

Laser Doping for Silicon Solar Cells: Modeling and Application

Von der Fakultät Informatik, Elektrotechnik und Informationstechnik der
Universität Stuttgart zur Erlangung der Würde eines Doktors-Ingenieurs
(Dr.-Ing.) genehmigte Abhandlung.

Vorgelegt von
Mohamed Hassan
geboren am 28.09.1990 in Giza, Ägypten

Hauptberichter:	Prof. Dr. rer. nat. habil. Jürgen H. Werner
1. Mitberichter:	Prof. Dr.-Ing. Norbert Frühauf
2. Mitberichter:	Prof. Dr. Michael Saliba

Tag der Einreichung:	07.10.2022
Tag der Mündlichen Prüfung:	26.09.2023

Institut für Photovoltaik der Universität Stuttgart
2024

To my family

Contents

Contents	i
Zusammenfassung	1
Abstract	3
1 Introduction	5
1.1 Motivation	5
1.2 Thesis Structure	6
2 Background	9
2.1 Silicon solar cell	9
2.1.1 Interdigitated back contact solar cell (IBC-SC)	10
2.1.2 Sheet Resistance	14
2.2 Sputtering	15
2.3 Laser Doping	16
2.3.1 Laser Processing Background	16
2.3.2 Laser Background	17
2.3.3 Doping Background	20
3 Experimental and Characterization Techniques	23
3.1 Laser System	23
3.2 Sputtering	25
3.3 Sheet Resistance	26
3.4 Secondary Ion Mass Spectroscopy	27
3.5 Laser scanning microscopy	27
3.6 Profilometer	27

4	Model and Simulation	29
4.1	Finite-Difference Method	30
4.1.1	Finite-Difference Forms of the Heat and Diffusion Equations .	30
4.1.1.1	The Heat Equation	30
4.1.1.2	The Diffusion Equation	32
4.1.2	The Nodal Network	34
4.1.2.1	Numerical Calculation Stability	37
4.1.2.2	The Interface Properties	38
4.2	Laser Doping of silicon	40
4.2.1	Heat Transfer Model	41
4.2.1.1	Heat Source	41
4.2.1.2	Laser-Silicon Interaction	44
4.2.1.3	Heating Phase	45
4.2.1.4	Phase Transformation	45
4.2.1.5	Melting the Silicon Surface	46
4.2.1.6	Evaporation of the Silicon Surface	46
4.2.1.7	Temperature-Time Curve	48
4.2.1.8	Model Validation	49
4.2.1.8.1	Experimental	49
4.2.1.8.2	Melt Dimensions' Validation	51
4.2.2	Mass Transfer Model	56
4.2.2.1	Diffusion Processes	56
4.2.2.2	Model Validation	59
4.2.2.2.1	Experiment	59
4.2.2.2.2	Validation	60
4.2.2.3	Assumption in the Model	63
5	Sheet Conductance of Laser Doped Layers	77
5.1	Introduction	78
5.2	Geometrical Consideration of Melted Regions	80
5.3	Experiment	82
5.4	Results and Discussion	83
5.4.1	Simulation Results	83

Conclusion	97
A Appendix	99
A.1 Material Properties	99
A.1.1 Optical Properties	99
A.1.2 Thermal and Mechanical Properties	100
A.2 Experimental Facilities	101
A.2.1 Laser System	101
A.2.2 Laser Power Measurement	103
A.2.3 Sputtering	104
A.2.4 Secondary Ion Mass Spectroscopy	108
A.2.5 Laser scanning microscopy	112
A.2.6 Profilometer	115
List of Figures	117
List of Tables	121
Bibliography	123
List of Publications	135
Acknowledgment	137

Zusammenfassung

Die Laserdotierung von Silizium ist eine etablierte Technik in der Photovoltaik. Während der Bestrahlung schmilzt ein fokussierter Laserstrahl die Siliziumoberfläche, und die Dotierungsatome diffundieren aus einem Precursor in das geschmolzene Silizium. Die rekristallisierte Siliziumoberfläche ist lokal dotiert und defektfrei. Abhängig vom Precursor und der angewandten Pulsenergiedichte verwandelt sich der Precursor während des Dotierungsprozesses entweder in Flüssigkeit oder Gas. Teile der Siliziumoberfläche können während des Dotierungsprozesses verdampfen, wenn die verwendete Pulsenergiedichte ausreichend hoch ist. Diese Arbeit stellt ein vereinheitlichtes Modell vor, das in der Lage ist, die verschiedenen Dotierungsfälle zu simulieren. Das Modell kann nicht nur die tiefenabhängigen, mittleren Dotierungsprofile vorhersagen, sondern auch die lateral und tiefenabhängigen geschmolzenen Abmessungen, die Tiefe und die Breite der deformierten Oberfläche über einen weiten Bereich von Laserenergiedichten.

Das Modell zeigt, dass etwa 50% der verdampften Materialien nach der Rekristallisation der Siliziumoberfläche wieder kondensieren. Je nach Überlappung wird ein Teil dieser 50% recycelt. Darüber hinaus zeigt das Modell, dass der Diffusionsprozess durch Marangoni-Konvektion verstärkt wird: Die gaußförmige Intensitätsverteilung des bestrahlenden Strahls erzeugt eine temperaturgradienteninduzierte Oberflächenspannung zwischen dem heißen Schmelzzentrum und den gerade geschmolzenen, relativ kalten Rändern, was dazu führt, dass die Schmelze zirkuliert. Der Diffusionsprozess in der Schmelze wird durch eine Exponentialfunktion beschrieben. Schließlich zeigen wir, dass der Wert des höheren pre-exponentiellen Faktors $D_0 = 8 \times 10^2 \text{ cm}^2/\text{s}$ dominiert, wenn die maximale Temperatur den Wert von $T \geq 2100 \text{ K}$ überschreitet.

Diese Arbeit verwendet dann das vereinheitlichte Modell, um die Abhängigkeit des Schichtleitwerts G_{sh} einer laserdotierten Schicht von ihrer Geometrie darzustellen. Für eine konstante Dotierungsdosis D_B ändert sich der Schichtleitwert G_{sh} linear mit dem Verhältnis zwischen der Tiefe d_{ch} des Schnitts zwischen zwei nebeneinander liegenden, lokal dotierten Bereichen und der Gesamttiefe d_{ch} der aufgeschmolzenen Schicht. Dieses Verhältnis zeigt, dass eine inhomogen (in Konzentration und Schichttiefe) laserdotierte Schicht durch eine homogen (in Konzentration und Schichttiefe) dotierte Schicht mit einer Flächenkonzentration $C_B = \bar{D}_B/d_{\text{melt}}$ und einer Tiefe $d = d_{\text{ch}}$ approximierbar ist. Für ein Verhältnis $d_{\text{ch}}/d_{\text{melt}} = 1$ hat die laser-

dotierte Schicht eine regelmäßige Tiefe wie eine durch Ofendiffusion erzeugte Schicht ($d_{\text{ch}} = d_{\text{melt}}$). Für eine nicht kontinuierliche Schicht ($d_{\text{ch}}/d_{\text{melt}} = 0$) fällt der Schichtleitwert auf null ($G_{\text{sh}} = 0 \text{ mS}$) aufgrund der elektrischen Trennung zwischen benachbarten, lokal dotierten Regionen.

Abstract

Laser doping of silicon is a well-established technique in photovoltaics. During irradiation, a line-focused laser beam melts the silicon surface and the doping atoms from a precursor diffuse into the melted silicon. The resolidified silicon surface is locally doped and defect free. Depending on the precursor and the applied pulse energy density, the precursor either turns into liquid or gas during the doping process. Parts of the silicon surface may evaporate during the doping process if the used pulse energy density is high enough. This work presents a unified model which is capable of simulating the different doping cases. The model is able to predict not only the doping profiles, but also the melted dimensions, depth, and width of the deformed surface over a wide range of laser energy density. The model showed that about 50% of the evaporated materials recondense after the resolidification of the silicon's surface. Depending on the overlap, part of the 50% is recycled. Additionally, the model shows that the diffusion process is enhanced by Marangoni convection: the Gaussian intensity distribution of the irradiating beam introduces a temperature gradient-induced surface tension between the hot melt center and the just melted edges causing the melt to circulate. Finally, we show that the value of the higher pre-exponential factor $D_0 = 8 \times 10^2 \text{ cm}^2/\text{s}$ dominates when the maximum temperature $T \geq 2100 \text{ K}$.

This work then uses the unified model to exhibit the dependence of the sheet conductance G_{sh} of a laser doped layer on its geometry. For a constant doping dose D_{B} , the sheet conductance G_{sh} linearly changes with the ratio between the depth d_{ch} of the intersection between the successive locally doped regions and the total layer's depth d_{melt} . For a ratio $d_{\text{ch}}/d_{\text{melt}} = 1$, the laser doped layer has a regular depth like a furnace-diffused layer, $d_{\text{ch}} = d_{\text{melt}}$. For a non-continuous layer, $d_{\text{ch}}/d_{\text{melt}} = 0$, the sheet conductance drops to zero $G_{\text{sh}} = 0 \text{ mS}\square$ (no current flows) due to the electrical separation between the locally doped regions.

Chapter 1

Introduction

1.1 Motivation

In recent years, greater emphasis has been placed on the importance of clean (low carbon dioxide CO₂ emission) energy resources. As a result, the German Federal Government declared that decreasing greenhouse gas emissions by 80% to 90% by 2050 [1–3] is one of its political goals. Photovoltaic *PV* solar energy is an important form of clean energy resources. In their 2019 report [4], the international energy agency *iea* predicted a 250% growth of PV capacity worldwide by 2024, which would achieve about 530 GW. In 2023 report from Fraunhofer ISE, it is reported that already about 945 GW are delivered from the cumulative installation of photovoltaics by the end of 2022 [5]. Fueled by global and governmental targets, the institute for photovoltaics (ipv) at Stuttgart university developed the laser-processed interdigitated back-contact (IBC) solar cell and achieved record efficiency 23.2% [6–10]. Understanding the different production steps of the laser-processed IBC solar cell is the key for improving energy conversion efficiency. Laser doping does not only enable a localized doping but also a defect-free doping [11, 12]. Furthermore, different research teams [11, 13, 14] have shown that besides a high spatial resolution, laser melting with a line-focused beam leaves a defect-free resolidified surface.

For doping of silicon, the ipv uses a deposited boron-containing precursor layer on a silicon surface which serves as a dopant source during the laser doping process. The precursor layer consists of two layers: a boron oxide layer (the boron atoms' source) and an amorphous silicon layer (the protecting layer for the boron oxide

layer against humidity in air). Due to the hygroscopic properties of boron oxide B_2O_3 [15], the amorphous silicon ($a-Si$) layer is necessary for maintaining stability of the doping process. During the laser doping process, a line-focused laser beam irradiates the two-layer precursor system and the crystalline silicon surface. A deep understanding of how system components react during laser processing and how lasing parameters affect the resulting doping profile is necessary to improve the doping process and to increase productivity for lower processing costs.

This work studies the laser doping process of silicon and proposes a unified model for laser doping from different precursors. The model enables the prediction of doping profiles resulting from doping with low and high pulse energy densities. Finally, this work contributes to knowledge obtained from the laser doping model to understand the dependence of the resulting sheet conductance G_{sh} of the doped layers on the layer's depth irregularity. This work deduces an equation to accurately calculate the sheet conductance G_{sh} for doped layers with an irregular depth.

The next section describes the building blocks of the present work.

1.2 Thesis Structure

This work consists of five chapters:

Chapter 2 demonstrates the building blocks of the back contact solar cell as well as the different production steps followed by the fabrication of each building block. This chapter then exhibits technologies used for creating a boron-doped region. For that purpose, this chapter briefly describes the radio frequency (RF) sputtering technique which deposits the precursor layer, which is the source of boron atoms used during the laser doping step. The discussion describes the propagation of a laser beam and the most important equations for calculating energy density. Finally, this chapter describes the laser doping process.

Chapter 3 describes the facilities used for conducting the experimental part of the present work and also illustrates the functioning principle for each machine. Additionally, this chapter briefly describes the facilities used for characterization and illustrates measurement techniques.

Chapter 4 visualizes the laser doping model postulated in this work. This chapter also shows how the heat and diffusion equations are numerically discretized and solved. The model then describes in detail the interaction between laser radiation,

the polished silicon surface and the precursor layer. Furthermore, the model depicts the state transition of each component during the irradiation period. Afterwards, in light of the experimental data, this chapter validates the postulated model.

Chapter 5 determines the dependence of the sheet conductance on the doped layer's depth regularity. This chapter describes the experiment used, exhibits the modeled and experimental results, and discusses the results. Finally, this chapter deduces a relationship between the resulting sheet conductance and the irregularity of the layer's depth.

Chapter 2

Background

This chapter illustrates the physical background necessary for the execution of the present work. This chapter describes the production steps and the working principle of the back contact silicon (IBC) solar cells. Moreover, this chapter introduces manufacturing techniques relative to this work: radio frequency *RF* sputtering and laser processing. Finally, this chapter closes by illustrating the laser-doping process of silicon.

2.1 Silicon solar cell

The world is currently striving to produce a high portion of consumed energy from clean sources. Photovoltaics, as a renewable energy source, is a promising choice to achieve this goal. Silicon is the second most abundant element in the earth's crust [16] and in the same time, silicon solar cells exhibit high efficiency for relatively cheap costs. These two reasons, the high silicon abundancy together with the high efficiency-to-cost ratio, paved the way for the occupation of silicon solar cells about 95% of total photovoltaic production [5]. The most famous silicon-based solar cells are: aluminum back surface field solar cells *AL – BSF* (energy conversion efficiency $\eta = 19.8\%$ [17]), passivated emitter and rear solar cells *PERC* ($\eta = 22.5\%$ [18]), and interdigitated back contact solar cells *IBC* ($\eta = 23.24\%$ [6]). Both AL-BSF and PERC solar cells have the emitter contacts on the front side and the back surface field *BSF* contacts on the back back. The front-contacted solar cells suffer from shadowing losses due to prohibiting a portion of incident sunlight by metallization

[19, 20]. On the contrary, the IBC solar cells have the metallic contacts of both polarities on the back side, which allows 100% of incident light to react with the solar cell [21]. The next section describes the production steps of the IBC solar cell developed at the institute for photovoltaics *ipv* at Stuttgart university.

2.1.1 Interdigitated back contact solar cell (IBC-SC)

As indicated by its name, the interdigitated back contact solar cell has all of its contacts on the backside. The metallization-free front surface allows 100% of incident light to react with the solar cell. Furthermore, it reduces the recombination of charge carriers at the critical carrier-generation region (the front region), which improves the cell's efficiency. The word “interdigitated” describes how the contact fingers are integrated on the back side as two in each other kinked combs.

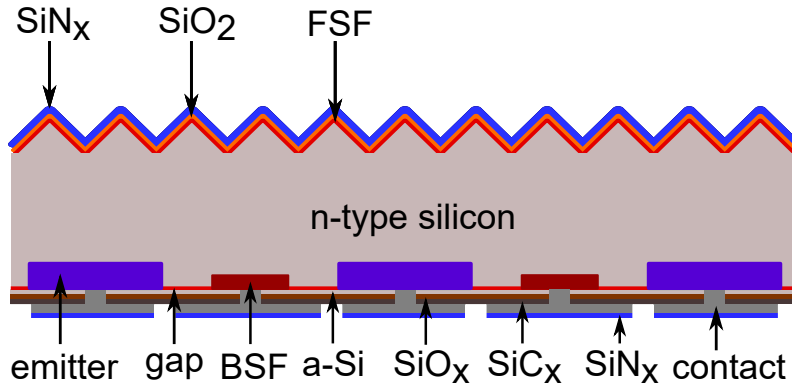


Figure 2.1: Schematic representation of the cross-section of the IBC solar cell developed in *ipv* [7, 22].

Figure 2.1 schematically shows a cross-sectional representation of the interdigitated back contact (IBC) solar cell developed at the institute for photovoltaics *ipv* [7, 22]. The front side (the sun-facing side, or the upper side) has a pyramidal texture with a face angle of 54.7° , which enhances light entrappment in the solar cell's depth. For further improvement of the optical properties of the solar cell, an anti-reflection coating of SiN_x faces the incident light. A silicon dioxide SiO₂ layer chemically passivates the unsaturated superficial silicon bonds of the front side. A phosphorous-diffused layer forms the front surface field *FSF*, which passivates the silicon surface through the field-effect. The front surface is n⁺-doped as the base

wafer is n-type. Both highly doped regions, the emitter (p^{++} -doped) and the back surface field *BSF* (n^{++} -doped), lie on the backside. The in-between regions are called gap regions and are doped with phosphorus (n^+ -doped) to provide the field-effect passivation. An amorphous silicon $a-Si:H$ layer chemically passivates the gap regions of the back side. A silicon oxide SiO_x layer followed by a silicon carbide SiC_x layer form a dielectric layer and cover the passivating a-Si:H layer. The dielectric layer improves the optical properties of the solar cell. Finally, for metallization, aluminum fingers contact both polarities and are covered with a silicon nitride SiN_x layer as an electrical isolation sheet. The sequence of the manufacturing techniques of the different parts of the IBC solar cell as well as the functions are as follows:

- **Base material** of the solar cell is a 6-inch Czochralski-grown *CZ* n-type silicon wafer with thickness $t \approx 160 \mu\text{m}$ of resistivity $\rho_{\text{electrical}} \approx 2 \Omega\text{cm}$.
- **Front surface texturing** takes place through anisotropic etching in a 3% potassium hydroxide *KOH* solution at 80°C for 20 min. Potassium hydroxide *KOH* displays a significantly slower etching rate in the $\langle 111 \rangle$ crystal directions compared to the $\langle 100 \rangle$ directions. Consequently, both sides result in a pyramidal surface texture that have a face angle of 54.7° and an average height between 3 and $4 \mu\text{m}$.
- **Front side texturing and backside polishing** occur in two chemical steps. The texturing step occurs in a 3% *KOH* solution followed by the polishing step in a 25% *KOH* solution at 80°C for 10 min. To protect the textured front side, a PECVD process deposits a silicon nitride SiN_x layer on the front surface [23]. The polishing step is crucial for the subsequent doping process; laser doping of the textured surface non-uniformly melts the randomly-sized pyramids causing a non-homogeneous doping of the surface and results in a nonlinear shunt element [24]. After the polishing step, the protective SiN_x layer on the front surface is etched away using a 5% *HF* solution.
- **Emitter** (the p^+ layer) arises from laser doping of the silicon surface with a deposited boron-containing layer. To perform a clean doping process and to produce a high quality emitter, after the polishing step of the backside and prior to the sputtering step, a two-stage wet chemical cleaning step occurs. Chemical cleaning consists of a dip in a 5% *HF* solution followed by a rinse

in a 10% HCl solution which removes the native silicon oxide and removes of the metallic contamination on both wafer surfaces, respectively. Directly after chemical cleaning, a sputtering machine deposits the boron-rich precursor layer, which provides the melted silicon surface during laser doping with boron to form the p^+ regions. The boron-containing layer is produced by sputtering a boron oxide target on the freshly-cleaned surface. By controlling sputtering power and time, the thickness of the deposited layer, and thus, the sheet resistance of the emitter layer, is controlled [25]. Directly after the deposition step, a pulsed nanosecond line-focused laser beam irradiates and dopes the surface locally with a precision of $30\text{ }\mu\text{m}$ [26, 27]. Unlike the circular-focused laser beam that induced defects after resolidification [28], the line-focused laser beam results in a defect-free resolidified boron-doped silicon surface [11, 12, 23].

- **Cleaning** of the rest of the unused boron layer occurs prior to the next step. The cleaning process occurs in 4 steps: a dip in a 5% HF solution followed by a dip in a mixture solution consisting of nitric acid HNO_3 , acetic acid CH_3COOH , and flouric acid HF , then again a dip in a 5% HF and a rinse in a 10% HCl solution. Afterwards, a cleaning step takes place in the standard cleaning solution (SC1 and SC2) [29], then finally in a 5% HF solution.
 - The front surface field **FSF** is produced through a furnace diffusion step. It provides a field-effect passivation to the two silicon wafer surfaces. A furnace diffusion step at 800°C in a phosphoroxchlorid-nitrogen $POCl_3-N_2$ flow in the range of 100 - 200 sccm deposits a phosphorus silicate glass *PSG* layer on the silicon surface allowing for the diffusion of phosphorus into the silicon surface, forming the phosphor-doped layer (the n^+ layer) underneath the silicon surface [30]. At the same time, the gettering effect in which the metallic contaminants (Cu, Fe, Cr, Ni, etc..) existing in the crystalline silicon diffuse out in the PSG layer takes place [31–33].
 - The backside field **BSF** eases the metallic contacting of the base n-type silicon. The PSG layer, deposited during the diffusion process on the silicon surface, serves as a phosphorus-rich precursor layer for the laser doping step. A line-focused green laser beam melts and dopes the silicon surface with the phosphorus forming the BSF layer. The high surface concentration of phospho-
-

rus reduces the contact resistance between the silicon surface and the metallic contact after the metallization step. As a result, the overall series resistance R_s term decreases and the solar cell efficiency η_{sc} increases [23]. Furthermore, the BSF layer forms a field-effect passivation [30]. Finally, the cleaning step mentioned in the last point is repeated to remove the PSG layer rests.

- The silicon dioxide ***SiO₂*** layer is about 10 nm thick and passivates the silicon surface chemically. The oxygen atoms saturate the dangling bonds existing at the silicon-air interface. An oxidation process at 1000°C for 5 min forms about 15 nm thick SiO₂ layer on both wafer surfaces [23, 30].
 - A PECVD process conducted at temperature $T_{dep} = 175^\circ\text{C}$ deposits a 30 nm thick hydrogenated amorphous silicon ***a-Si:H*** layer with an optical band gap $E_{g, a-Si} \approx 1.75$ eV. The a-Si:H layer passivates the non-contacted n^{++} -, n^+ - and p^{++} -doped back side of the silicon wafer perfectly [8–10, 30, 34].
 - The silicon nitride ***SiN_x*** layer improves the optical properties of the solar cell. On the front side, a 70 nm-thick SiN_x layer serves as an anti-reflection coating *ARC*. It maximizes the photogenerated current density $J_{gen, max}$. A plasma-enhanced chemical vapor deposition *PECVD* process deposits the SiN_x layer [7]. On the metallization, the SiN_x layer forms an isolation layer.
 - A **dielectric stack** consists of a 150 nm thick silicon oxide ***SiO_x*** layer and a 50 nm thick silicon carbide ***SiC_x*** layer is deposited through a PECVD step. The stack improves light entrapment in the solar cell [30].
 - A pulsed UV-laser (wavelength $\lambda = 355$ nm) locally ablates the stack and the a-Si:H passivation layer on the back side at the contact positions. To avoid the occurrence of surface damage during the **ablation step**, the laser beam, using a moderate pulse energy density H , partially ablates the stack layer system. The rest of the a-Si:H layer is then cleaned away with a 20% KOH solution [30]. The ablated areas are now ready for the metallization step.
 - A 5 μm thick aluminum *Al* layer contacts the exposed doped silicon areas forming the **metallization step**. The aluminum layer is deposited through an evaporation step forming a continuous Al layer which connects both polarities simultaneously.
-

- An **electrical separation** of both polarities occurs by the PECVD deposition of a 150 nm thick SiN_x layer over the aluminum layer. The SiN_x layer acts as a masking layer for the contact fingers, and later on, as an electrical isolation layer. A pulsed UV-laser system entirely ablates the masking SiN_x layer where the finger separation areas should exist [35]. Finally, an etching process in a 85% phosphoric acid H_3PO_4 at 80°C for 5 min etches away the exposed Al areas, separating the different polarity fingers from one other [30].

2.1.2 Sheet Resistance

Sheet resistance R_{sh} is the resistance to current flow through thin films or thin sheets. Sheet resistivity is another name for sheet resistance R_{sh} . Due to free electrons in n-type silicon and free holes in p-type silicon, doped silicon shows a significantly lower sheet resistance than intrinsic/lightly-doped silicon. On one hand, a lightly-doped n-type silicon of homogeneous donor concentration $C_D = 10^{15} \text{ cm}^{-3}$ has resistivity $\rho = 4.6 \Omega \text{ cm}$, whereas a highly-doped n-type Si ($C_D = 10^{19} \text{ cm}^{-3}$) shows a resistivity $\rho = 0.0059 \Omega \text{ cm}$. On the other hand, a p-type Si of homogeneous acceptor concentration $C_A = 10^{15} \text{ cm}^{-3}$ exhibits a resistivity $\rho = 13.5 \Omega \text{ cm}$, whereas $C_A = 10^{19} \text{ cm}^{-3}$ shows a resistivity $\rho = 0.0098 \Omega \text{ cm}$.

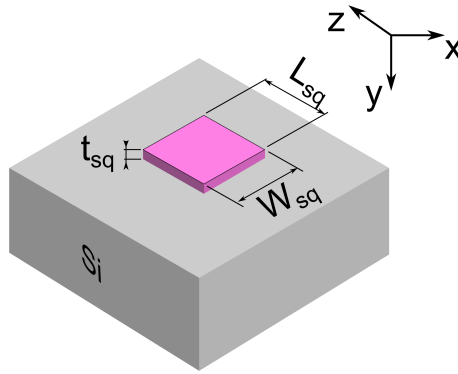


Figure 2.2: Scheme of a doped square-like area in an undoped silicon wafer. The doping concentration C_{maj} is homogeneous in the x - z plane.

Figure 2.2 schematically represents a doped square-shaped area in an intrinsic silicon wafer surface. The conductive sheet has a uniform sheet thickness t_{sq} and homogeneous doping concentration C_{maj} in x - z plane. The thickness t_{sq} of the con-

ductive sheet is significantly smaller in comparison to the other two dimensions, L_{sq} and W_{sq} . The sheet resistance R_{sh} relates to the bulk resistance R , the resistivity ρ and the conductive sheet dimensions, depth t_{sq} , length L_{sq} and width W_{sq} through

$$R = \rho \frac{L_{sq}}{A_{sq}} = \frac{\rho}{t_{sq}} \frac{L_{sq}}{W_{sq}} = R_{sh} \frac{L_{sq}}{W_{sq}} = \frac{L_{sq}}{G_{sh} W_{sq}}. \quad (2.1)$$

The unit of sheet resistance R_{sh} is Ω/\square , whereas the unit of sheet conductance G_{sh} (the reciprocal of the sheet resistance R_{sh}) is S/\square . This implies that the resistance R of a conductive sheet with an aspect ratio $L_{sq}/W_{sq} = 1$ equals the sheet resistance R_{sh} . Eq. 2.1 is valid for the case of a doping concentration C_{maj} , which is homogeneous in the three dimensions. The doping concentration C_{maj} of a furnace-diffused or a laser-doped layer, may not be homogeneous in depth (y -direction), which affects the sheet resistance R_{sh} as follows:

$$R_{sh} = \frac{\rho}{t_{sh}} = \frac{1}{\sigma_{maj}(y) y} = \frac{1}{q \int_0^{y=t_{sq}} \mu_{maj}(y) C_{maj}(y) dy} = \frac{1}{G_{sh}}, \quad (2.2)$$

where C_{maj} is the dopant concentration and μ_{maj} is charge carriers mobility. From the previous example, the resistivity ρ at p-type base doping concentration $C_A = 10^{15} \text{ cm}^{-3}$ was almost 3 times higher than ρ of n-type base doping at the same concentration C_D in silicon. The difference between both cases, the n-type and p-type at the same base doping concentration, is the mobility of majority charge carriers. Electrons have significantly higher mobility than holes at the same concentration in silicon [36, 37].

2.2 Sputtering

The phenomenon of ejection of an atom or a cluster of atoms from a solid surface through a collision process with an accelerated ion is called *Sputtering* [38, 39]. Sputtering is currently used for thin film deposition, surface cleaning and etching, and surface layer analysis [40].

Figure 2.3 schematically represents the sputtering deposition chamber. The target, which is the material to be deposited, is sputtered by accelerated argon Ar^+ ions. An alternating polarity applies to both, the substrate and the target, with a

frequency $f_{sp} = 13.56$ MHz. The process gas is the inert argon Ar gas. A pumping system controls the pressure of the deposition chamber.

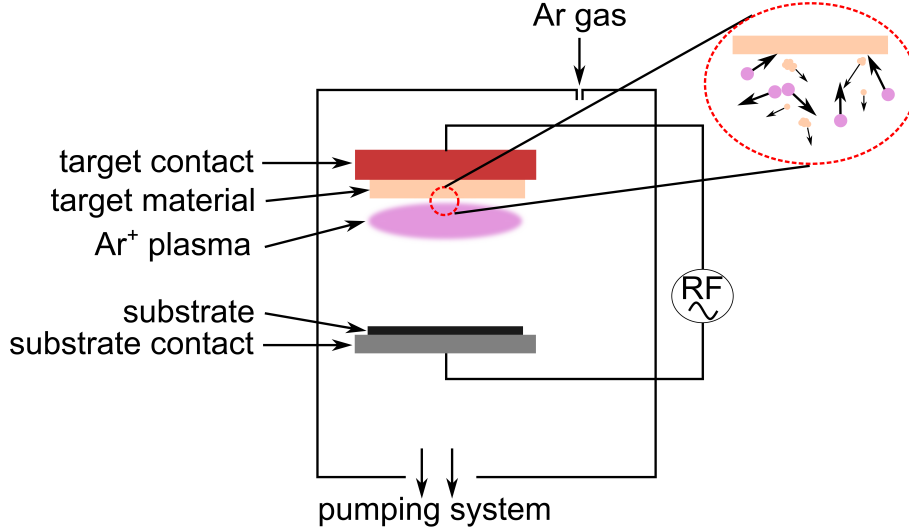


Figure 2.3: Scheme of the radio frequency sputtering deposition chamber. Under the applied alternating bias, the process gas (argon) ionizes. The Ar^+ ions impinge the surface of the target material mounted on the cathode, causing dislodgement of target surface atoms. The sputtered atoms(s) deposit on the exposed areas of the deposition chamber.

2.3 Laser Doping

2.3.1 Laser Processing Background

Figure 2.4 schematically represents one type of laser processing unit used for material processing. The main components are: the laser source, the optical system, and the work piece positioning system [41]. The precise positioning of the focused laser beam on the working piece follows one of three concepts: either moving the laser source, or moving components of the optical system [42] or moving the working specimen itself (the configuration shown in fig. 2.4). In the latter, the working-piece holding system fixes the working piece during the processing. The holding system moves, with the working piece fixing on it, in the x- and y-directions, to provide a precise positioning of the focused laser beam on the working piece surface. This precise

positioning gives the laser the ability to dope, anneal, and structure silicon wafers in the semiconductor industry [43].

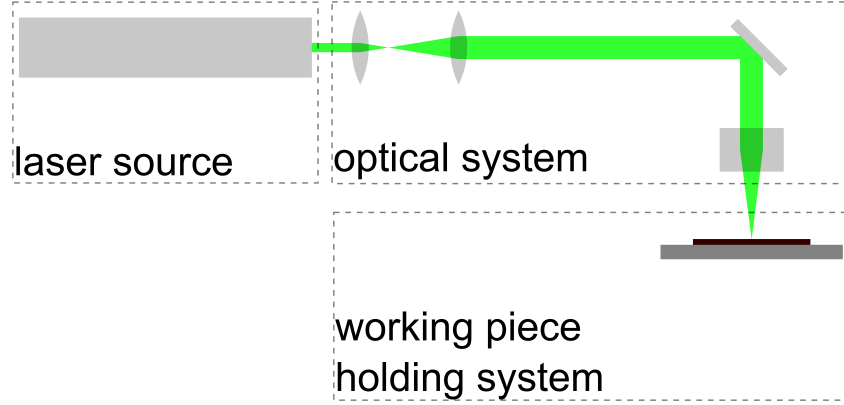


Figure 2.4: Scheme of a typical laser processing machine. The machine's main sections are: the laser source, the optical system, and the working piece-holding stage. For precise positioning of the laser beam, a movable holding stage fixes the working piece during the processing.

2.3.2 Laser Background

Laser as a word stands for **L**ight **A**mplification by **S**timulated **E**mission of **R**adiation. The emitted photons are temporally and spatially coherent [44]. The coherent electric fields of the propagating waves/photons are called mode. Coherency increases with the decreasing number of propagating modes inside the laser resonator. The intensity of an electromagnetic wave is directly proportional to the square of the amplitude E_0 of the electric field as expressed

$$I_{\text{em}} = \frac{n\varepsilon_0 c_0 E_o^2}{2\mu_r}, \quad (2.3)$$

where μ_r is the relative permeability, ε_0 is the dielectric constant of free space, and c_0 is the light speed in free space. Each electric field of a propagating mode is represented by a linear combination of plane waves according to Fourier-Transformation. Thus, the intensity I_{em} of a propagating mode is the square of the summation of the electric fields' amplitudes E_0 of the linear combination of plane waves representing

that mode. On the contrary, the intensity of multiple modes (e.g. incoherent propagating waves) is the summation of the intensities of each single mode. That is why a single mode laser has a high intensity as $I_{\text{mode}} = (\sum_{j=1}^n E_{0j})^2 > I_{\text{incoherent}} = \sum_{j=1}^n I_{\text{emj}}$ [45].

The small transversal divergence θ to the propagation direction is another important characteristic of lasers. That is one reason to consider the electromagnetic laser beam as a paraxial wave (the paraxial approximation). The transversal change of intensity distribution of a laser during propagation along the y-axis is described by the transversal electromagnetic modes TEM_{mn} families, the Hermite-Gauss modes and the Laguerre-Gaussian modes. The fundamental mode, known as the Gaussian mode, of these families is the TEM_{00} mode, where $m = 0$ and $n = 0$. Propagation modes with higher values of m and n are called higher-order modes.

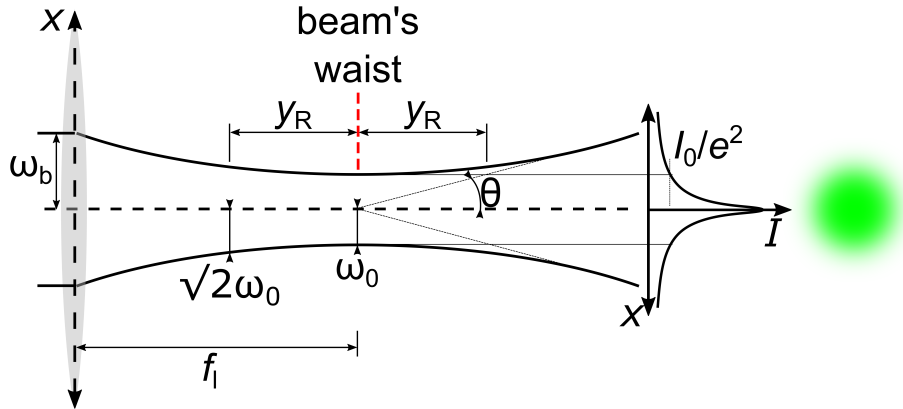


Figure 2.5: Scheme of a green focused round laser spot having a Gaussian intensity distribution. A round laser beam of radius ω_B falls on a convex length of focal length f_l . The laser beam's waist $2\omega_0$, where the beam's radius ω is the smallest, lies at the focal length f_l of the focusing lens. The area A_p of the laser spot doubles at a distance $y = \text{Rayleigh length } y_R$. The angle at which the beam transversally expands is called the angle of divergence. Half of the angle of divergence θ depends inversely on the Rayleigh length y_R and the beam's radius at the beam's waist ω_0 . The radius ω of the Gaussian beam occurs at the position where the maximum intensity I_0 drops by a factor $1/e^2$. The real appearance of the focused round green spot exists on the right of the figure.

Figure 2.5 visualizes the radial change of a round green laser beam along the

propagation axis, the y-axis, propagating in the TEM₀₀ mode. The intensity I distribution of the TEM₀₀ mode is

$$I(x, y) = I_0 \exp\left(-\frac{2x^2}{\omega_0^2}\right), \quad (2.4)$$

where I_0 is the maximum intensity and occurs at the middle of the beam, i.e. at transversal directions $x = 0$ and $y = 0$. The radius ω of the propagating TEM₀₀ mode is the radius at which the intensity I drops to the factor of $1/e^2$ of the maximum intensity I_0 . The maximum intensity depends on the laser power P through

$$I_0 = \frac{P}{\pi\omega^2/2}. \quad (2.5)$$

At the beam's waist, the beam's radius ω is the smallest and has the value $\omega = \omega_0$ and occurs at the focal length f_1 of a focusing optical element, e.g. a convex lens, when a collimated laser beam (i.e. divergence angle $\theta \approx 0$) passes through it. The beam's radius ω varies along the propagation direction, the y-axis, as follows:

$$\omega^2(y) = \omega_0^2 \left(1 + \frac{y^2}{y_R^2}\right), \quad (2.6)$$

where y_R is the Rayleigh length. At $y = y_R$, the beam's radius is $\omega = \sqrt{2} \omega_0$. Thus, the Rayleigh length y_R is the length at which the area of the round beams is doubled and the intensity is halved. The Rayleigh length y_R depends on the beam's waist ω_0 , the wavelength λ of the emitted beam through [41, 45]

$$y_R = \frac{\pi \omega_0^2}{\lambda} = \frac{\pi d_0^2}{4\lambda}, \quad (2.7)$$

where $d_0 = 2\omega_0$ is the diameter of the beam at the beam's waist.

On the basis of the paraxial approximation, half of the angle of divergence θ of the propagating beam depends on the beam's waist radius ω_0 and the Rayleigh length y_R through

$$\theta = \frac{\omega_0}{y_R}. \quad (2.8)$$

The transversal expansion of the propagating beam in the Gauss mode, TEM₀₀ mode, is the smallest in comparison to the higher order propagation modes, TEM_{m,n} with $m > 1$ and $n > 1$ [41].

The beam parameter product BPP is a physical parameter that describes the beam's quality, and therefore the focusability of the laser beam. The full divergence

angle $\Theta_f = 2\theta_f$ and the diameter d_f of the focused beam at the beam's waist express the BPP as follows [41, 45]

$$BPP_{\text{any beam}} = \frac{d_f \Theta_f}{4} = \frac{d_f^2}{4y_R}. \quad (2.9)$$

Substituting eq. 2.7 in eq. 2.9, we get

$$BPP_{\text{diffraction-limited}} = \frac{\lambda}{\pi}, \quad (2.10)$$

which is the beam parameter product in the case of a diffraction-limited beam. The beam quality parameter M^2 is the normalization of the quality of an actual beam to the diffraction-limited beam and is represented

$$M^2 = \frac{BPP_{\text{any}}}{BPP_{\text{diffraction-limited}}} = \frac{\pi d_f \Theta_f}{\lambda} = \frac{\pi d_f^2}{\lambda 4y_R}. \quad (2.11)$$

A beam of quality parameter $M^2 = 1$ behaves as a TEM_{00} propagating mode, Gauss beam.

The distance over which the focused spot size variation equals $\pm 5\%$ which results in laser intensity variation of $\pm 10\%$ is called the depth of focus DOF [44, 46]. A higher DOF value enables laser processing of a non-flat surface with different depths without significantly changing the final result. Applying the geometrical similarity from fig. 2.5, DOF is obtained as:

$$DOF = 0.025 (2y_R) = 0.05 y_R. \quad (2.12)$$

This work uses the energy density parameter to express the energy density used to irradiate the samples. In the case of a pulsed laser, the pulse energy density H varies with the average power P_{av} and the pulse repetition rate f and beam area A_p according to

$$H[\frac{\text{J}}{\text{cm}^2}] = \frac{P_{\text{avg}}[\text{W}]}{f[\text{Hz}] A_p[\text{cm}^2]} = \frac{E_p[\text{J}]}{A_p[\text{cm}^2]}. \quad (2.13)$$

The pulse energy E_p is the average power P_{av} divided by the repetition rate f .

2.3.3 Doping Background

In 1980, T. F. Deutsch et al. conducted the first successful laser doping experiment using a pulsed [47] and a continuous wave (cw) UV-laser [48]. A laser irradiates and

melts the surface allowing the dopant material(s) to diffuse in silicon and become activated [13, 49] to locally improve silicon's electrical properties [50]. Doping using lasers enabled the research team at the institute for photovoltaics (*ipv*) at Stuttgart University to achieve an efficiency $\eta_c = 23.2\%$ [7].

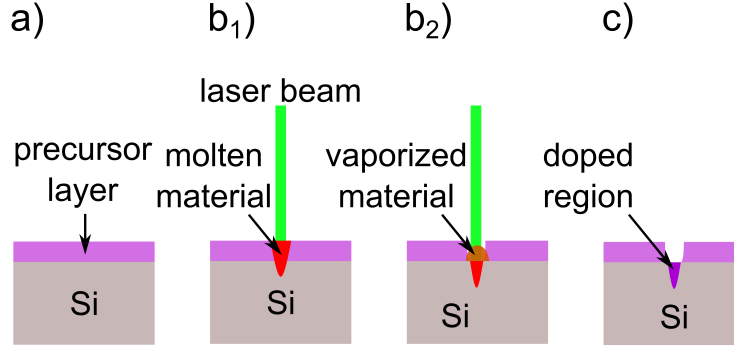


Figure 2.6: Scheme of the doping process of a silicon wafer with doping material from a pre-deposited precursor layer using a green laser beam. a) A pre-deposited precursor layer, which acts as a source of doping material, covers the surface of the silicon wafer. b₁) A green laser beam irradiates the surface of the silicon wafer. If the absorbed energy is sufficiently high, both materials, the precursor and the silicon surface locally heat up and melt. The two molten materials diffuse into one other, allowing for the doping process of silicon to take place. b₂) If the absorbed energy is sufficiently high, a portion of the irradiated materials locally evaporates, allowing for gas-liquid diffusion to occur. c) After irradiation ends, the molten material cools and solidifies in the form of a locally-doped solid silicon region. A thinly-doped layer results from repeating the previous process multiple times.

Figure 2.6 schematically demonstrates the laser doping process of a silicon wafer using a pre-deposited precursor layer. Figure 2.6a shows the moment immediately prior to the laser doping process. The precursor layer covers the clean, oxide-free surface of the silicon wafer. It is not necessary for the precursor layer to exist in a solid state, however for the example shown, it exists in a solid state. Figure 2.6b₁ represents the moment of melting and doping. A green laser beam irradiates the surface. A part of the incident irradiation reflects back and the other part transmits through the wafer. If the silicon wafer is sufficiently thick (several micrometers), almost 100% of the transmitted laser energy is absorbed, which raises the tempera-

ture of the surface. The silicon surface and the precursor heat up and melt, allowing for the diffusion of dopants inside of it. Figure 2.6b₂ visualizes the case in which the absorbed laser energy is high enough to evaporate the precursor layer. In this case, the gaseous dopants diffuse inside the molten silicon. Figure 2.6c shows this scenario after the laser pulse ends and the molten materials cool down and re-solidify.

The advantage of laser doping over other techniques such as ion implantation is the high spatial selectivity for localized doping with a controlled junction depth without introducing surface defects [11, 12, 51, 52].

Chapter 3

Experimental and Characterization Techniques

This chapter discusses the experimental techniques and the characterization techniques used for laser texturing. The experimental techniques are those used for processing the samples, like the laser system and the sputtering system. Characterization techniques are those used to measure the sample features after processing, like the measurement of sheet resistance, the measurement of doping concentration profile, and the characterization of the processed surface.

3.1 Laser System

Figure 3.1a schematically represents the line-focused laser beam used to process the silicon surface. The beam has a width $w_p = 12 \mu\text{m}$ and a length $l_p = 800 \mu\text{m}$. Over the width (the x-axis), a Gaussian intensity distribution dominates, whereas over the length (the z-axis), a top-hat intensity distribution extends. The beam is a result of a complex optical system developed at the institute for photovoltaics (*ipv*). A description of the laser system is presented in appendix A.2.1.

Figure 3.1b shows a scheme of the laser processing of the silicon wafer surface. The line-focused beam irradiates the wafer surface. To achieve homogeneous doping, the irradiated areas have to intersect with one other. The degree of intersection is called the overlap O_x and O_z . The degree of overlap O_x and O_z depends on the intensity profile in each axis. On the one hand, the Gaussian intensity distribution

in the x-axis implies the usage of a high overlap O_x to achieve a homogeneously-doped layer. On the other hand, the top-hat distribution does not need high overlap in the z-direction. For high spatial precision of processing, the wafer is placed and aligned on a vacuum chuck with the assistance of a magnifying camera. Finally, a translational xz-table moves the chuck precisely to the given coordinates.

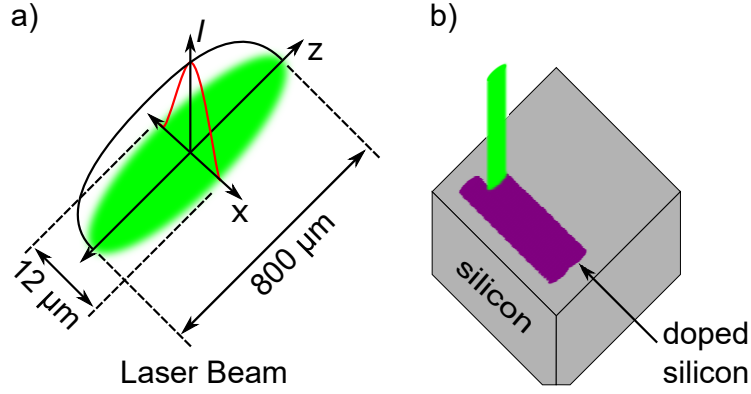


Figure 3.1: a) Scheme of the line-focused laser spot on the substrate's surface for the laser doping process. The laser spot has a Gaussian intensity distribution in the x-direction and a top-hat intensity distribution in the z-direction. The focused beam has a width $w_p = 12 \mu\text{m}$ and a length $l_p = 800 \mu\text{m}$. b) The line-focused green laser beam irradiates and dopes the surface of the silicon wafer. The scanning direction is in the x-direction. As a result of the intensity profiles in the x- and z-directions, homogeneous doping of the silicon surface is only achievable using a high overlap in the x-direction and a low overlap in the z-direction. The irradiated/doped area is violet while the undoped area is grey. During processing, a vacuum chuck fixes the wafer while the translational xz-table moves the chuck according to the laser file loaded to the controlling unit.

Figure 3.2 schematically demonstrates overlapping between the processed areas. The overlapping O_x in the scanning direction (the x-direction) depends on the combination of the width w_p of the used spot, the input laser pulse repetition rate f and the scanning speed v_{scan} through

$$O_x = \frac{(w_p - \Delta x)}{w_p} \times 100 = \frac{(w_p - \frac{v_{\text{scan}}}{f})}{w_p} \times 100. \quad (3.1)$$

The overlapping O_z in z-direction relays on the input displacement Δ_z in the laser

file and the length l_p of the focused laser spot as follows

$$O_z = \frac{(l_p - \Delta z)}{l_p} \times 100. \quad (3.2)$$

More overlap means melting the same area repeatedly, which affects processing quality and results. Since the focused spot has a line form, then the spot area A_p is approximated to be

$$A_p = w_p l_p. \quad (3.3)$$

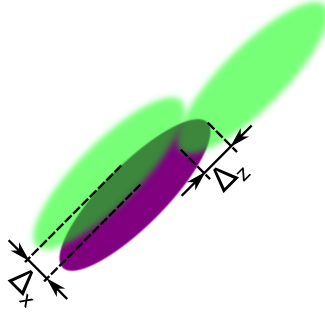


Figure 3.2: The overlap O_x between the irradiated/doped areas in the x -direction is schematically shown. The input scanning speed v_{scan} and laser pulse repetition rate f together with the width w_p of the focused laser spot determine the pulse-pulse distance Δx . The pulse-pulse distance Δz inputted through the loaded laser file together with the length l_p of the focused beam determine the overlap O_z in z -direction. The re-irradiated distances Δ_x and Δ_z are the area of overlap between the current pulse and the subsequent pulse in the x - and z -directions, respectively.

3.2 Sputtering

For homogeneously-deposited sheets, the Leybold Univex 600-il sputtering machine is used. Better homogeneity is a result of linear targets used and the moving wafer carrier. The linear targets guarantee homogeneous sputtering over its length, whereas the carrier moves back and forth underneath the target during the plasma-on time to achieve a homogeneous thickness of deposited sheet over 6 wafers. A scheme of the machine, the carrier and the sputter gun used by the univex as well

as a detailed explanation of the sputtering process used in this work is mentioned in appendix A.2.3.

3.3 Sheet Resistance

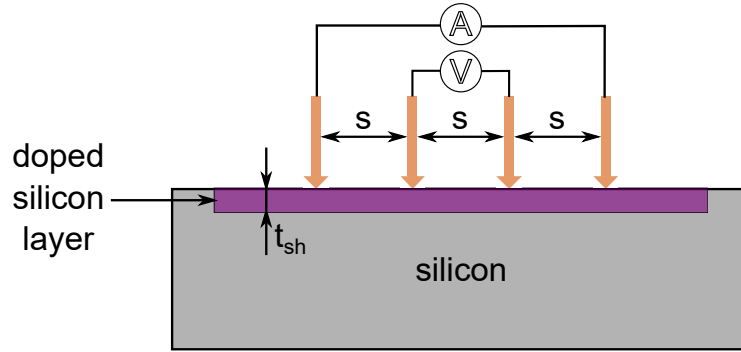


Figure 3.3: Scheme of the four-point probe sheet resistance measurement device. The outer two probes inject current inside the doped silicon layer (with thickness t_{sq}), whereas the inner two probes measure the potential drop. The four probes are placed equidistantly at a distance s . The four-point probe sheet resistance measurement is more accurate than the two-point probe, as there is high parasitic resistance in the two-point probe measurement. The resistance is easily calculated from the supplied constant current $I = 10 \text{ mA}$ and the measured voltage drop V across the two-inner probes. The depletion region (on the doped layer borders) between the doped silicon and the counter polarity acts as insulation, which ensures that the measured potential drop occurs across the doped layer.

Figure 3.3 schematically shows the four-point probe sheet resistance measurement. The measuring head contains 4 contacts aligned equidistantly from each other in a row. The outer two contacts inject current inside the doped film, whereas the inner pair measure the voltage drop across the surface under test. The advantage of the four point probe over the two-point probe is the negligible effect of the parasitic resistances: the wire resistance R_w , the contact resistance R_c for each contact, as well as the spreading resistance R_{sp} . In the two-point probe method, these parasitic resistances distort the voltage measurement due to the voltage drop across each of them. In the four-point probe method, the inner pair of contacts are connected to

a voltmeter which has an ohmic resistance as high as 10^{12} ohms. Consequently, a negligible current will flow through these parasitic contacts, causing the voltage drop across these parasitic resistances to be negligible. As a result, the measured sheet resistance R_{sh} value is much more accurate [53] and relates to the applied constant current $I = 10$ mA and the measured potential drop V through

$$R_{\text{sh}} = \frac{\pi}{\ln(2)} \frac{V}{I}. \quad (3.4)$$

3.4 Secondary Ion Mass Spectroscopy

For validation of the proposed model and understanding how the laser doping process takes place, this work uses secondary ion mass spectroscopy (*SIMS*) for measuring doping profiles. With an accuracy greater than 10^{15} atom/cm³, the SIMS device (Atomika 6500) measures the concentration of the doping atoms in the depth of the silicon surface. Appendix A.2.4 explains in detail how the SIMS works and how the measurement is conducted.

3.5 Laser scanning microscopy

The deformed irradiated wafer surface is examined with a 3D laser scanning microscope from Keyence (VK 9700). The microscope uses a short wavelength laser (a violet laser beam) to capture height information. Appendix sec. A.2.5 illustrates the measurement in detail.

3.6 Profilometer

For thickness measurements of the sputtered sheets, we used the modern Dektak XT produced by Bruker corporation. The measurement resolution is in the range of a few nanometers. For that, a $2 \mu\text{m}$ -head diameter stylus scans the flat polished wafer surface over the edge of the deposited layer. The amplitude of the edge step is the thickness of the layer. Further information about the profilometer system that is used is found in appendix A.2.6.

Chapter 4

Model and Simulation

Laser doping of silicon is too sensitive to the laser processing parameters (pulse energy density H and pulse duration τ_p). Pulse energy density H and pulse duration τ_p define the melt dimensions, melt depth d_{melt} and melt width w_{melt} , the diffusion time, the doping profile and the evaporation of materials. The mechanism with which the lasing parameters and the material interact defines the electrical properties of the resulting doped layer. Understanding of that interaction enables tailoring of doped layers as required. During irradiation, the dopant diffuses from a precursor layer into the melted silicon through one or more of these three forms: solid precursor/liquid silicon, liquid precursor/liquid silicon and gas precursor/liquid silicon. The modeling of each of the preceding cases differs from the others in terms of absorbed energy, species transfer and material recycling. Extensive research has been published on this subject; published models fit specific single cases of the three previously mentioned cases [54–64]. This chapter represents a unified numerical Matlab-based computer model that describes the laser doping process and simulates the three possible cases for doping from a precursor for wide laser energy densities. The model correctly estimates not only the doping profile, but also the melt dimensions (after irradiation). The model uses the finite-difference numerical method to solve the heat equation and the diffusion equation in space and time. The following sections discuss the finite-difference numerical method as well as each sub-process of the doping process.

4.1 Finite-Difference Method

The finite-difference method *FDM* is a numerical technique to discretize and solve differential equations. The discretization of differential equations means approximating differential equations to a set of solvable algebraic equations. Solving the algebraic equations gives an approximate solution of the problem at only discrete instances in space and time. Discretization divides the volume of interest into an aggregate of unit volumes at the center of which lies a point called *mesh point* or *mesh node*. The aggregate of the mesh points is called *mesh* or *nodal network*. The value of any material property at each mesh point is the averaged value of that property in the surrounding unit volume. The accuracy of the numerical solution critically depends on the number of mesh points. The finer the discretization is, the more accurate the obtained solution.

4.1.1 Finite-Difference Forms of the Heat and Diffusion Equations

4.1.1.1 The Heat Equation

The general form of the heat equation in the Cartesian co-ordinates is

$$\frac{\partial}{\partial x} \left(k(T) \frac{\partial T}{\partial x} \right) + \frac{\partial}{\partial y} \left(k(T) \frac{\partial T}{\partial y} \right) + \frac{\partial}{\partial z} \left(k(T) \frac{\partial T}{\partial z} \right) + \dot{q} = \rho(T) c_p(T) \frac{\partial T}{\partial t} \quad (4.1)$$

, where T is the temperature [K], k is the thermal conductivity [W/(m K)], ρ is the density [Kg/m³], and c_p is the heat capacity [J/(Kg K)] of the control volume around the nodal point. The term \dot{q} is the rate of energy generation per unit volume [W/m³] and t is time [s]. In the case of laser doping using line-focused beams, the intensity profile in the long axis direction (in the z-axis direction) is top-hat. Consequently, in the z-axis, the variation in the incidence intensity is negligible. Consequently, the change in temperature in the z-direction is small enough to be ignored, which reduces the problem into a 2D case. Furthermore, assuming that the thermal conductivity k is constant per unit volume, the equation 4.1 reduces to

$$k(T) \left(\frac{\partial^2 T}{\partial x^2} + \frac{\partial^2 T}{\partial y^2} \right) + \dot{q} = \rho(T) c_p(T) \frac{\partial T}{\partial t}. \quad (4.2)$$

Converting the volume of interest into several unit volumes with a network of nodes dictates that some nodes lie inside and other nodes lie at the boundaries of the volume of interest. The nodes inside the volume are called *interior nodes* and those lying at the boundaries are called *boundary nodes*.

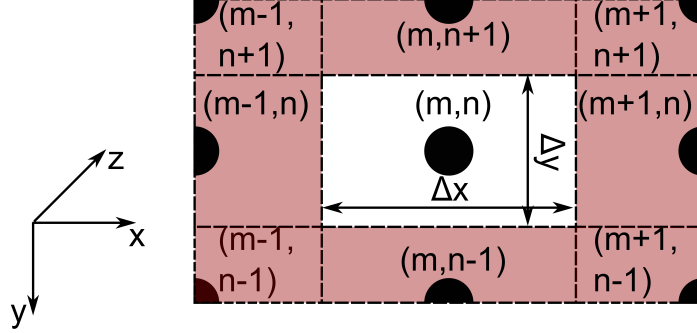


Figure 4.1: Scheme of a small nodal network with one interior node (the node with a white background) and eight boundary nodes (the nodes with a dark pink background color). The interior node is surrounded with a full unit volume, whereas the boundary nodes are surrounded with fractions of one unit volume.

Figure 4.1 demonstrates a part of the used mesh. The white background node (the node with co-ordinates (m, n)) is an interior node. The nodes with a dark pink color are boundary nodes. The interior node is surrounded with one complete unit volume, whereas the boundary nodes are surrounded with fractions of a unit volume. For example, the node $(m-1, n)$ is surrounded by half of a unit volume, while the node (like node $(m-1, n-1)$) at the edge is surrounded by one quarter of a unit volume.

At the interior node (m, n) shown in figure 4.1, the spatial discretization or the finite-difference form approximates the term $\frac{\partial^2 T}{\partial x^2}$ in the heat equation 4.2 to be

$$\begin{aligned} \frac{\partial^2 T}{\partial x^2} &= \frac{\frac{\partial T}{\partial x}|_{m+1, n} - \frac{\partial T}{\partial x}|_{m-1, n}}{\Delta x} = \left(\frac{T_{m+1, n} - T_{m, n}}{\Delta x} - \frac{T_{m, n} - T_{m-1, n}}{\Delta x} \right) / \Delta x \\ &= \frac{T_{m+1, n} + T_{m-1, n} - 2T_{m, n}}{\Delta x^2}. \end{aligned} \quad (4.3)$$

Analogously, the term $\frac{\partial^2 T}{\partial y^2}$ is approximated to

$$\frac{T_{m, n+1} + T_{m, n-1} - 2T_{m, n}}{\Delta y^2}. \quad (4.4)$$

The temporal discretization of the temporal term $\frac{\partial T}{\partial t}$ according to the forward-difference formulation is

$$\frac{\partial T}{\partial t} = \frac{T_{m,n}^{t+1} - T_{m,n}^t}{\Delta t}. \quad (4.5)$$

Substituting eq. 4.3, eq. 4.4 and eq. 4.5 in eq. 4.2 gives

$$\begin{aligned} & \rho(T) c_p(T) \frac{T_{m,n}^{t+1} - T_{m,n}^t}{\Delta t} \\ = & k(T) \left(\frac{T_{m+1,n} - T_{m,n}}{\Delta x^2} - \frac{T_{m,n} - T_{m-1,n}}{\Delta x^2} + \frac{T_{m,n+1} - T_{m,n}}{\Delta y^2} - \frac{T_{m,n} - T_{m,n-1}}{\Delta y^2} \right) + \dot{q}. \end{aligned} \quad (4.6)$$

Multiplying by $\Delta x \Delta y \Delta z$ and re-arranging eq. 4.6 gives

$$\begin{aligned} T_{m,n}^{t+1} = & T_{m,n}^t \\ & + \frac{\Delta t}{\rho(T) c_p(T) \Delta x \Delta y \Delta z} \left(k(T) \left((T_{m+1,n} - T_{m,n}) \frac{\Delta y \Delta z}{\Delta x} \right) \right) \\ & + \frac{\Delta t}{\rho(T) c_p(T) \Delta x \Delta y \Delta z} \left(k(T) \left((T_{m-1,n} - T_{m,n}) \frac{\Delta y \Delta z}{\Delta x} \right) \right) \\ & + \frac{\Delta t}{\rho(T) c_p(T) \Delta x \Delta y \Delta z} \left(k(T) \left((T_{m,n+1} - T_{m,n}) \frac{\Delta x \Delta z}{\Delta y} \right) \right) \\ & + \frac{\Delta t}{\rho(T) c_p(T) \Delta x \Delta y \Delta z} \left(k(T) \left((T_{m,n-1} - T_{m,n}) \frac{\Delta x \Delta z}{\Delta y} \right) \right) \\ & + \frac{\Delta t \dot{q}}{\rho(T) c_p(T)}. \end{aligned} \quad (4.7)$$

Equation 4.7 is the explicit form of the finite-difference heat eq. 4.2 used here. The *explicit method* of solution means that the temperature of a given node at a given time step is calculated using the known temperature from the previous time step.

4.1.1.2 The Diffusion Equation

Fick's second law of diffusion is the general form of the diffusion equation in the Cartesian co-ordinates and has the following formulation

$$\frac{\partial C}{\partial t} = D_c(T) \left(\frac{\partial^2 C}{\partial x^2} + \frac{\partial^2 C}{\partial y^2} + \frac{\partial^2 C}{\partial z^2} \right). \quad (4.8)$$

Provided that the change in laser intensity in the z-direction is negligibly small, the heat generated inside the melted volume is also negligibly small. Thus, the dopant source is homogeneous in the z-direction and the problem is reduced to being two dimensional in x- and y-directions. The 2D simplification of eq. 4.8 is

$$\frac{\partial C}{\partial t} = D_c(T) \left(\frac{\partial^2 C}{\partial x^2} + \frac{\partial^2 C}{\partial y^2} \right). \quad (4.9)$$

Analogous to eq. 4.7, the finite difference form of the simplified diffusion eq. 4.9 is

$$\begin{aligned} & \frac{C_{m,n}^{t+1} - C_{m,n}^t}{\Delta t} \\ = & D_c(T) \left(\frac{C_{m+1,n} - C_{m,n}}{\Delta x^2} - \frac{C_{m,n} - C_{m-1,n}}{\Delta x^2} + \frac{C_{m,n+1} - C_{m,n}}{\Delta y^2} - \frac{C_{m,n} - C_{m,n-1}}{\Delta y^2} \right). \end{aligned} \quad (4.10)$$

Re-arranging eq. 4.10 gives

$$\begin{aligned} C_{m,n}^{t+1} = & C_{m,n}^t \\ & + D_c(T) \Delta t \left(\frac{C_{m+1,n} - C_{m,n}}{\Delta x^2} \right) \\ & + D_c(T) \Delta t \left(\frac{C_{m-1,n} - C_{m,n}}{\Delta x^2} \right) \\ & + D_c(T) \Delta t \left(\frac{C_{m,n+1} - C_{m,n}}{\Delta y^2} \right) \\ & + D_c(T) \Delta t \left(\frac{C_{m,n-1} - C_{m,n}}{\Delta y^2} \right). \end{aligned} \quad (4.11)$$

Equation 4.11 is the explicit form of the finite-difference diffusion eq. 4.9 used in this work.

4.1.2 The Nodal Network

Solving the spatial and the temporal discretized heat and diffusion equations (eq. 4.7 and eq. 4.11) at each node needs a proper discretization of the volume of interest. The finer the discretization is in space and time, the more accurate is the determination of temperature and concentration at any given node. Finer discretization in time and space means using smaller Δt , Δx and Δy , which means more nodes to be calculated for each time step. Similarly, smaller Δt means more calculations for a given period of time, which dictates more computing resources, power and time. For that reason, this work uses the adaptive grid concept to decrease the total number of nodes calculated per time step while increasing the number of nodes in the region of interest, where a more accurate result is needed. In the case of the laser doping process, the region of interest is that directly under the laser beam. Using finer discretization in the region of interest and coarser discretization in the surrounding region dramatically reduces the calculation time, power and resources required without impairing the accuracy of the calculated temperature and concentration [65–68].

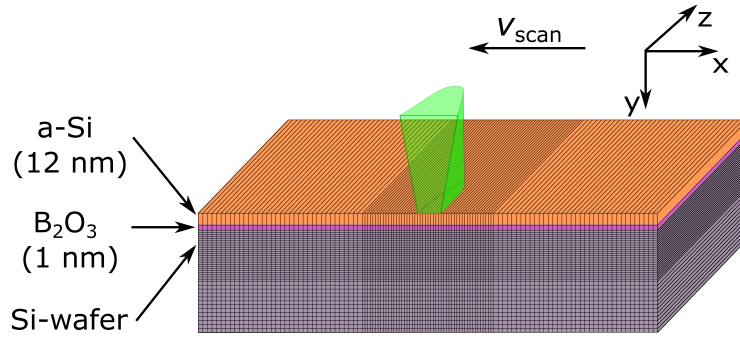


Figure 4.2: The nodal network used in the simulation of the laser doping process. The nodes in the region of interest directly under the laser beam have relatively finer dimensions than the nodes outside to get more accurate results. The precursor layer system consists of an amorphous silicon cap layer and a boron oxide layer acting as the dopant source. The thicknesses Δy_{a-Si} and $\Delta y_{B_2O_3}$ of the amorphous silicon cap layer and the boron oxide layer are 12 nm and 1 nm, respectively. The dimensions of the discretized volume cross section shown in fig. 4.2 are represented by two matrices shown in fig. 4.3 and fig. 4.4.

Figure 4.2 shows the nodal network used in the simulation of the laser doping process. According to the adaptive grid concept, the region of interest directly under the laser beam and the small region surrounding it have more nodes with finer Δx and Δy than the regions far away. The inter-nodal distancing in the x-direction increases laterally from the region of interest outwards and the inter-nodal distancing in the y-direction increases vertically from the region of interest downwards. The finest discretization exists at the center of the surface of the considered volume. The first two layers of the system are the two-layer precursor system, which consists of an amorphous silicon cap layer and the doping atoms source layer (the boron oxide layer). The thickness $\Delta y_{\text{a-Si}}$ of the amorphous silicon cap layer is 12 nm, and the thickness $\Delta y_{\text{B}_2\text{O}_3}$ of the boron oxide layer is 1 nm. Simulation of thicker layers is also possible; if the layer's thickness $\Delta y_{\text{layer}} \leq \Delta y_{\text{Si}}$, the layer remains a single layer, otherwise, the layer is divided into several layers with each having the same thickness.

Δx_4	...	Δx_3	...	Δx_2	...	Δx_1	...	Δx_1	...	Δx_2	...	Δx_3	...	Δx_4
Δx_4	...	Δx_3	...	Δx_2	...	Δx_1	...	Δx_1	...	Δx_2	...	Δx_3	...	Δx_4
\vdots														
Δx_4	...	Δx_3	...	Δx_2	...	Δx_1	...	Δx_1	...	Δx_2	...	Δx_3	...	Δx_4
Δx_4	...	Δx_3	...	Δx_2	...	Δx_1	...	Δx_1	...	Δx_2	...	Δx_3	...	Δx_4

Figure 4.3: Scheme shows the construction of the matrix carrying the x-dimensions of the unit cells constituting the studied volume. The width of the cells decreases proceeding along the rows from outward to the center ($\Delta x_4 > \Delta x_3 > \Delta x_2 > \Delta x_1$). Along the depth of the studied volume, the widths of the rows do not differ.

Figure 4.3 and figure 4.4 schematically demonstrate the matrices carrying the x- and y-dimensions of the cells composing the studied volume. Figure 4.3 represents the widths, whereas figure 4.4 represents the thicknesses of the unit cells. Along the columns, from the surface to the bottom of the matrices, the widths of the unit cells are constant whereas the thicknesses increase. Along the rows, from outwards to the center, the thicknesses are constant, whereas the widths decrease. Finer discretization of the width and thickness of the unit cells in both matrices exist in the middle of the upper row which corresponds to the center of the surface.

This method of discretization allows for a more precise calculation in the region of interest (underneath the irradiating laser beam) without losing precision in the region outside.

$$\begin{array}{c}
 \boxed{\begin{array}{ccccc} \Delta y_1 & \Delta y_1 & \dots & \Delta y_1 & \Delta y_1 \end{array}} \\
 \vdots \\
 \boxed{\begin{array}{ccccc} \Delta y_2 & \Delta y_2 & \dots & \Delta y_2 & \Delta y_2 \end{array}} \\
 \vdots \\
 \boxed{\begin{array}{ccccc} \Delta y_3 & \Delta y_3 & \dots & \Delta y_3 & \Delta y_3 \end{array}}
 \end{array}$$

Figure 4.4: Scheme shows the construction of the matrix carrying the y -dimensions of the unit cells constituting the studied volume. The thickness of the cells decreases proceeding from the bottom to the surface ($\Delta y_3 > \Delta y_2 > \Delta y_1$). The thickness of the cells is constant along the rows.

$$\begin{array}{c}
 \boxed{\begin{array}{ccccc} p_{1,1} & p_{1,2} & \dots & p_{1,N-1} & p_{1,N} \\ p_{2,1} & p_{2,2} & \dots & p_{2,N-1} & p_{2,N} \end{array}} \\
 \vdots \\
 \boxed{\begin{array}{ccccc} p_{M-1,1} & p_{M-1,2} & \dots & p_{M-1,N-1} & p_{M-1,N} \\ p_{M,1} & p_{M,2} & \dots & p_{M,N-1} & p_{M,N} \end{array}}
 \end{array}$$

Figure 4.5: Scheme exhibits the construction of the matrix carrying the properties p of the unit cells constituting the studied volume cross section. Some of the possible properties p are: thermal conductivity k , density ρ , heat capacity c_p , temperature T , concentration C , etc. The property matrix has the same number of rows M and the same number of columns N as the discretization matrices shown in fig. 4.3 and fig. 4.4.

Figure 4.5 shows a scheme of the matrix carrying the properties of the unit cells composing the studied volume cross section. For each unit cell, the property p can be a material property (e.g., thermal conductivity k , heat capacity c_p , density ρ , diffusion coefficient D_c etc.) or a calculated parameter (e.g., temperature T or

concentration C). The matrix has the same dimensions (number of rows N and columns M) as the discretization matrices (fig. 4.3 and fig. 4.4) of the considered volume cross section. According to the numbering shown, the first unit cell exists at the top left of the matrix with the index (1,1), whereas the last unit cell exists at the bottom right of the matrix with the index (M,N).

4.1.2.1 Numerical Calculation Stability

Simulating with the adaptive grid concept without impairing the precision requires stability of the discretization of the heat equation and the diffusion equation. As the explicit method implies, the calculation of a property $p_{m,n}^{t+1}$ at a particular node for a given time $t+1$ requires the knowledge of that particular property $p_{m,n}^t$ at the previous time step t . During calculation, going forward in time convergence on the correct solution for each of the two equations (the 2-D heat equation 4.7 and the 2-D concentration equation 4.11). Achieving the required convergence dictates that the coefficient of the property $p_{m,n}$ at the node of interest in the equations 4.7 and 4.11 at the previous time step t is \geq zero.

One one hand, simplifying the heat equation (eq. 4.7) results in:

$$\begin{aligned}
 T_{m,n}^{t+1} &= T_{m,n}^t + \frac{\Delta t}{\Delta x^2} \alpha_{th}(T) (T_{m+1,n} + T_{m-1,n} - 2T_{m,n}^t) \\
 &\quad + \frac{\Delta t}{\Delta y^2} \alpha_{th}(T) (T_{m,n+1} + T_{m,n-1} - 2T_{m,n}^t) \\
 &= \frac{\Delta t}{\Delta x^2} \alpha_{th}(T) (T_{m+1,n} + T_{m-1,n}) + \frac{\Delta t}{\Delta y^2} \alpha_{th}(T) (T_{m,n+1} + T_{m,n-1}) \\
 &\quad + (1 - \frac{2\Delta t}{\Delta x^2} \alpha_{th}(T) - \frac{2\Delta t}{\Delta y^2} \alpha_{th}(T)) T_{m,n}^t
 \end{aligned} \tag{4.12}$$

, where $\alpha_{th}(T)$ is the term $\frac{k(T)}{\rho(T)c_p(T)}$ and is called *thermal diffusivity* [m²/sec].

Applying the stability criteria, the equality results in:

$$(1 - \frac{2\Delta t}{\Delta x^2} \alpha_{th}(T) - \frac{2\Delta t}{\Delta y^2} \alpha_{th}(T)) \geq 0, \tag{4.13}$$

which implies that the largest time step Δt_{heat} should not exceed

$$\Delta t_{heat} \leq \left(\frac{\Delta x^2 \Delta y^2}{2\alpha_{th}(T) (\Delta x^2 + \Delta y^2)} \right) \tag{4.14}$$

to keep the convergence while calculating the explicit form of the finite difference heat equation (eq. 4.7). The condition in eq. 4.14 is called *Courant-Friedrichs-Lewy*, which correlates the spatial resolution and the maximum time step used for numerical calculation [69].

On the other hand, analogous to eq. 4.12, simplifying eq. 4.11 results in

$$\begin{aligned}
 C_{m,n}^{t+1} &= C_{m,n}^t + \frac{\Delta t}{\Delta x^2} D_c(T) (C_{m+1,n} + C_{m-1,n} - 2C_{m,n}^t) \\
 &\quad + \frac{\Delta t}{\Delta y^2} D_c(T) (C_{m,n+1} + C_{m,n-1} - 2C_{m,n}^t) \\
 &= \frac{\Delta t}{\Delta x^2} D_c(T) (C_{m+1,n} + C_{m-1,n}) + \frac{\Delta t}{\Delta y^2} D_c(T) (C_{m,n+1} + C_{m,n-1}) \\
 &\quad + (1 - \frac{2\Delta t}{\Delta x^2} D_c(T) - \frac{2\Delta t}{\Delta y^2} D_c(T)) C_{m,n}^t.
 \end{aligned} \tag{4.15}$$

Consequently, applying the stability criteria, the maximum usable time step Δt_{diff} that maintains stability is

$$\Delta t_{diff} \leq \left(\frac{\Delta x^2 \Delta y^2}{2D_c(T) (\Delta x^2 + \Delta y^2)} \right). \tag{4.16}$$

The value of $D_c(T)$ used for the calculation of Δt must be the maximum possible value of the diffusion coefficient that can be used in the simulation to guarantee stability during the whole calculation period. Finally, the time step actually used for the simulation process should be smaller than or equal to the smallest time step obtained from equations 4.14 and 4.16.

4.1.2.2 The Interface Properties

Adaptive grid means that the volume of substrate is divided into nodal network-containing regions of different inter-nodal spacing, called the mesh region. This means that the face of an interior node existing at the border between two mesh regions experiences significant changes in material properties with temperature. The main properties are: thermal conductivity k and diffusion coefficient D_c of the border nodes. Due to non-uniform inter-nodal spacing, the simple arithmetic mean of the property p at the interface results in an inaccurate value. A proper formulation is being tackled in the following paragraphs.

Figure 4.6 visualizes two neighboring nodes existing at the boundaries of two neighboring mesh regions. The width of the unit cell on the left is wider than that

at the right. Half of the width of the unit cell of the node (m-1,n) is $\Delta x_{(m-1,n)}/2$ and that of the node (m,n) is $\Delta x_{(m,n)}/2$. A proper formulation of thermal conductivity k_{int} at the interface between the two cells, (m-1,n) and (m,n), is obtained through the heat flux equation:

$$q_{\text{int}} = k_{\text{int}} \frac{\partial T}{\partial x} = k_{\text{int}} \frac{T_{(m-1,n)} - T_{(m,n)}}{\Delta x_{(m-1,n)-(m,n)}}. \quad (4.17)$$

Substituting the term $k_{\text{int}}/\Delta x_{(m-1,n)-(m,n)}$ in eq. 4.17 with a more logical form yields

$$q_{\text{int}} = \frac{T_{(m-1,n)} - T_{(m,n)}}{\Delta x_{(m-1,n)}/k_{(m-1,n)} + \Delta x_{(m,n)}/k_{(m,n)}}. \quad (4.18)$$

The thermal conductivity considered by eq. 4.17 is assumed to be for a homogeneous material, however, the two cells do not have the same thermal conductivity k value. Thus, formulating the equivalent thermal conductivity k_{int} to be dependent on the two homogeneous thermal conductivity $k_{(m-1,n)}$ and $k_{(m,n)}$ values and the widths, $\Delta x_{(m-1,n)}$ and $\Delta x_{(m,n)}$ of both cells is more logical. As a result of that formulation in eq. 4.18, the thermal conductivity k_{int} at the interface is expressed as

$$k_{\text{int}} = \left(\frac{(1 - f_{(m-1,n)})}{k_{(m-1,n)}} + \frac{f_{(m,n)}}{k_{(m,n)}} \right)^{-1}, \quad (4.19)$$

where $f_{(m-1,n)}$ is an interpolation factor and expressed as

$$f_{(m-1,n)} = \frac{\Delta x_{(m,n)}/2}{\Delta x_{(m-1,n)-(m,n)}} = \frac{\Delta x_{(m,n)}}{\Delta x_{(m-1,n)} + \Delta x_{(m,n)}}. \quad (4.20)$$

In the case of equidistant spacing, $\Delta x_{(m-1,n)} = \Delta x_{(m,n)}$, the value of the interpolation factor is $f_{(m-1,n)} = 0.5$, which makes the value of thermal conductivity k_{int} equal

$$k_{\text{int}} = \frac{2 k_{(m-1,n)} k_{(m,n)}}{k_{(m-1,n)} + k_{(m,n)}}. \quad (4.21)$$

The formulation of the thermal conductivity k_{int} in eq. 4.21 is called the *harmonic mean* of property p . Analogous to thermal conductivity k_{int} in eq. 4.19, the diffusion coefficient D_{cint} follows

$$D_{\text{cint}} = \left(\frac{(1 - f_{(m-1,n)})}{D_{\text{c}(m-1,n)}} + \frac{f_{(m,n)}}{D_{\text{c}(m,n)}} \right)^{-1}, \quad (4.22)$$

where $D_{c(m-1,n)}$ and $D_{c(m,n)}$ are the values of the diffusion coefficient of the homogeneous unit cells at the interface. The harmonic mean of the diffusion coefficient is thus expressed as

$$D_{cint} = \frac{2 D_{c(m-1,n)} D_{c(m,n)}}{D_{c(m-1,n)} + D_{c(m,n)}}. \quad (4.23)$$

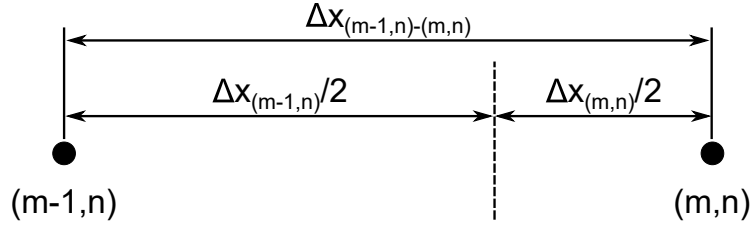


Figure 4.6: The inter-nodal spacing between two neighboring nodes at the borders of two different mesh regions.

Thus, the thermal conductivity formulation (eq. 4.19) and the diffusion coefficient formulation (eq. 4.22) are not only valid inside each mesh region, but also on the boundaries between the mesh regions in the x- and y- directions. Within a mesh region where nodes are equidistant, eq. 4.19 and eq. 4.22 equal the harmonic means (eq. 4.21 and eq. 4.23).

4.2 Laser Doping of silicon

This section illustrates the sub-processes that occur during the laser doping process and how the model considers them. The irradiated substrate is a mono-crystalline silicon wafer with a boron precursor layer on the surface. The surface of the wafer is polished. The boron precursor layer consists of a stack of two deposited layers: a 1 nm thick boron oxide layer covered with a 12 nm thick silicon layer on top of it. The green nanosecond pulsed laser (described in sec. 3.1) irradiates the substrate system. During irradiation, the surface melts, boron diffuses in silicon, and the melted doped silicon re-solidifies. Thus, the laser doping process of silicon consists of two main problems: the heat transfer problem and the mass transfer problem. The subsequent subsections explain in detail each process of the formerly mentioned processes and how the model tackles each.

4.2.1 Heat Transfer Model

4.2.1.1 Heat Source

Section 3.1 described the laser system used to dope a silicon wafer with boron. The laser system emits laser pulses with a Gaussian intensity distribution in the x-direction and a tophat intensity distribution in the z-direction as demonstrated in fig. 3.1. The pulse duration τ_p of the laser pulses measured at $1/e^2$ of maximum intensity I_{\max} varies between 41 ns up to about 250 ns depending on the used pulse width modulation *PWM* and pulse repetition rate f .

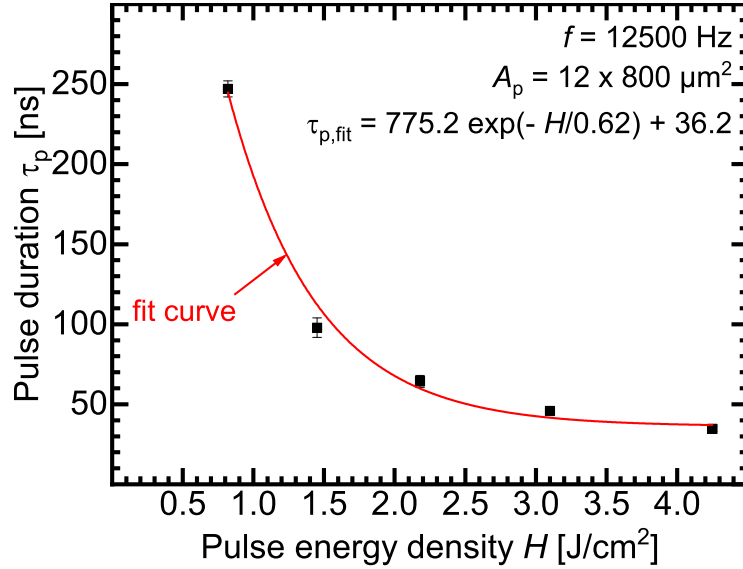


Figure 4.7: The measured pulse duration τ_p of the emitted laser beam used in this work increases with decreasing pulse energy density H . The fit for the experimental data shows that the pulse duration τ_p exponentially increases with decreasing pulse energy density H . The resulting fit equation is then used to obtain the correct pulse duration τ_p as a function of the input pulse energy density H . The measured data are obtained at a pulse repetition rate $f = 12.5$ kHz. The pulse area is $A_p = 12 \times 800 \mu\text{m}^2$.

Figure 4.7 shows the measured pulse duration τ_p of the laser shown in fig. A.1. A photodetector measures the pulse duration τ_p by converting the absorbed number of photons incoming per pulse into an electrical signal. The width of the measured

signal peak at full width half maximum $FWHM$ gives the pulse duration τ_p . The measurement takes place at pulse repetition rate $f = 12500$ Hz and pulse area $A_p = 12 \times 800 \mu\text{m}^2$. The pulse duration τ_p increases with decreasing laser pulse energy density H . The fit for the measured data shows an exponential increase of the pulse duration τ_p with decreasing pulse energy density H . The model uses the resulting fit equation:

$$\tau_p = 775.2 \exp\left(\frac{-H}{0.62}\right) + 36.2. \quad (4.24)$$

to calculate the pulse duration τ_p as a function of the input pulse energy density H .

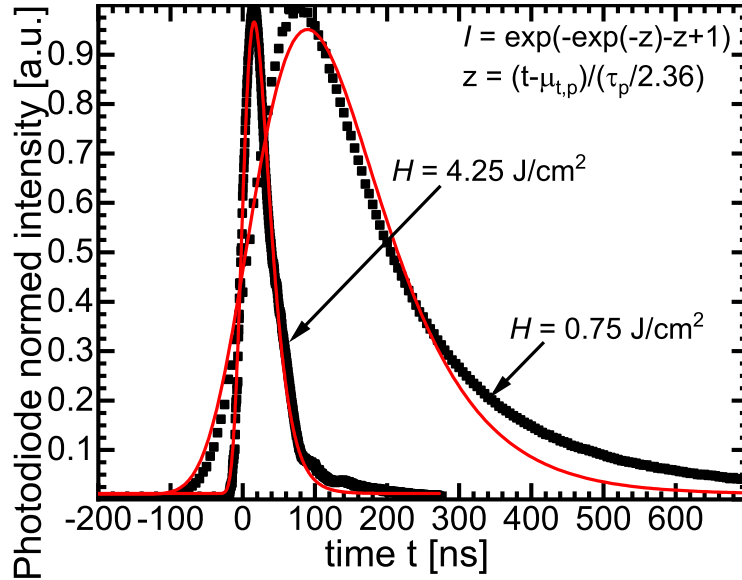
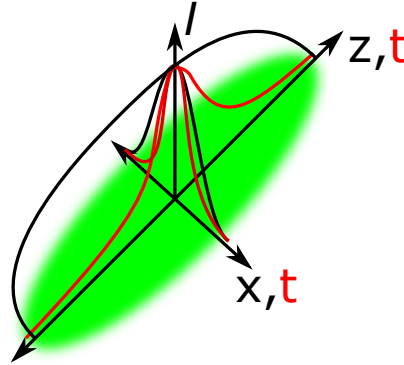


Figure 4.8: The voltage signals measured by the photodetector for the emitted laser pulse at two pulse energy densities $H = 0.75 \text{ J/cm}^2$ and $H = 4.25 \text{ J/cm}^2$ show an asymmetrical temporal Gaussian distribution of the pulse intensity. The absolute amplitude of the resulted voltage signal is directly proportional to the number of absorbed photons per unit time t . The vertical axis represents the normalized amplitude. The model uses the fit equation of the measured peak with the knowledge of the pulse duration τ_p to calculate the portion of the total pulse intensity that reaches the wafer's surface at any moment of time t .

Figure 4.8 shows the measured voltage signal by the photodetector at two pulse energy densities $H = 0.75 \text{ J/cm}^2$ and $H = 4.25 \text{ J/cm}^2$. The number of absorbed photons at any moment of time determines the signal's amplitude. The representa-

tion of the voltage signal on the time axis gives not only the pulse duration τ_p of the emitted pulses, but also the temporal intensity distribution. The measurement exhibits an asymmetrical Gaussian distribution of the laser intensity over time t . The fit peak equation of the measured voltage signal calculates the intensity of the laser at any moment of time during the pulse lifetime. The model uses this fit equation to correctly calculate the laser energy delivered to the wafer's surface at each time step t .

Figure 4.9 schematically shows the spatial and the temporal intensity distribution of the laser pulse. Spatially, the pulse shows a Gaussian intensity distribution in the x -direction and top-hat intensity distribution in the z -direction. Temporally, the intensity distribution has an asymmetrical Gaussian distribution over the pulse life time, as demonstrated in figure 4.8.



laser pulse

Figure 4.9: Scheme of the spatial and temporal intensity distributions of the incident laser pulse. The spatial intensity distribution has a Gaussian shape in the x -direction and a top-hat shape in the z -direction. The temporal intensity distribution has an asymmetric Gaussian shape as demonstrated in fig. 4.8.

To summarize, the model used the knowledge of the spatial and temporal intensity distribution forms to calculate the incident laser energy E_{inc} to the irradiated surface at any given moment of time as follows

$$E_{\text{inc}} = \left(\frac{E_p}{\sqrt{\pi/2}\omega_{x,p}l\tau_p} \right) \exp \left(-\frac{(x - \mu_{x,p})^2}{2\sigma_{x,p}^2} \right) \exp \left(-\exp \left(\frac{\mu_{t,p} - t}{\omega_{t,p}} \right) - \left(\frac{t - \mu_{t,p}}{\omega_{t,p}} \right) + 1 \right), \quad (4.25)$$

where the term $(E_p/(\sqrt{\pi/2}\omega_{x,p}l\tau_p))$ norms the total incident pulse energy spatially and temporally. The term $\exp((x - \mu_{x,p})^2/(2\sigma_{x,p}^2))$ considers the spatial Gaussian distribution of intensity at any position x . Finally, the last term $\exp \left(-\exp \left(\frac{\mu_{t,p} - t}{\omega_{t,p}} \right) - \left(\frac{t - \mu_{t,p}}{\omega_{t,p}} \right) + 1 \right)$ considers the asymmetric temporal intensity distribution at moment t . The mean of the spatial and temporal intensity distributions are $\mu_{x,p}$ and $\mu_{t,p}$, whereas $\omega_{x,p}$ and $\omega_{t,p}$ are the width of the symmetric and asymmetric Gaussian distributions, respectively. The values of $\omega_{x,p}$ and $\omega_{t,p}$ are $\omega_{x,p} = 2\sigma_{x,p} = 6 \mu\text{m}$ and $\omega_{t,p} = \tau_p/2.36$. Note that the pulse duration τ_p is the peak's width at FWHM, whereas $2\omega_{t,p}$ is the peak's radius at $1/e^2$.

4.2.1.2 Laser-Silicon Interaction

During the laser doping process, a line-focused nanosecond pulsed laser with a wavelength $\lambda = 532 \text{ nm}$ perpendicularly irradiates the silicon wafer with the precursor layer on the top of it. The reflected portion of the laser energy is expressed as [41, 70, 71]

$$R = \frac{(n_{\text{Si}} - 1)^2 + n_{\text{Si}}^2 \kappa_{\text{Si}}^2}{(n_{\text{Si}} + 1)^2 + n_{\text{Si}}^2 \kappa_{\text{Si}}^2}, \quad (4.26)$$

where n_{Si} and κ_{Si} are the refractive index and the extinction factor of silicon. The values of n_{Si} and κ_{Si} are obtained from the formulas displayed in appendix A.1.1. The absorbed portion of laser energy is absorbed in the depth of the silicon wafer according to Beer's law:

$$E_{\text{trans}} = E_{\text{inc}}(1 - R)(1 - \exp(-\alpha_{\text{Si}}y)), \quad (4.27)$$

where the term $(1 - R)$ considers the non-reflected part of the incident energy. The terms E_{inc} and E_{trans} are the incident and transmitted laser energy, α_{Si} is the absorption coefficient and y is the depth. The values of the absorption coefficient α_{Si} are obtained from appendix A.1.1. For silicon melting, the wavelength of the laser used for doping of silicon plays a crucial rule. Silicon is an indirect bandgap

material, and thus, has no sharp absorption edge $E_{\text{ph, th}}$. The bandgap energy $E_{\text{g, indirect}}$ of silicon at room temperature $T_0 = 300$ K is 1.12 eV [72]. The photon energy E_{ph} of the green laser with wavelength $\lambda = 532$ nm is about 2.33 eV. The corresponding absorption coefficient α_{th} of silicon at room temperature $T_0 = 300$ K is about 7850 cm^{-1} , which corresponds to an absorption length $l_{\text{abs}} = 1.3 \text{ }\mu\text{m}$ [72–74]. The thickness of the substrate is about $160 \text{ }\mu\text{m}$, which is sufficient to absorb almost all of the non-reflected laser intensity. The laser intensity $I_{\text{ref}}(\lambda = 532 \text{ nm})$ reflected on the polished silicon surface at room temperature $T_0 = 300$ K is about 37% [74].

4.2.1.3 Heating Phase

During the heating phase, it is essential to understand the mechanism of laser absorption in silicon. The optical, thermal and mechanical properties of silicon vary with temperature T according to the equations in appendix A.1.2.

After irradiation starts ($0 < t < \tau_p$), the silicon surface at room temperature T_0 absorbs $1/e$ of the non-reflected fraction, which is about 63% of the incoming laser intensity, at a depth $l_{\text{abs, Si}}$ of $1.3 \text{ }\mu\text{m}$. The absorbed optical energy is converted into thermal energy. The heat generated is considered the heat source, which is the term \dot{q} in the 2-D heat equation 4.2. The temperature T of the region, where laser irradiation is absorbed, gradually increases and leads to local variation in the properties of silicon.

The optical properties of silicon like the real and imaginary refractive index parts, n_{Si} and k_{Si} , as well as the absorption coefficient $\alpha_{\text{abs, Si}}$ vary with changing temperature. Equation 4.26 uses the values of n_{Si} and k_{Si} to calculate the reflectance $R_{\text{c-Si}}$ on the polished flat silicon surface. The reflectance $R_{\text{c-Si}}$ increases with temperature T . The data of the dependencies of the refractive index real part n_{Si} and the absorption coefficient α_{Si} of solid crystalline and liquid are mentioned in appendix A.1.1 and A.1.2.

4.2.1.4 Phase Transformation

During phase transformations, numerical calculation instability is likely to occur, due to the high latent heat of fusion $H_{\text{melt, Si}}$. An approximation of heat capacity c_p through a Gaussian distribution function with a standard deviation of ΔT avoids the instability of the numerical simulation upon phase changing [75]. The approximation

not only smooths the strong change of the heat capacity $c_{p,\text{Si}}$, but also includes both latent heats, which include the heat of fusion $H_{\text{melt,Si}}$ and the heat of evaporation $H_{\text{evap,Si}}$ as follows:

$$c_{p\text{Si}, \text{ smooth}} = c_{p,\text{Si}} + \frac{H_{\text{melt,Si}}}{(\Delta T \sqrt{\pi/2})} \exp\left(\frac{-2 (T - T_{\text{melt,Si}})^2}{\Delta T^2}\right) + \frac{H_{\text{evap,Si}}}{(\Delta T \sqrt{\pi/2})} \exp\left(\frac{-2 (T - T_{\text{evap,Si}})^2}{\Delta T^2}\right). \quad (4.28)$$

The area under the Gaussian distribution at temperature $T_{\text{melt/evap,Si}} \pm \Delta T$, where ΔT equals 10 degrees, is the enthalpy needed for phase changing. The simulation uses the smoothed heat capacity $c_{p,\text{Si}, \text{ smooth}}$ as the heat capacity of silicon.

4.2.1.5 Melting the Silicon Surface

From eq. A.1 and A.3, not only the refractive index n_{Si} but also the absorption coefficient $\alpha_{\text{abs,Si}}$ of silicon increase with increasing temperature of the silicon bulk. As a result, the absorption length $l_{\text{abs,Si}}$ decreases which pushes the absorption region and the heat generation region towards the surface. As a result, the temperature of the surface of silicon significantly increases relative to the bulk of the silicon substrate until fusion. The extinction factor of the melted silicon is 4.87 [76]. Using eq. A.2, the absorption depth $l_{\text{abs,Si}}$ of the melted silicon ($T = T_{\text{melt,Si}} = 1687$ K [76]) for the green laser with wavelength $\lambda = 532$ nm is about $l_{\text{abs,Si}} = 8.7$ nm below the surface [77].

4.2.1.6 Evaporation of the Silicon Surface

From eq. 4.27, when irradiation starts, the first $1.3 \mu\text{m}$ depth beneath the flat silicon surface absorbs almost 64% of the incoming non-reflected laser radiation. The absorbed radiation raises the temperature locally, which decreases the absorption length ($l_{\alpha} \approx 9$ nm at $T = T_{\text{melt,Si}}$). Consequently, the heat generation region is pushed to the first layer and leads to a rapid rise in the superficial temperature T_{surf} . If the pulse energy density H is high enough, the surface evaporates.

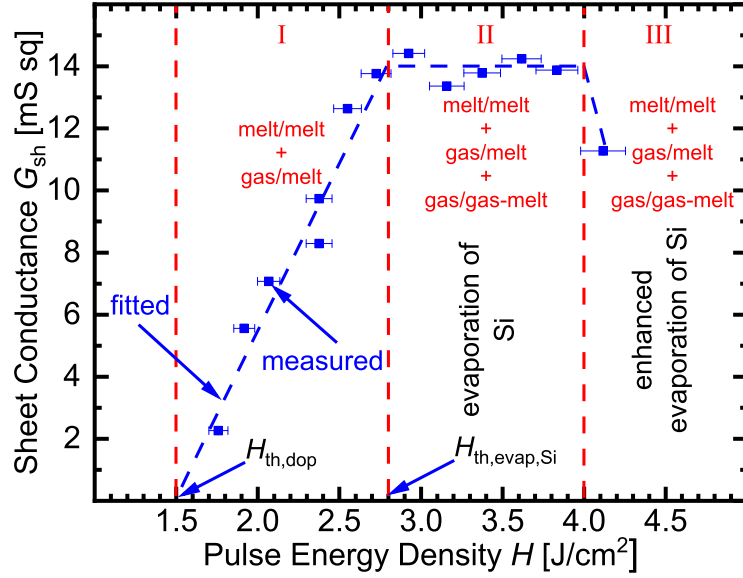


Figure 4.10: The measured sheet conductance G_{sh} of a doped silicon surface with a precursor layer consisting of a 12 nm thick a -Si cap layer and a 1 nm thick boron oxide layer using the laser system introduced in sec. 3.1 versus the used pulse energy density H . The doping threshold pulse energy density is $H_{th,dop} = 1.5 \text{ J/cm}^2$. In regime I, the sheet conductance G_{sh} increases linearly for pulse energy density $H > 1.5 \text{ J/cm}^2$ until $H = 2.8 \text{ J/cm}^2$. At $H > 2.8 \text{ J/cm}^2$, the linear increment of sheet conductance G_{sh} stops and further increasing pulse energy density H does not change the sheet conductance G_{sh} (regime II). In other words, in regime II, as H increases, the gain of the doping material is compensated by the loss of the doping atoms due to evaporation of a portion of the doped silicon surface. Therefore, $H = 2.8 \text{ J/cm}^2$ is the threshold pulse energy density $H_{th,evap,Si}$ for silicon evaporation. For pulse energy density $H > 4 \text{ J/cm}^2$, the material loss overcomes the dopant gain which causes a reduction in the sheet conductance G_{sh} . Melt/melt, gas/melt and gas/gas-melt are the three main types of doping processes occurring in regime I, II and III, respectively.

Figure 4.10 shows the calculated sheet conductance G_{sh} from the measured sheet resistance R_{sh} of a laser doped silicon surface with a deposited boron-rich precursor layer versus the used pulse energy density H . The two sputtered layers of the precursor layer consists of a 12 nm amorphous silicon $a-Si$ layer and a 1 nm boron oxide B_2O_3 layer. A laser beam irradiates the surface, which enables the diffusion of

boron atoms into the melted silicon surface. As indicated by the plotted results, the pulse energy density H range is divided into three main regimes. Regime I starts at the doping threshold pulse energy density $H_{\text{th,dop}} = 1.5 \text{ J/cm}^2$. For $1.5 \text{ J/cm}^2 < H < 2.8 \text{ J/cm}^2$ (regime I), increasing the used pulse energy density H linearly increases the sheet conductance G_{sh} . This means that the gain in the amount of dopant material linearly increases with the used pulse energy density H . In Regime II ($2.8 \text{ J/cm}^2 < H < 4.0 \text{ J/cm}^2$), as H increases, the sheet conductance G_{sh} remains almost constant, indicating that the gain of dopant material is compensated by a loss of material. This is only possible when evaporation of parts of the surface occurs. Thus, $H = 2.8 \text{ J/cm}^2$ is considered to be the threshold pulse energy density $H_{\text{th,evap,Si}}$ of silicon evaporation. In regime III ($H > 4.0 \text{ J/cm}^2$), sheet conductance G_{sh} decreases, which indicates that the loss of dopant materials exceeds the gain. Therefore, regime II is considered to be of technological importance, whereas regime III is considered the regime where enhanced evaporation takes place. Regimes I, II and III correspond to melt/melt-doping, gas/melt-doping and gas/gas-melt-doping, respectively.

4.2.1.7 Temperature-Time Curve

Figure 4.11 shows the calculated surface temperature-time during laser irradiation of silicon. The temporal form of the laser pulse is also plotted versus time t . For the calculation of the temporal form of the used laser pulse, the equation mentioned in fig. 4.8 is used.

Figure 4.11a demonstrates the calculated surface temperature T_{surf} of the center of the silicon surface during irradiation with pulse energy density $H = 1.77 \text{ J/cm}^2$ (pulse duration $\tau_p = 77 \text{ ns}$). The maximum temperature T_{surf} is about 2200 K and is reached shortly after the peak of the temporal form. After the pulse is off, the hot molten surface cools down to the melting temperature $T_{\text{melt,Si}} = 1687 \text{ K}$ [76]. After losing the latent heat of fusion, the surface resolidifies again.

Figure 4.11b represents the T_{surf} -time curve when pulse energy density $H = 3.45 \text{ J/cm}^2$ (pulse duration $\tau_p = 43 \text{ ns}$) is used. At the peak of the temporal form of the laser pulse, the maximum temperature T_{surf} of the silicon surface reaches and holds at the evaporation temperature of silicon $T_{\text{evap,Si}} = 3538 \text{ K}$ [78, 79] and consumes the extra absorbed energy to evaporate. After the end of the laser pulse duration,

the evaporation phase ends and the cooling phase decreases the temperature T_{surf} to the melting temperature $T_{\text{melt,Si}}$. The hot molten silicon continues to lose energy until the whole surface is resolidified.

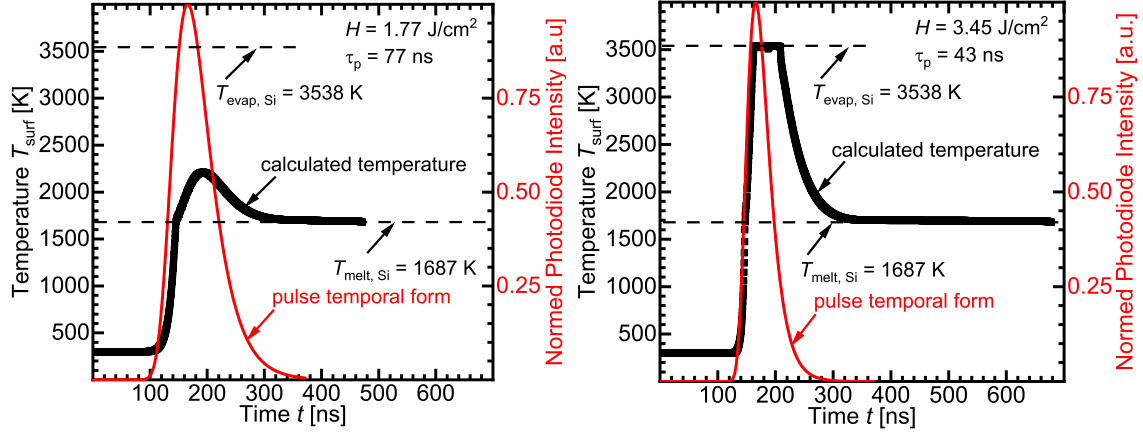


Figure 4.11: The calculated temperature-time curve (the thick black points) of the center of the silicon surface during the irradiation process and the temporal form (the thin red line) of the used laser pulse obtained from the fit equation mentioned in fig. 4.8. a) The pulse energy density $H = 1.77 \text{ J/cm}^2$, pulse duration $\tau_p = 77 \text{ ns}$, heats and melts the silicon surface to a maximum temperature T_{surf} of about 2220 K. The complete melt duration is about 450 ns. b) Using a higher pulse energy density $H = 3.45 \text{ J/cm}^2$ (pulse duration $\tau_p = 43 \text{ ns}$) heats, melts and evaporates parts of the silicon surface. This is observed in the maximum temperature T_{surf} reached during the irradiation, which is the evaporation temperature of silicon $T_{\text{evap,Si}} = 3538 \text{ K}$ [78, 79].

4.2.1.8 Model Validation

The current section discusses the procedures followed to validate the heat transfer model.

4.2.1.8.1 Experimental

It is challenging to measure the temperature T_{surf} of a hot silicon surface during irradiation that takes only a few hundred nanoseconds. Consequently, validating the model with this method is nearly impossible with our facilities. Therefore,

finding another method is the only option to validate our heat transfer model.

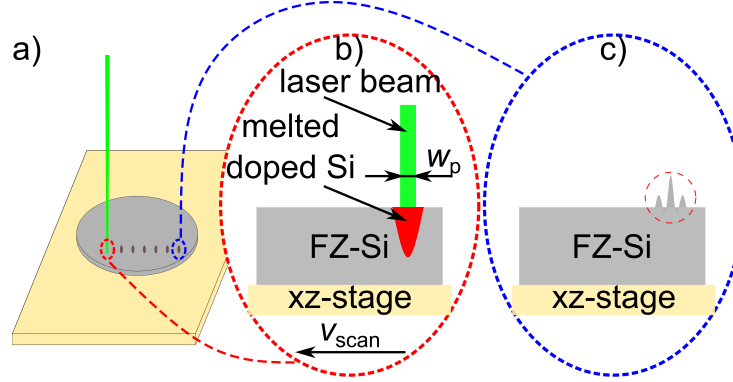


Figure 4.12: Scheme of the experiment used to investigate the surface morphology results from irradiating a well polished wafer surface. a) A chemically and mechanically polished float zone silicon wafer is cleaned with HF-dip to remove the native silicon oxide layer prior to irradiation. The oxide-free wafer is placed on a porous ceramic translational table in the x - z plane. The wafer is fixed on the porous ceramic table during processing using a vacuum pump. b) With a high scanning speed v_c , the laser beam irradiates the wafer with no overlap between the irradiated areas. c) The temperature gradient-induced surface tension gradient across the melted silicon surface together with the density anomaly of silicon upon melting cause a fluid circulation. Therefore, the resolidified surface is no longer flat, but deformed. The resulting surface deformation is investigated using the laser scanning microscope LSM mentioned in sec. 3.5

Figure 4.12a shows the experiment that validates the heat transfer model mentioned in this work. A chemical and mechanical polished n-type float zone silicon wafer (FZ-Si wafer) with a 4 inch diameter and a $250\ \mu\text{m}$ thickness is cleaned by dipping in a 5% HF solution for 30 seconds to remove the native-grown silicon oxide layer from both surfaces. The clean, oxide-free FZ wafer is then irradiated with the laser system introduced in sec. 3.1. The wafer is placed on the porous ceramic plate under the objective lens. A vacuum pump fixes the wafer on the stage during laser processing.

Figure 4.12b schematically shows the laser beam irradiating the surface with a variable pulse energy density ranging from $H = 1.77\ \text{J}/\text{cm}^2$ to $H = 4.97\ \text{J}/\text{cm}^2$ (the maximum obtainable energy density for the system). No overlap between the

irradiated areas occurs through adjusting the scanning speed v_{scan} . Increasing the scanning speed v_{scan} increases the pulse-pulse distance x_{irr} between the successive pulses.

Figure 4.12c shows a scheme of the resolidified silicon surface after the pulse ends. Due to the Gaussian intensity distribution of the laser pulse, the middle of the irradiated area heats up, melts and may evaporate faster than the rest of the surface. The temperature gradient-induced surface tension gradient extends along the molten silicon surface [44, 80–82] and the density anomaly of silicon [81, 83] moves the melt. After resolidification, a deformation of the surface remains and does not remelt by proceeding laser pulse(s). The laser scanning microscope *LSM* mentioned in sec. 3.5 investigated the surface textures after irradiation.

4.2.1.8.2 Melt Dimensions' Validation

The melt dimensions resulting from both models (with and without considering evaporation phenomenon) are compared to the LSM data (melt width w_{melt} and depth d_{melt}). Validation means that the model w/ evaporation predicts the results more accurate than the model w/o evaporation. To measure melt width w_{melt} , the *LSM* mentioned in appendix A.2.5 is used to investigate the surface morphology of the irradiated float zone silicon wafer that resulted from the experiment mentioned in 4.2.1.8.1. The measured doping profiles were used to deduce the melt depth d_{melt} .

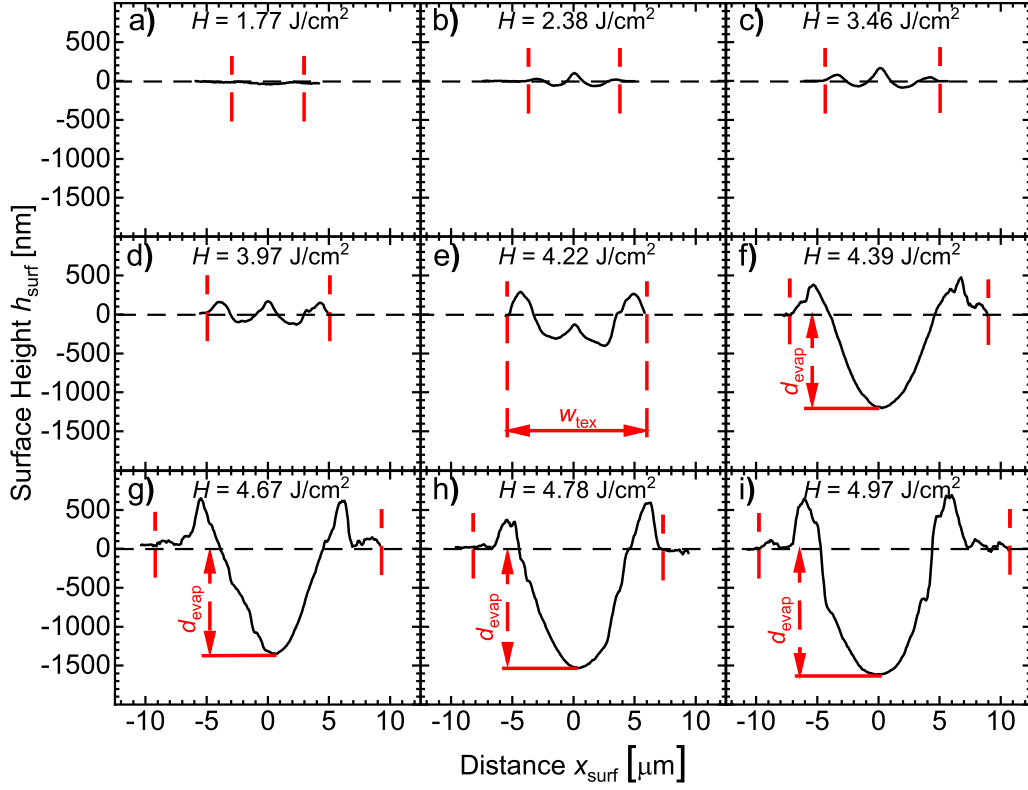


Figure 4.13: The surface textures captured by the laser scanning microscope LSM after irradiation of the flat silicon surface. In a), the used laser pulse energy density $H = 1.77 \text{ J/cm}^2$ barely textured the surface. b) The used pulse energy density $H = 2.38 \text{ J/cm}^2$ left behind a middle peak and relatively shorter satellite side peaks stemming from the thermocapillary effect [81]. c) Using a higher pulse energy density $H = 3.46 \text{ J/cm}^2$ increases the height of the resulting peaks. d) As the pulse energy density H further increases, the evaporation of silicon increases to a point that the height of the middle peak is almost level with the side satellite peaks. Note that evaporation occurs at the center of the melted surface as a result of the Gaussian intensity distribution of the irradiating laser beam. e) The pulse energy density $H = 4.22 \text{ J/cm}^2$ further enhances evaporation at the middle of the melted area, which causes the middle peak height to be lower than the two satellite peaks. f), g), h) and i) Replacing the middle peak with a deep tube-like capillary with depth d_{evap} results in severe evaporation taking place during irradiating with pulse energy density $H \geq 4.22 \text{ J/cm}^2$. The width w_{tex} of the textures also increases with pulse energy density H .

Figure 4.13 shows surface textures captured by the laser scanning microscope *LSM* for the irradiated FZ wafer shown in figure 4.12a. Figure 4.13a shows that using a low pulse energy density $H = 1.77 \text{ J/cm}^2$ leaves a non-detectable surface texture. Using $H_{\text{th,evap,Si}} = 2.38 \text{ J/cm}^2$, as in fig. 4.13b, melts more volume of silicon. This not only indicates the effect of the density anomaly of silicon upon melting, but also the surface tension gradient induced by the temperature gradient [81]. Therefore, the peak left in the middle of the structure is a more easily detected peak. Furthermore, the thermocapillary effect becomes stronger, leading to the formation of the two small satellite peaks on both sides of the middle peak. Figure 4.13c shows that the height of the middle peak and the height of the two satellite peaks become higher as pulse energy density H increased to $H = 3.46 \text{ J/cm}^2$. The pulse energy density $H = 3.97 \text{ J/cm}^2$ shown in figure 4.13d demonstrates that the height of the middle peak is almost at the same level as that of the two satellite peaks. This is due to the evaporation of parts of the silicon surface as the pulse energy density exceeds $H = 2.8 \text{ J/cm}^2$ as shown in fig 4.10. In figure 4.13e, the height of the middle peak is much lower than that of the two satellite peaks. It is very likely that this is due to higher evaporation of parts of the silicon surface. As the used pulse energy density H increases ($H > 4 \text{ J/cm}^2$), as in figures 4.13f, 4.13g, 4.13h and 4.13i, the middle peak disappears and a deep tubelike capillary is left over. This is due to enhanced evaporation at the center of the irradiated silicon surface. The enhancement of evaporation results from the extra absorbed energy due to the geometrical form of the melted surface. The deep tube-like capillary reflects the incident laser radiation multiple times on its wall, which increases the chance for absorption of more energy [84]. Consequently, as pulse energy density $H > 4 \text{ J/cm}^2$, more materials are evaporated and a wider deformed area is left over. Furthermore, a deeper tube-like capillary results, as indicated in figure 4.10.

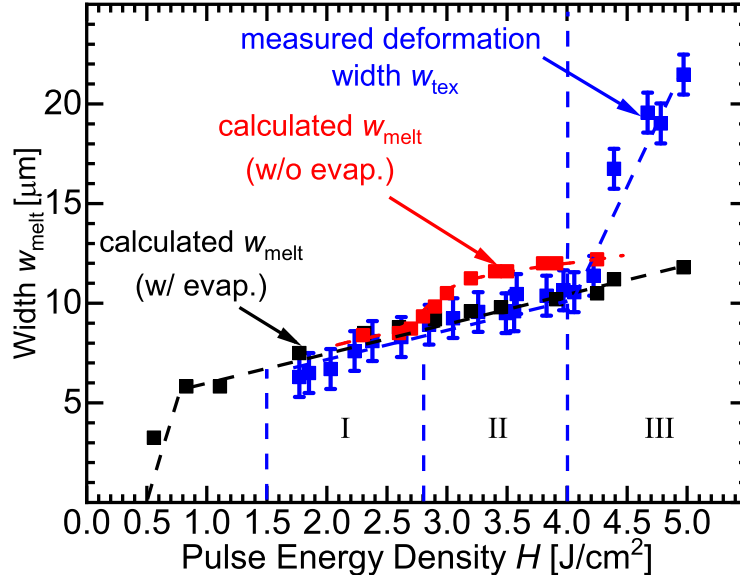


Figure 4.14: The measured melt width w_{melt} is considered to be the texture width w_{tex} . In Regime I (between the doping threshold energy $H_{\text{th,dop}} = 1.5 \text{ J/cm}^2$ until the evaporation threshold $H_{\text{th,evap,Si}} = 2.8 \text{ J/cm}^2$), there is a very good agreement between the measured widths w_{tex} and those simulated by the two models (with- and without-evaporation). In Regime II (between the evaporation threshold $H_{\text{th,evap,Si}} = 2.8 \text{ J/cm}^2$ and the evaporation enhancement threshold $H = 4.0 \text{ J/cm}^2$), the model w/ evaporation agrees with the measured width w_{tex} better than the model w/o evaporation. The overestimated w_{melt} by the model w/o evaporation is due to the consumption of the extra absorbed energy above evaporation threshold to widen and deepen the melt volume instead of evaporation. In regime III at $H > 4.0 \text{ J/cm}^2$, the two models are not able to correctly predict the measured w_{tex} . Possible explanations are: 1) neglecting the increment of the thermal conductivity k_{Si} as a result of the melt motion-assisted heat transfer, 2) the absorption of the radiation in the tube-like capillary in the x -direction may be higher than in the y -direction and 3) the melt splashes due to vigorous melt evaporation.

Figure 4.14 compares the measured and the calculated melt width w_{melt} using two models. One model considers the evaporation of silicon and the other does not. The measured texture width w_{tex} obtained from fig. 4.13 is considered to be the measured melt width w_{melt} . In the no evaporation regime (regime I), there is strong agreement between the measured width w_{melt} and the calculated melt width w_{melt}

by both models. Since in regime I no evaporation occurs, both models predicted the melt width w_{melt} correctly. In the regime where evaporation occurs (regime II), the model neglecting the evaporation of silicon overestimated the melt width w_{melt} as a result of overheating the melted silicon. On the other hand, the model that considers the evaporation of silicon correctly predicted the measured melt width w_{tex} . Starting from regime III, where evaporation of silicon is enhanced, the two models fail to predict the measured width w_{tex} . Possible explanations for the incorrect prediction of width w_{melt} are:

- neglecting the increment of the thermal conductivity k_{Si} as a result of melt circulation/convection-assisted heat transfer,
- stronger lateral (in the x-direction) absorption of laser radiation than perpendicular (in the y-direction) absorption during the multiple reflection on the walls of the tube-like capillary melted surface,
- the covering of the correct melt width w_{melt} by melt splashes taking place during strong evaporation.

Figure 4.15 demonstrates the melt depth d_{melt} calculated from both models, w/ and w/o considering the evaporation process, in comparison to the melt depth d_{melt} extracted from fig. 4.18 and fig. 4.19. The melt depth d_{melt} , at which the extension of the SIMS-measured doping profile (shown in fig. 4.18 and fig. 4.19) intersects the depth d axis at concentration $C_{\text{B}} \approx 10 \text{ cm}^{-3}$, is considered to be the measured melt depth d_{melt} . For regime I and below, no evaporation of silicon takes place, therefore, the measured and the calculated melt depth d_{melt} show a good agreement with both models. In regime II, where evaporation of parts of the melted silicon surface occurs, the model w/o evaporation overestimates the melt depth d_{melt} due to the extra absorbed energy which is not used to compensate latent heat of evaporation, but to melt more silicon. The model w/ evaporation strongly agrees with the measured melt depth d_{melt} . Even in regime III, where evaporation of parts of the silicon surface is enhanced, the calculated melt depth d_{melt} under the model w/ evaporation demonstrates a better agreement with the measured d_{melt} .

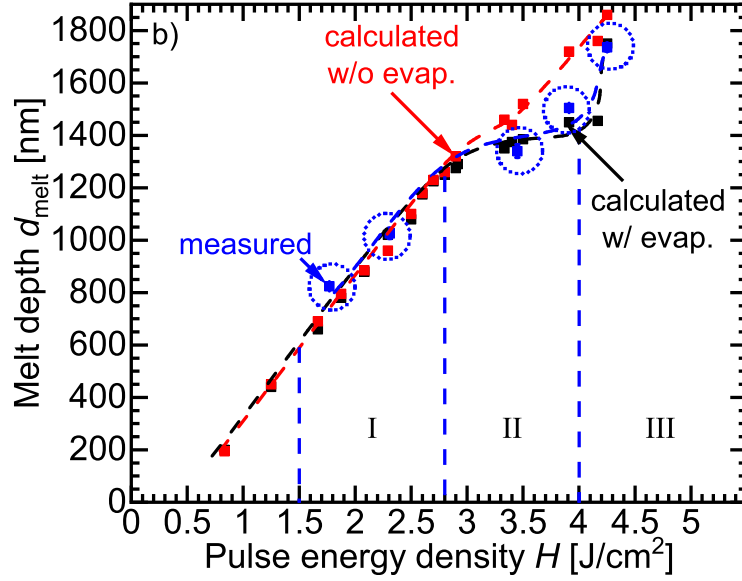


Figure 4.15: The calculated melt depth d_{melt} agrees with the melt depth (surrounded by blue dotted circles) extracted from fig. 4.18 and fig. 4.19. The intersection between the extension of the doping profiles (shown in fig. 4.18 and fig. 4.19) with the depth d axis at concentration of $C_B = 10 \text{ cm}^{-3}$ is considered to be the measured melt depth d_{melt} . In the no evaporation regime (regime I), the measured and the calculated melt depth d_{melt} agree well. As the evaporation regime (regime II) begins, the measured melt depth d_{melt} deviates from the calculated depth using the w/o evaporation model. The w/ evaporation model shows significantly better agreement between the calculated and the measured melt depth d_{melt} . In Regime III, where evaporation is enhanced, the calculated depth d_{melt} matches the measured depth very well. Deepening and widening of the melted area instead of compensating the latent heat of evaporation $H_{\text{evap}, \text{Si}}$ of silicon leads to a linear increase in the depth d_{melt} with pulse energy density H as stated by the results from the w/o evaporation model.

4.2.2 Mass Transfer Model

4.2.2.1 Diffusion Processes

The doping of a silicon surface with boron atoms occurs through laser irradiation of a deposited boron-containing precursor layer lying on a clean oxide-free silicon

surface. The precursor layer system consists of two layers: a 12 nm thick amorphous silicon $a - Si$ layer and underneath, a 1 nm thick boron oxide layer acting as a boron-atoms source. Since boron oxide B_2O_3 and amorphous silicon $a - Si$ layers have lower melting temperatures than crystalline silicon, they melt before crystalline silicon during the laser doping process. It is clear that there is no difference between the amorphous silicon $a - Si$ and the crystalline silicon after melting, however, for convenience, we use the terms of the amorphous and crystalline silicon to simplify the steps of the complicated doping process. The melting temperature of boron oxide B_2O_3 , amorphous silicon $a - Si$ and of crystalline silicon are $T_{\text{melt}, B_2O_3} = 723 \text{ K}$ [85, 86], $T_{\text{melt}, a-Si} = 1420 \text{ K}$ [87] and $T_{\text{melt}, Si} = 1687 \text{ K}$ [76], respectively. Consequently, the liquid/liquid diffusion type takes place as soon as the amorphous silicon $a - Si$ layer melts ($T_{\text{surf}} = T_{\text{melt}, a-Si} = 1420 \text{ K}$), as the boron oxide layer is already in a liquid state. In other words, the diffusion process occurs between the two melted precursor layers before the crystalline silicon melts. After the evaporation of the boron oxide layer, the boron atoms doped in the amorphous silicon $a - Si$ layer diffuse in the freshly-melted crystalline silicon $c - Si$. Furthermore, the boron atoms in the vaporized boron oxide B_2O_3 further diffuse from the gaseous phase into the liquid crystalline silicon. In other words, the laser doping process of silicon from a precursor layer (containing amorphous silicon $a - Si$ and boron oxide B_2O_3) contains the following two doping cases: melt/melt and gas/melt doping. If the used pulse energy density $H > H_{\text{th}, \text{evap}, Si} = 2.8 \text{ J/cm}^2$, parts of the melted silicon surface evaporate leading to the gas/gas-melt diffusion type. The evaporated boron oxide B_2O_3 must first diffuse through the evaporated silicon to reach the melted crystalline silicon, therefore, this case is a gas/gas-melt doping type process.

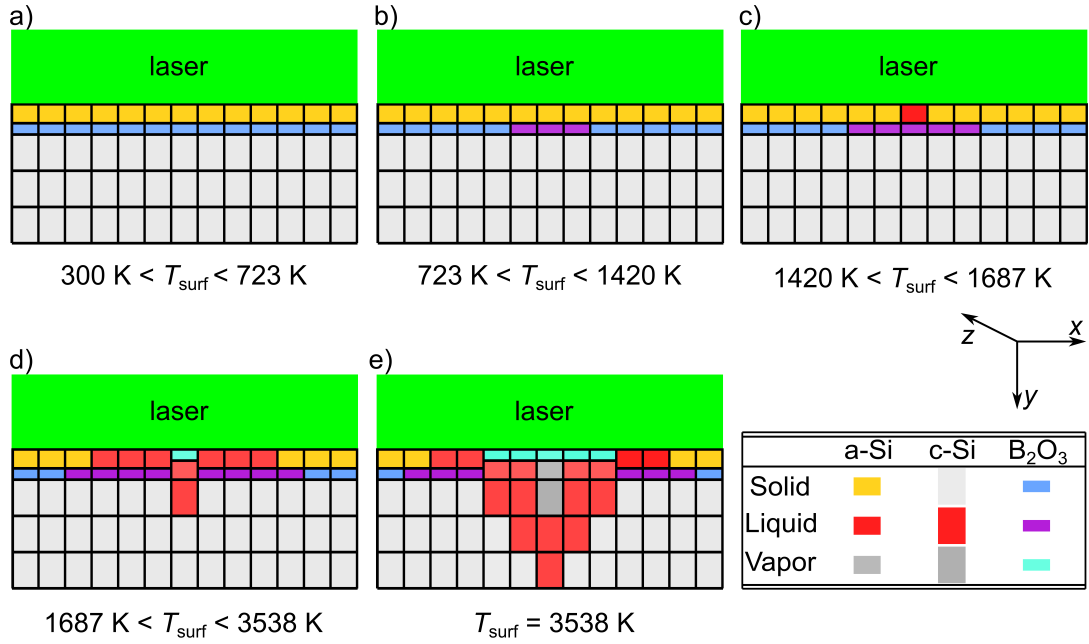


Figure 4.16: The different phases occurring during the doping process are schematically represented at the region with the finest discretization in fig. 4.2. a) At the beginning of irradiation, the wafer surface temperature $T_{surf} = 300$ K. Silicon absorbs the green laser and the surface temperature T_{surf} increases. b) At $T_{surf} \geq 723$ K, boron oxide B_2O_3 melts but no diffusion occurs as silicon (a-Si and c-Si) is still solid. c) When T_{surf} exceeds $T_{melt,a-Si} = 1420$ K [87], the 12 nm thick amorphous silicon a – Si melts and the diffusion process begins (melt/melt). d) As the surface temperature T_{surf} reaches the crystalline silicon melting temperature $T_{melt,Si} = 1687$ [76], crystalline silicon c – Si melts and boron atoms diffuse from the boron-rich, previously-melted, thin 'a-Si' silicon layer. Fusion of the crystalline silicon and evaporation of the boron oxide layer occur simultaneously as $T_{evap,B_2O_3} = 1773$ K [85]. The evaporated boron oxide volume element is reallocated to be on the top of all layers, which is analogous to the real situation (gas/melt/melt). e) Finally, silicon evaporates when $T_{surf} \geq 3538$ K [79]. Boron then diffuses through the evaporated silicon to reach the melt surface (gas/gas/melt).

Figure 4.16 schematically shows the different phases through which the discretized volume passes during the laser doping process. a) At the beginning of processing, the green laser beam irradiates the silicon surface and the precursor layer system (12 nm a-Si over 1 nm B_2O_3). The surface at room temperature is $T_{surf} = 300$ K.

The absorbed radiation heats up the surface, increasing its temperature T_{surf} . b) At $T_{\text{surf}} = 723$ K, boron oxide elements in the middle of the beam melts while silicon is still in a solid state, therefore, no diffusion happens. c) The amorphous silicon melts at $T_{\text{surf}} = T_{\text{melt,a-Si}} = 1420$ K [87]. As soon as the thin (12 nm thick) a-Si layer melts, boron atoms diffuse from the melted boron oxide. At this moment, the diffusion process begins as melt/melt. d) The beam continues to heat the surface until $T_{\text{surf}} = T_{\text{melt,Si}} = 1687$ K. At $T_{\text{surf}} = 1687$ K, crystalline silicon melts [76] and boron oxide evaporates (an illustration is presented in the next section). When the state of a unit volume changes from liquid to vapor, a reordering of the nodal mesh occurs to move the evaporated element to the top. The diffusion process then takes place as follows: gas/melt/melt e) For enough high pulse energy densities $H \geq 4$ J/cm², the melted silicon evaporates and the diffusion process continues as gas/gas/melt.

4.2.2.2 Model Validation

The current section discusses the procedures followed to validate the mass transfer model/diffusion model.

4.2.2.2.1 Experiment

Figure 4.17 shows a scheme of the experiment used for the validation of the diffusion model. The experiment consists of three steps: precursor layer deposition, dopant diffusion inside of the pure silicon surface and doping profile measurement of the doped layer.

Figure 4.17a shows the first step, which deposits a two-layer precursor using the RF-sputtering technique. The precursor layer system that covers the cleaned silicon wafer surface consists of a 12 nm thick amorphous silicon layer on top of a 1 nm thick boron oxide layer.

Figure 4.17b demonstrates the laser doping step of the silicon surface with the precursor layer covering it. The green pulsed laser (wavelength $\lambda = 532$ nm) irradiates and melts the surface allowing diffusion of the dopant materials in the melted surface. After laser doping, a 30 s dip in a 5% HF solution removes materials that remain after the doping step.

Figure 4.17c displays the secondary ion mass spectroscopy *SIMS* measurement of the doped layer in the silicon surface. The measurement produces a concentration

C_B - depth d profile (the doping profile) of the doped layer. The measured doping profiles are then compared to the calculated profiles using the proposed mass transfer model.

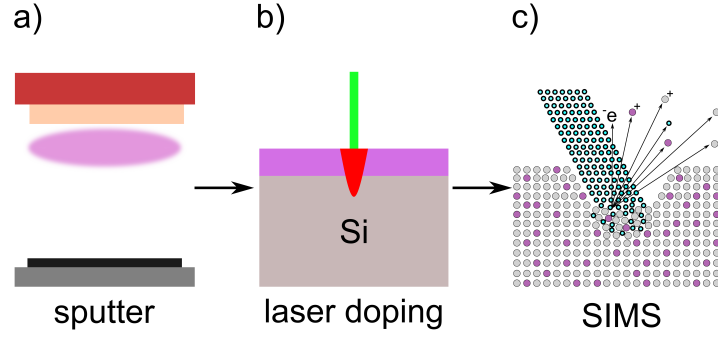


Figure 4.17: The experiment used to validate the diffusion model consists of three steps. a) RF-Sputtering of the precursor layer system which consists of a 12 nm thick a -Si covering 1 nm thick B_2O_3 . b) Directly after the deposition of the precursor layer, a green pulsed laser beam irradiates the surface, allowing the boron atoms existing in the precursor layer to diffuse into the silicon surface. c) Finally, the secondary ion mass spectroscopy SIMS device mentioned in sec. A.2.4 measures the doping profile (concentration C_B - depth d profile) of the doped surface layer. The obtained doping profiles are then compared to the calculated profiles by the proposed diffusion model.

4.2.2.2.2 Validation

Figure 4.18 shows the measured and the calculated doping profiles w/ and w/o considering the evaporation processes occurring during the doping process. Since the two used pulse energy density $H_1 = 1.77 \text{ J/cm}^2$ and $H_2 = 2.31 \text{ J/cm}^2$ are less than the threshold for silicon evaporation ($H_{\text{th, evap, Si}} = 2.8 \text{ J/cm}^2$), no evaporation of silicon takes place during the doping process. However, both pulse energy densities H_1 and H_2 are high enough to evaporate the boron source layer which evaporates immediately after, or even with, the melting of the crystalline silicon surface as shown in sec. 4.2.2.3. The evaporation of the melted boron oxide layer increases its volume which locally decreases the boron concentration C_B . Consequently, the number of boron atoms diffusing inside the surface decreases. Therefore, ignoring the evaporation process of the boron source layer overestimates the number of boron

atoms diffusing inside the melted silicon surface. For that reason, the doping profiles calculated w/o the evaporation process overestimates the doping profile, whereas the profiles w/ evaporation fits the measured profiles well.

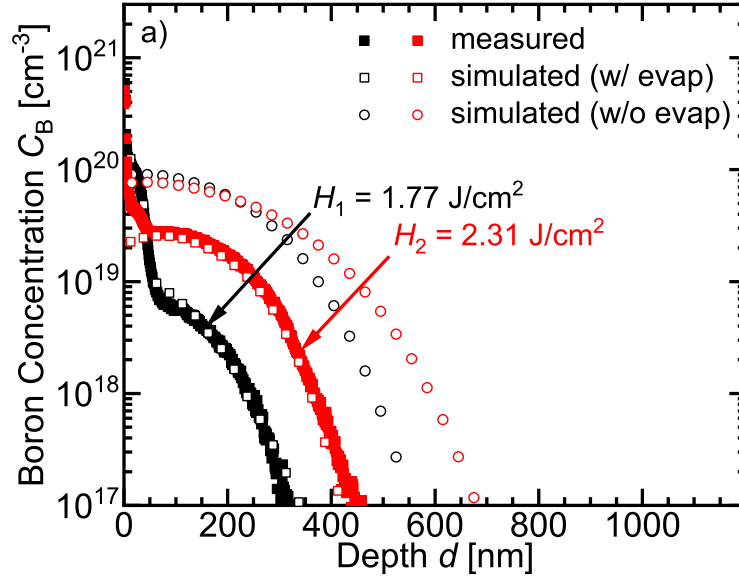


Figure 4.18: The comparison between the simulated doping profiles w/ and w/o considering evaporation and the measured doping profiles for a laser doped silicon surface with pulse energy density $H_1 = 1.77 \text{ J/cm}^2$ and $H_2 = 2.31 \text{ J/cm}^2$. Since H_1 and H_2 are less than $H_{th, \text{evap}, Si}$, silicon does not evaporate. Boron oxide evaporates simultaneously with the melting of crystalline silicon, as calculated in details in sec. 4.2.2.3. The simulated doping profile using the model w/ evaporation fits the measured doping profiles well, whereas the profiles calculated using the model w/o evaporation overestimates the doping profiles. Evaporation of the boron oxide layer (the boron source) increases its volume, which locally decreases the boron concentration in the source layer. Ignoring dilution of the superficial boron source as a result of expansion after evaporation overestimates the boron concentration at the surface. The high surface concentration C_B increases the concentration gradient along the depth, which enhances diffusion in depth, and thus, creates deeper profiles.

Figure 4.19 shows the comparison between the measured and the simulated doping profiles for the doped layer using the three pulse energy densities $H_3 = 3.45 \text{ J/cm}^2$, $H_4 = 3.91 \text{ J/cm}^2$ and $H_5 = 4.25 \text{ J/cm}^2$. In the three cases, evaporation of not

only the boron oxide layer but also parts of the melted silicon surface occurs, as H_3 , H_4 and H_5 are higher than $H_{th, evap, Si} = 2.8 \text{ J/cm}^2$. In addition to evaporation of the boron source with the accompanying local boron concentration C_B dilution, parts of the highly doped melted silicon surface evaporate. In other words, the evaporated highly doped silicon surface decreases the total number of boron atoms in the doped layer. Therefore, the model w/o evaporation overestimates the doping profile, whereas the model w/ evaporation predicts the doping profiles accurately.

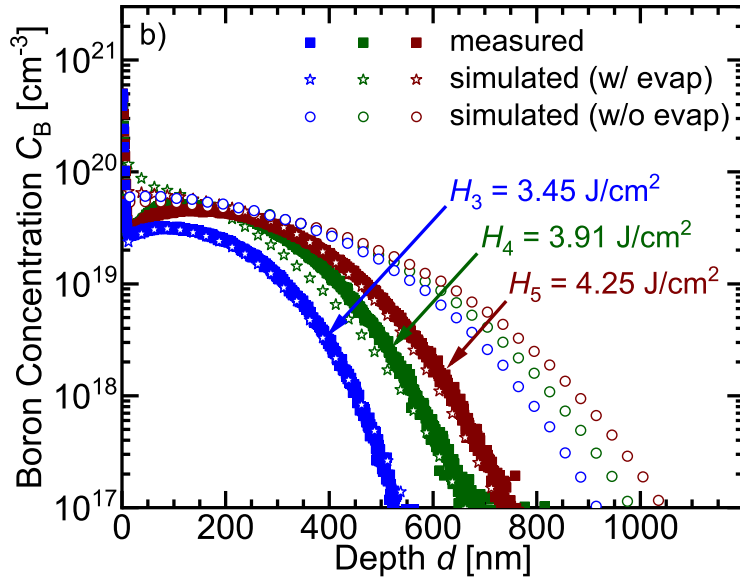


Figure 4.19: The doping profiles of the silicon surface doped with pulse energy density $H_3 = 3.45 \text{ J/cm}^2$, $H_4 = 3.91 \text{ J/cm}^2$ and $H_5 = 4.25 \text{ J/cm}^2$. The threshold pulse energy density $H_{th, evap, Si}$ of silicon evaporation is $H_{th, evap, Si} = 2.8 \text{ J/cm}^2$ which is lower than H_3 , H_4 and H_5 . Therefore, not only the boron source layer but also parts of the melted silicon surface evaporate during the doping process. Due to evaporation, the loss of boron atoms of the relatively high-doped silicon surface, as well as the dilution of the boron source, decrease the content of boron in the doped layer. For this reason, the model w/o evaporation overestimates the depth of the doping profile as a result of the overestimated melt depth d_{melt} as shown in fig. 4.15 and the overestimated number of diffused boron atoms in the melted surface. The model w/ evaporation predicts the doping profile well.

4.2.2.3 Assumption in the Model

- The model neglects the heat transfer between the hot/melted surface and the air above it. The thermal conductivity k_{air} of air ranges from 0.01 - 0.08 W/(m K) [88] and increases to be 0.12 W/(m K) at temperature T of 2000 K [89]. The thermal conductivity k_{Si} of solid silicon at temperature T of 300 K equals 152 W/(m K) and that of melted silicon at temperature T of 2000 K equals 62 W/(m K) [90, 91]. Consequently, heat loss from the hot surface into the surrounding air is neglected by the current model.
- The absorption of the incident laser in the 12 nm thick amorphous silicon cap *a-Si* layer is negligibly small, therefore the model does not consider it. The absorption coefficient $\alpha_{\text{abs,a-Si}}$ of the amorphous silicon layer for wavelength $\lambda = 532$ nm at room temperature $T = 300$ K is $\alpha_{\text{abs,a-Si}} = 21.88 \times 10^3 \text{ cm}^{-1}$ which corresponds to absorption length $l_{\text{abs,a-Si}} = 469$ nm [92]. Thus, the absorption in the 12 nm thick cap layer is less than 2.5% of the incident non-reflected green laser. As a result, the temperature T of the two-layer precursor system equals the temperature T_{surf} of the surface of the silicon wafer.
- For consideration of over heating and undercooling situations, the used melting temperature in the simulation for melting is $T_{\text{melt,Si}} + 20$ and for re-solidification is $T_{\text{melt,Si}} - 20$. The difference of 20 corresponds to the increase (when melting occurs) and to the drop (when re-solidification occurs) of the melting temperature away from the slow melting and slow re-solidification temperature $T_{\text{melt,Si}}$. For the pulse duration τ_p range and pulse energy density range H used in this work, during and after irradiation, the liquid/solid interface velocity v_{int} ranges between 5 and 16 m/s during melting and re-solidification. For that reason, it is reasonable that the increment and drop in the melting/re-solidification temperature is about 20 degrees [62, 93].
- Due to the relatively small thermal penetration depth δ_{th} in comparison to the thickness of the silicon wafer, the model assumes the temperature T of the deep bulk material to be equal to room temperature $T = T_0$ during the entire irradiation duration. The thermal penetration depth δ_{th} is a characteristic property that describes the thermal propagation depth and is expressed as

$$\delta_{\text{th,Si}} = 2\sqrt{\alpha_{\text{th,Si}} \tau_{\text{irr}}}, \quad (4.29)$$

where α_{th} is the thermal diffusivity of silicon and τ_{irr} is the irradiation duration from the beginning of irradiation and extending until the liquid silicon resolidifies. Assuming that the surface temperature T_{surf} reached the evaporation temperature $T_{\text{surf}} = T_{\text{Si,evap}} = 3538$ K and the whole irradiation duration $\tau_{\text{irr}} = 300$ ns [62], the thermal penetration depth equals

$$\delta_{\text{th}} = 2 \sqrt{\frac{k_{\text{Si}}(T = 3538\text{K}) \tau_{\text{irr}}}{\rho_{\text{Si}}(T = 3538\text{K}) c_{\text{p,Si}}(T = 3538\text{K})}} = 2 \sqrt{\frac{62 \left[\frac{\text{J}}{\text{m s K}} \right] * 300 \times 10^{-9} [\text{s}]}{2311 \left[\frac{\text{Kg}}{\text{m}^3} \right] 1021.8 \left[\frac{\text{J}}{\text{Kg K}} \right]}} = 5.6 \mu\text{m} \quad (4.30)$$

which is much thinner than the wafer thickness $d_{\text{wafer}} = 160 \mu\text{m}$. For that reason, the model assumes the temperature T of the bulk stays at $T = 300$ K during the whole irradiation process. Additionally, the current model assumes that the temperature T of the far sides of the substrate stay at $T = 300$ K. The depth of the volume studied in the current work is $6.5 \mu\text{m}$ and the lateral width is $40 \mu\text{m}$, and the beam irradiates at the middle of the width.

- The assumption that the far lateral sides and the deep bulk of substrate has temperature T of 300 K is simulated by adding two virtual columns on the lateral extremes and a virtual row beneath the simulated volume. The temperature T of the added virtual columns and row at the bottom is fixed at $T = 300$ K.
- The model assumes that the 1 nm thick boron oxide layer (the dopant source) evaporates as soon as the first crystalline silicon row (25 nm thick) melts. Crystalline silicon melts at $T = 1687$ K with a latent heat of fusion $H_{\text{melt,Si}} = 1802$ J/g [76], whereas boron oxide evaporates at $T = T_{\text{evap,B}_2\text{O}_3} = 1773$ K with a latent heat of fusion $H_{\text{evap,B}_2\text{O}_3} = 4308$ J/g[85]. The density of silicon and boron oxide at $T = T_{\text{melt,Si}} = 1687$ K is $\rho_{\text{s-Si}} = 2.293$ g/cm³ [83] and $\rho_{\text{l-B}_2\text{O}_3} = 1.498$ g/cm³ [78, 94]. The heat capacity c_{p} of solid silicon and liquid boron oxide at $T = 1687$ K are $c_{\text{p,c-Si}} = 3.307$ J/(g K) and $c_{\text{p,l-B}_2\text{O}_3} = 0.4472$ J/(g K) [95]. The required energy $E_{\text{melt,Si}}$ to melt the first row of crystalline silicon

($\Delta y = 25$ nm thick) is

$$\begin{aligned} E_{\text{melt,Si}} &= \rho_{\text{s-Si}} d_{\text{Si}} H_{\text{melt,Si}} = 2.293 * 25 \times 10^{-7} * 1802 \\ &= 10300 \mu\text{J}/\text{cm}^2, \end{aligned} \quad (4.31)$$

whereas the energy $E_{\text{evap,B}_2\text{O}_3}$ needed by a 1 nm thick boron oxide layer to heat up from $T = T_{\text{melt,Si}} = 1687$ K [76] up to $T = T_{\text{evap,B}_2\text{O}_3} = 1773$ K [85] is

$$\begin{aligned} E_{\text{evap,B}_2\text{O}_3} &= \rho_{\text{l-B}_2\text{O}_3, \text{l}} d_{\text{B}_2\text{O}_3} \left[c_{\text{pB}_2\text{O}_3} (T_{\text{evap,B}_2\text{O}_3} - T_{\text{melt,Si}}) + H_{\text{evap, B}_2\text{O}_3} \right] = \\ &1.498 * 1 \times 10^{-7} [0.4472 * (1773 - 1687) + 4308] = 651 \mu\text{J}/\text{cm}^2. \end{aligned} \quad (4.32)$$

Thus, the required energy $E_{\text{evap,B}_2\text{O}_3}$ to heat a 1 nm thick boron oxide layer from $T = T_{\text{melt,Si}}$ to $T_{\text{evap,B}_2\text{O}_3}$ and evaporate it equals the energy $E_{\text{melt,Si}}$ needed to melt a 1.6 nm thick crystalline silicon layer. Thus the assumption made in the model is valid.

- The model addresses the increased energy coupling as a reduction in the melted surface reflectance $R_{\text{Si,l}}$ over the evaporated width during the evaporation phase only. The amount of evaporated material is mainly determined by the pulse energy density H , pulse duration τ_p and the intensity-distribution profile of the irradiating laser beam. The laser pulse has a Gaussian intensity distribution in the x-direction, which means more photons are absorbed in the middle of the irradiated area than in the lateral directions. The beam also has a tophat profile in the long axis direction (the z-direction). The profile of the molten surface is almost an inverse shape of the intensity-distribution profile of the laser beam. Consequently, more heat, and thus higher temperature, is acquired in the middle in comparison to the relatively colder melt edges. When temperature T_{surf} at the center of the melted area reaches the evaporation temperature $T_{\text{evap,Si}} = 3538$ K of silicon, evaporation starts, whereas the edges are still molten. Resultantly, the melted surface under the evaporated volume acquires a capillary-like shape. Higher pulse energy density H laser beams increase the depth d_{evap} of the capillary. Accordingly, increasing the pulse energy density H of the laser beam increases the aspect ratio (evaporated depth d_{evap} /evaporated width W_{evap}) of the melted silicon surface. The increased aspect ratio enhances the laser entrapment by multiple reflection of

radiation, and thus, improves the coupling efficiency η_{coupling} [41, 96]. Additionally, due to the anomalous behavior of the silicon upon melting (increasing of silicon density at the melting temperature T_{meltSi}), the silicon surface's level lowers, which further increases the aspect ratio [81, 97, 98]. Consequently, the coupling efficiency η_{coupling} increases.

The model considered the increased coupling efficiency η_{coupling} as a local reduction of the reflection $R_{\text{Si,l}}$ of the melted silicon surface along the evaporation width W_{evap} . The determination of the equivalent reduced surface reflection $R_{\text{Si,l}}$ occurred based on the heat transfer model. The correct equivalent surface reflectance $R_{\text{Si,l}}$ value is that that gives the same evaporated depth d_{evap} as measured from fig. 4.13f), g), h) and i).

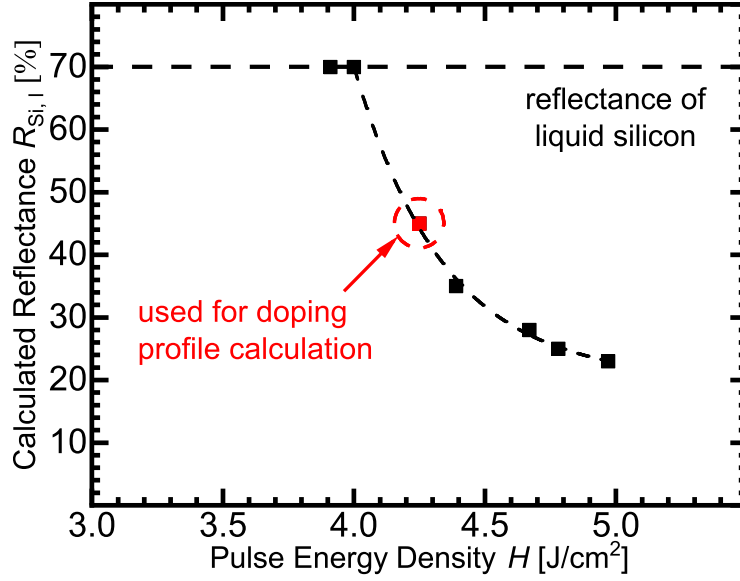


Figure 4.20: The absorption efficiency of laser radiation on the evaporated tube-like capillary-shaped surface increases due to the multiple reflection. The increased absorption is represented in the model as a reduced equivalent surface reflectance $R_{Si,l}$. The determination of the reduced equivalent surface reflectance $R_{Si,l}$ took place using the heat transfer model. The correct equivalent surface reflectance $R_{Si,l}$ value is that, that accurately predicts the evaporated depth d_{evap} measured in fig. 4.13. Since there is no available microscopic profile at the pulse energy density $H = 4.25$ J/cm², the equivalent surface reflectance $R_{Si,l}$ is extrapolated from the fitted curve. The equivalent surface reflectance $R_{Si,l}$ at pulse energy density $H = 4.25$ J/cm² is 45% instead of 70% [74].

Figure 4.20 represents the equivalent surface reflectance $R_{Si,l}$ of the melted silicon that correctly predicts the evaporation depth d_{evap} measured from fig. 4.13. Increasing the used pulse energy density H increases the portion of the evaporated silicon surface during irradiation, which increases the depth d_{evap} of the evaporated surface. The increased evaporated depth d_{evap} improves light absorption through multiple reflections. Improved absorption with increasing pulse energy density H decreases the equivalent surface reflectance $R_{Si,l}$. For a pulse energy density $H = 4.25$ J/cm², the equivalent surface reflectance $R_{Si,l}$ is extrapolated from the fitted points and is $R_{Si,l} = 45\%$. The extrapolated equivalent surface reflectance $R_{Si,l}$ is used for simulation of the doping profile

at pulse energy density $H = 4.25 \text{ J/cm}^2$.

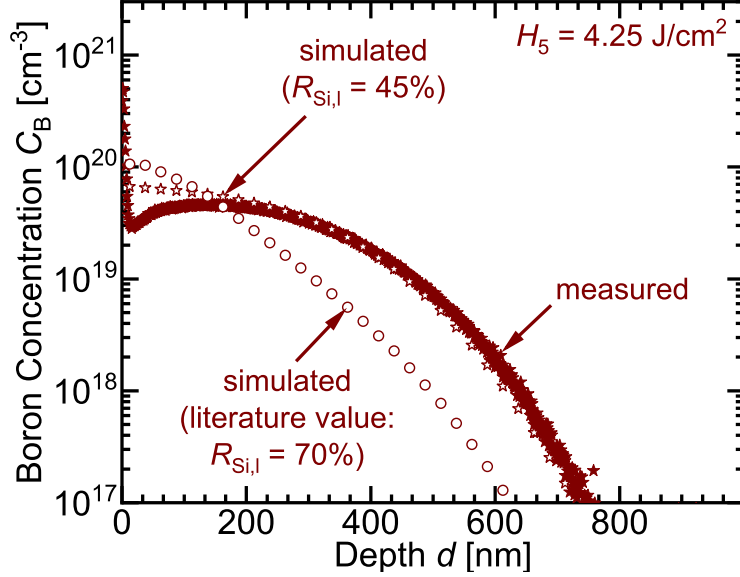


Figure 4.21: Simulation using the reflection value $R_{Si,l} = 45\%$ over the evaporated width W_{evap} during the evaporation phase accurately predicted the doping profile. The model underestimates the doping profile when the literature value ($R_{Si,l} = 70\%$ [74]) is used without reduction. The higher literature value of surface reflectance $R_{Si,l}$ decreases the amount of coupled optical energy in the silicon surface which underestimates the melt depth d_{melt} . Therefore, the doping profile resulting from using the literature value $R_{Si,l} = 70\%$ [74] is shallower.

Figure 4.21 shows the comparison between the simulated doping profile using the literature value of surface reflectance $R_{Si,l} = 70\%$ [74] of melted silicon and the reduced reflectance $R_{Si,l}$ as a result of enhanced energy coupling. The literature value of surface reflectance $R_{Si,l} = 70\%$ [74] couples less laser energy inside the melted layer. Therefore, the melt depth d_{melt} decreases and the profile depth decreases. In reality, at such a high pulse energy density $H_5 = 4.25 \text{ J/cm}^2$, parts of the silicon surface evaporate from the surface center, leaving behind a tube-like capillary. The capillary tube enhances energy coupling by multiple reflection of radiation on its walls. Consequently, the equivalent surface reflectance $R_{Si,l}$ value over the evaporated width during the evaporation phase must be lower than the value in the literature to allow more energy

coupling. The value of surface reflectance $R_{\text{Si,l}}$, which is extracted from fig. 4.20 ($R_{\text{Si,l}} = 45\%$), gives the best fit for the measured doping profile.

- After the melted region cools and resolidifies, a part of the evaporated materials (only boron oxide or boron oxide and silicon) recondenses on the cooled surface. The recondensed materials provide an additional doping source during the subsequent laser pulses. The correct portion of recondensed materials is determined based on which recondensation value gives the best fit for the measured doping profile. For pulse energy density $H \leq 2.8 \text{ J/cm}^2$, the silicon does not evaporate, and thus, the recondensed materials are only boron oxide. For higher laser pulse energy densities $H > 2.8 \text{ J/cm}^2$, doped silicon also evaporates and recondenses as a doped amorphous silicon layer (p-aSi).

Figure 4.22 displays the recondensed portion of the evaporated materials after the end of the laser pulse and cooling of the melted region. The simulation used three values of the recondensed portion, 40%, 50% and 60%. The best fit for the measured data (profile of layer doped at pulse energy density $H_5 = 4.25 \text{ J/cm}^2$) resulted from using the 50% value. The 40% recondensation portion underestimates the profile as it provides less recycled boron atoms as a doping source. On the contrary, the 60% provides more recycled boron atoms as a doping source, and therefore, overestimates the doping profile. In the work of Koehler et al. [62], they obtained the best fit for the measured doping profiles when the value of the recondensation portion equals 50%.

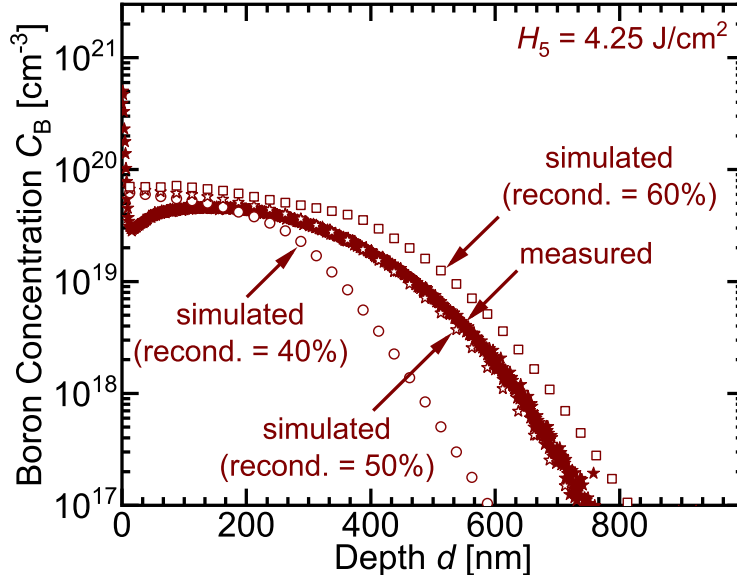


Figure 4.22: To find out the portion of vaporized materials that recondenses after the melt cools down, the model simulated using different values. The recondensation value that gave the best fit to the measured profile at $H_5 = 4.25 \text{ J/cm}^2$ is the 50%. Simulation using the other two values (40% and 60%) either underestimates or overestimates the doping profile, respectively.

- The best fits showed that the segregation coefficient of boron in liquid silicon is unity. A similar value of the segregation coefficient of boron in the liquid silicon was used in the work of Lill et al. [64] and the work of G. G. Bentini et al. [57] to obtain the best fitting of the experimental data.
- The best fits of the measured doping profiles occurred when two values of the diffusion coefficient D_c of boron in liquid silicon were used. The diffusion coefficient D_c depends on the activation energy E_a and the pre-exponential diffusion coefficient D_0 through

$$D_c(T) = D_0 \exp\left(\frac{-E_a}{k_B T}\right). \quad (4.33)$$

The literature values of both the pre-exponential diffusion coefficient $D_0 = 2.7 \times 10^{-4} \text{ cm}^2/\text{s}$ and the activation energy $E_a = 11.5 \text{ kJ/mol}$ are mentioned in the work of Tang et al. [99]. However, the best prediction of the doping profile occurs when two values of the pre-exponential diffusion coefficient D_0

values are used for two different temperature ranges. The literature value of the diffusion coefficient $D_{0,1} = 2.7 \times 10^{-4} \text{ cm}^2/\text{s}$ [99, 100] dominates as long as the highest temperature in the melt does not exceed 2100 K. The value reported in the work of Lill et al. [64], the pre-exponential coefficient $D_{0,2} = 8 \times 10^{-4} \text{ cm}^2/\text{s}$ dominates as long as the maximum temperature in the melt is higher than 2100 K. That means for the temperature range $T_{\text{melt,Si}} \leq T_{\text{surf}} < 2100 \text{ K}$, the literature value of the pre-exponential factor $D_{0,1} = 2.7 \times 10^{-4} \text{ cm}^2/\text{s}$ dominates. For the temperature range $2100 \leq T_{\text{surf}} \leq T_{\text{evap,Si}}$, the pre-exponential factor $D_{0,1} = 8 \times 10^{-4} \text{ cm}^2/\text{s}$.

A similar behavior is observed by M. Bertie et al. [54] for the case of oxygen diffusion in liquid silicon. They found that the diffusion coefficient of oxygen is in the order of $10^{-4} \text{ cm}^2/\text{sec}$.

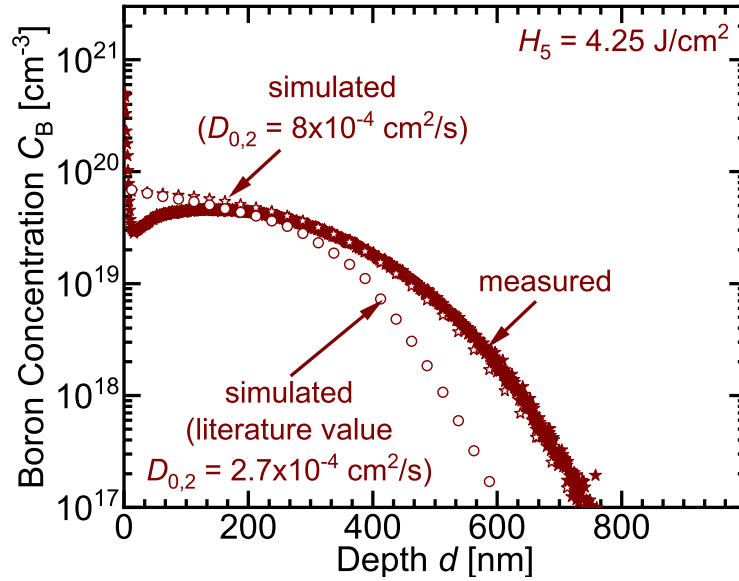


Figure 4.23: The best fit to the measured concentration profile results when a higher value of the pre-exponential factor D_0 is used. Simulation using only the literature value of pre-exponential factor $D_0 = 2.7 \times 10^{-4} \text{ cm}^2/\text{s}$ [99, 100] underestimates the doping profile due to ignoring the circulation-assisted diffusion happening when temperature T_{surf} is high enough. Using the value $D_0 = 8 \times 10^{-4} \text{ cm}^2/\text{s}$, reported in the work of Lill et al. [64], when the temperature $T_{\text{surf}} \geq 2100 \text{ K}$ and the value $D_0 = 2.7 \times 10^{-4} \text{ cm}^2/\text{s}$ when the temperature $T_{\text{surf}} < 2100 \text{ K}$, accurately predicts the doping profile.

Figure 4.23 compares the simulated doping profiles when a higher pre-exponential factor $D_{0,2}$ value is used with the measured doping profile. Using the value $D_{0,2} = 8 \times 10^{-4} \text{ cm}^2/\text{s}$ when the temperature $T_{\text{surf}} \geq 2100 \text{ K}$ yields the best fit to the measured profile. Using only the literature value $D_{0,1} = 2.7 \times 10^{-4} \text{ cm}^2/\text{s}$ underestimates the doping profile. The reason for the underestimation is due to ignoring the circulation-assisted diffusion.

The reason for the higher pre-exponential coefficient $D_{0,2}$ is the circulating melt. As a result of the Gaussian intensity distribution of the irradiating laser, the center of the melt surface is much hotter than the relatively colder edges. In this context, cold melt means at melting temperature $T_{\text{melt,Si}} = 1687 \text{ K}$ [76]. The surface tension σ of the melted silicon is a function of temperature T which means that the temperature gradient across the melted surface induces a surface tension gradient, causing the melt to circulate. The circulation of the melt due to the surface tension induced temperature gradient is called *thermocapillary effect* or *Marangoni convection*. The melt motion enhances the diffusion process, hence, the effective diffusion coefficient D_c must be higher than the equilibrium literature value. Therefore, the pre-exponential factor D_0 must be high when the melt circulates.

The circulation velocity v_c depends on the surface tension gradient-induced temperature gradient $\partial\sigma/\partial T$, the temperature difference ($T_{\text{surf}} - T_{\text{melt,Si}}$) between the hot center and the cold melt edge, the dynamic viscosity η , the length Δr_{melt} over which the temperature gradient extends and the melt depth d_{melt} through [101]

$$v_c = \frac{\partial\sigma}{\partial T} \frac{T_{\text{surf}} - T_{\text{melt,Si}}}{\Delta r_{\text{melt}}} \frac{d_{\text{melt}}}{\eta}. \quad (4.34)$$

Figure 4.24 displays a moment during irradiation of the silicon surface. The temperature distribution in the melted volume ranges from the maximum reachable temperature (the evaporation temperature $T_{\text{evap,Si}} = 3538 \text{ K}$ [79]) down to the coldest temperature (the melting temperature $T_{\text{melt,Si}} = 1687 \text{ K}$ [76]). The red color represents the highest temperature T_{surf} and the blue represents the coldest temperature, the melting temperature $T_{\text{melt,Si}}$. The Gaussian intensity distribution of the irradiating laser beam over the width (x-direction)

of the melt induces a temperature gradient across the melt width. The temperature gradient induces a surface tension gradient, which circulates the melt. The parameters in eq. 4.34 (the melt depth d_{melt} and the width Δr_{melt} over which the temperature gradient extends) are shown in the figure. The surface tension gradient induced temperature gradient $\partial\sigma/\partial T = 86 \times 10^{-6} \text{ N}/(\text{m K})$ [102] and the dynamic viscosity $\eta = 750 \text{ } \mu\text{N s}/\text{m}^2$ [103].

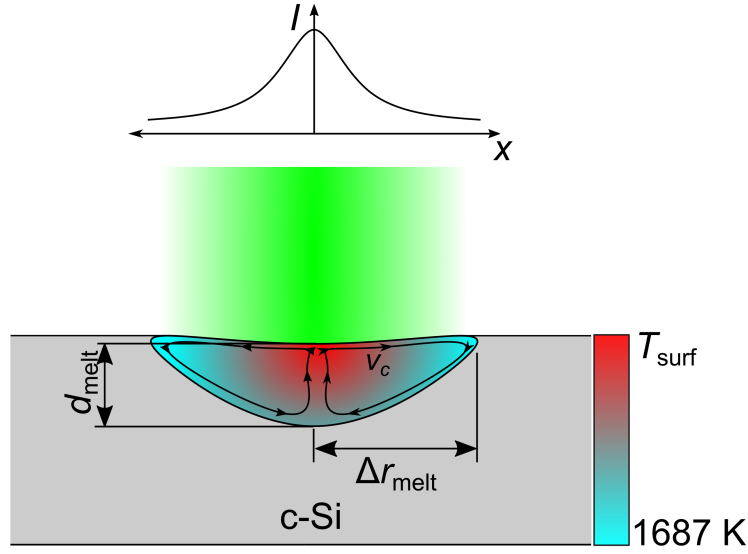


Figure 4.24: The scheme visualizes the melted volume during irradiation with the temperature distribution represented by colors. The red color represents the maximum temperature T_{surf} and the blue represents the coldest temperature, the melting temperature $T_{\text{melt,Si}} = 1687 \text{ K}$ [76] of silicon. The superficial temperature gradient results from the Gaussian distribution of the laser intensity over the melt width (in the x -direction). A surface tension gradient results from the temperature gradient leading to circulation of the melt. The phenomena is called Marangoni convection or thermocapillary effect.

Figure 4.25 shows the approximated geometrical shape for the melted volume during irradiation. Figure 4.25a shows when the used pulse energy density $H \leq 2.8 \text{ J}/\text{cm}^2$. In this scenario, no evaporation occurs. Therefore the length Δr_{melt} , over which the temperature gradient extends, is the half of the melt width W_{melt} . Figure 4.25b demonstrates when the pulse energy density $H > 2.8 \text{ J}/\text{cm}^2$, where portions of the melted silicon surface evaporate. In this case,

the melt length Δr_{melt} increases due to the increased surface circumference that results from evaporation. Furthermore, the melt depth d_{melt} is the remaining depth after the evaporation depth d_{evap} is deducted from the complete melt depth d_{melt} .

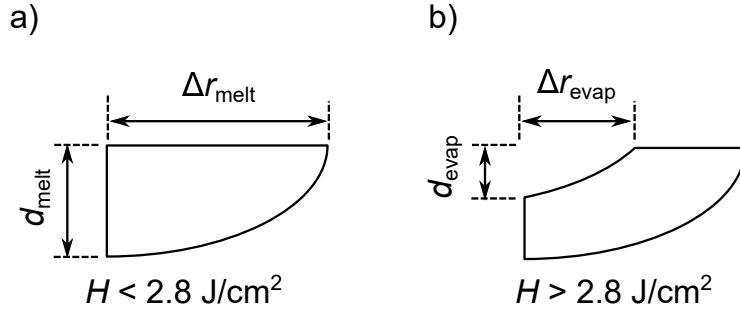


Figure 4.25: The scheme represents half of the molten pool in both irradiation cases, for pulse energy density a) $H < H_{\text{th, evap, Si}}$ and b) $H > H_{\text{th, evap, Si}}$. The melt width Δr_{melt} , over which the temperature gradient extends, increases in the case of evaporation. The increased part is due to the ellipse-shaped surface resulting from evaporation. a) At $H \leq 2.8 \text{ J/cm}^2$, half of the melt pool is a quarter of an ellipse. b) At $H > 2.8 \text{ J/cm}^2$, half of the melt pool is approximated by two concentric ellipses in order to consider the evaporated portion.

The following calculation clarifies for the higher pre-exponential coefficient $D_{0,2} = 8 \times 10^{-4} \text{ cm}^2/\text{s}$ (literature $D_0 = 2.7 \times 10^{-4} \text{ cm}^2/\text{s}$ [99, 100]). The temperature-time curve (as fig. 4.11) determines the maximum surface temperature T_{surf} . Additionally, the curve allows the determination of the duration of heating, evaporation and cooling phases. The heating phase duration t_{heating} is the period over which the temperature T_{surf} heats from $T_{\text{surf}} = 2100 \text{ K}$ up to the maximum temperature T_{max} . The cooling phase t_{cooling} is the period over which the temperature T_{surf} cools from $T_{\text{surf}} = T_{\text{max}}$ down to the temperature $T_{\text{surf}} = 2100 \text{ K}$. The evaporation phase t_{evap} is the period over which the surface temperature T_{surf} equals the evaporation temperature $T_{\text{evap, Si}}$. The duration t_{heating} , t_{cooling} and t_{evap} are also obtainable from the validated model.

For a pulse energy $H_1 = 1.77 \text{ J/cm}^2$, the heating, cooling and evaporation periods equal $t_{\text{heating}} = 20 \text{ ns}$, $t_{\text{cooling}} = 36 \text{ ns}$ and no evaporation occurs. The maximum temperature $T_{\text{max}} = 2660 \text{ K}$. The average melt width ($w_{\text{melt}}/2$) over

which the temperature gradient $\Delta T = 2660 - 1687$ extends is $3 \mu\text{m}$. The average melt depth $d_{\text{melt, heating}}$ during the heating phase is $d_{\text{melt, heating}} = 340$ nm, while during the cooling phase is $d_{\text{melt, cooling}} = 600$ nm. Substituting in eq. 4.34, the circulation velocity v_c during the heating phase $v_{c, \text{heating}} = 12.6$ m/s while during the cooling phase is $v_{c, \text{heating}} = 22.3$ m/s. From the circumference formula for the assumed melt pool geometry depicted in fig. 4.25, the complete circumference is obtained. The circumference equation of the quarter ellipse is $(\Delta r_{\text{melt}} + d_{\text{melt}})(1 + \pi/4)$. For $H = 1.77 \text{ J/cm}^2$, the total circumference $L_{\text{melt, total}} = 6.7 \mu\text{m}$. Using the calculated circulation velocities together with the heating and cooling phase duration, we get a circulated distance $L_{\text{circ}} = 1.06 \mu\text{m}$, which means about 15.8% of the total half pool circumference.

For a pulse energy density $H_5 = 4.25 \text{ J/cm}^2$, the heating, evaporation and cooling periods equal $t_{\text{heating}} = 12$ ns, $t_{\text{evap}} = 46$ ns and $t_{\text{cooling}} = 65$ ns. The half of the melt width $w_{\text{melt}}/2$ during the heating, evaporation and cooling phases are $2.5 \mu\text{m}$, $5.25 \mu\text{m}$ and $5.25 \mu\text{m}$, respectively. The melt depth during each phase is $d_{\text{melt, heating}} = 250$ nm, $d_{\text{melt, evap}} = 663$ nm and $d_{\text{melt, cooling}} = 413$ nm. The maximum temperature T_{max} reached is the evaporation temperature $T_{\text{evap, Si}} = 3538$ K [78, 79]. Substituting in eq. 4.34, the circulation velocity during each phase is $v_{c, \text{heating}} = 10.7$ m/s, $v_{c, \text{evap}} = 26.5$ m/s and $v_{c, \text{cooling}} = 8.3$ m/s. The total distance L_{circ} circulated by the melt during the irradiation period is $L_{\text{circ}} = 1.9 \mu\text{m}$ which is about 16.1% of the total circumference of the half pool ($L_{\text{melt, total}} = 11.8 \mu\text{m}$).

As shown in the calculations above, the total circulated portion of the half-melted pool is about 16% for both high and low pulse energy densities $H_1 = 1.77 \text{ J/cm}^2$ and $H_5 = 4.25 \text{ J/cm}^2$. That justifies the use of the same pre-exponential factor $D_{0, 2} = 8 \times 10^{-4} \text{ cm}^2/\text{s}$ for the entire pulse energy density range used.

Chapter 5

Sheet Conductance of Laser Doped Layers

This chapter focuses on the calculation of the sheet conductance G_{sh} of a doped layer using a pulsed laser beam. The substantial difference between a laser-doped layer and a furnace-doped layer is the cross-sectional geometry of the layer. A furnace-diffused layer has a uniform depth (y-direction) across the layer's width (x-direction), whereas a laser-doped layer does not. For that reason, eq. 2.2 accurately predicts the sheet conductance G_{sh} of a furnace-diffused layer. The regularity of a laser doped layer's depth d_{melt} significantly depends on the used pulse to pulse distance x_{irr} , which is defined as the distance between the centers of each two subsequent laser pulses. Since the pulses center coincides with the melted region center, a small x_{irr} melts the surface at positions close to each other, whereas a wide x_{irr} melts the surface at positions apart from each other. Therefore, a small x_{irr} decreases the depth variation along the layer's width, whereas a wide x_{irr} causes a significant depth d_{melt} irregularity along the width of the laser doped layer. Therefore, eq. 2.2 does not always predict the sheet conductance G_{sh} of a laser-doped layer accurately. The current chapter investigates the dependence of the sheet conductance G_{sh} of a laser-doped layer on doped layer geometry. The works shows the quadratic dependence of the resulting sheet conductance G_{sh} on the used pulse to pulse distance x_{irr} .

5.1 Introduction

The laser doping parameters control the resulting electrical properties of the doped sheet, i.e the sheet conductance G_{sh} . The scanning speed v_{scan} , with which the laser irradiates the surface, and the pulse repetition rate f , which is the number of pulses per second [Hz], control the distance x_{irr} between the successive laser pulses through

$$x_{\text{irr}} = \frac{v_{\text{scan}}}{f}. \quad (5.1)$$

The overlap O_x between the irradiated areas varies with the pulse to pulse distance x_{irr} according to

$$O_x = \frac{w_{\text{melt}} - x_{\text{irr}}}{w_{\text{melt}}} 100, \quad (5.2)$$

where w_{melt} is the melted/doped width by each laser pulse.

Figure 5.1a schematically represents a section of a silicon wafer during the laser doping process with a pulsed green laser beam. The wafer's surface is covered with a two-layer precursor system: a boron oxide (B_2O_3) layer covered by an amorphous silicon (a-Si) layer (orange color). The B_2O_3 layer is the boron (dopant) source. The laser irradiates and melts the surface allowing for the diffusion of boron atoms from the boron oxide layer into the melted silicon. The locally doped silicon (violet color) regions intersect according to the used distance x_{irr} . The width w_{melt} is the width of the melted region per laser pulse in the x-direction. Both the melt depth d_{melt} and width w_{melt} depend on the used pulse energy density H .

Figure 5.1b schematically represents a cross section of the doped layer in the silicon surface using different pulse to pulse distances x_{irr} . A single melted silicon region has approximately a parabolic shape. The parabolic shape emerges from the intensity distribution nature of the laser beam used. The pulse to pulse distance x_{irr} defines the overlap O_x between the doped regions, as indicated in eq. 5.2, and defines the intersection depth d_{ch} between the intersected doped regions. As the pulse to pulse distance x_{irr} increases, the pulse overlap O_x decreases and the intersection depth d_{ch} decreases until reaching zero for $x_{\text{irr}} \geq w_{\text{melt}}$. The decreasing pulse to pulse distance x_{irr} increases the intersection depth d_{ch} until reaching the melt depth $d_{\text{ch}} = d_{\text{melt}}$ at $x_{\text{irr}} \approx 0$. The next section mathematically tackles the dependence of intersection depth d_{ch} on pulse to pulse distance x_{irr} .

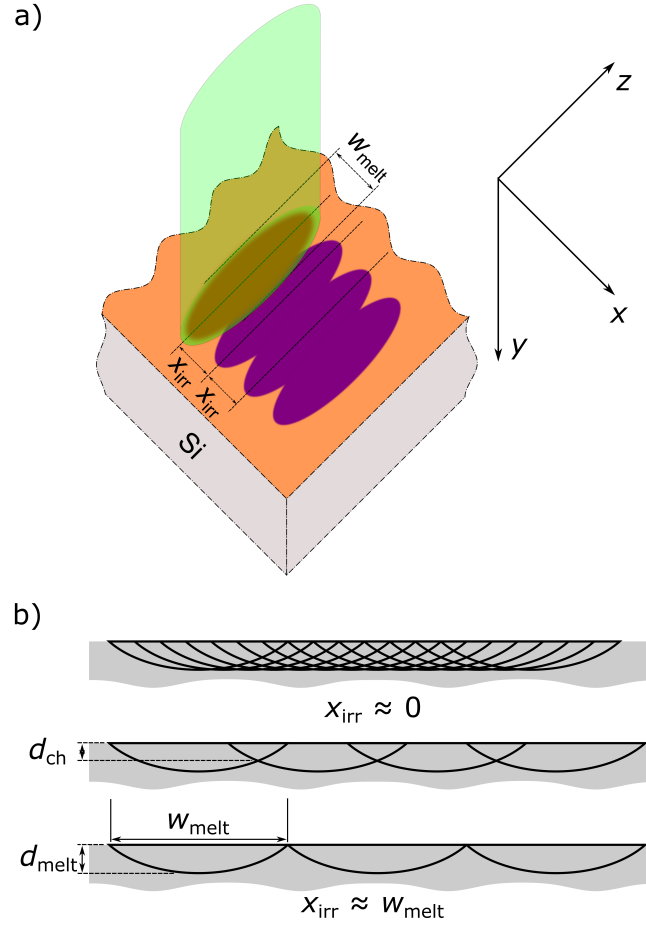


Figure 5.1: a) Cross section of a silicon wafer covered with a precursor layer (a 1 nm thick boron oxide layer covered by a 12 nm thick amorphous silicon layer (orange color)) during the laser doping process. A pulsed green laser beam with a Gaussian intensity distribution (over the x -axis) irradiates and melts the surface as shown by the red-colored region underneath the laser pulse. In the liquid state, boron atoms (dopant) diffuse in the melted silicon volume. The doped regions (violet color) are intersecting together depending on the distance x_{irr} between the centers of each two successive laser pulses. The width w_{melt} is the width of the melted silicon area. b) Each melted region has approximately parabolic borders in the irradiated silicon wafer. The distance between the centers of the parabolas corresponds to the used pulse to pulse distance x_{irr} . The increased distance x_{irr} decreases the intersection depth d_{ch} between the locally doped regions. For a distance $x_{irr} \geq w_{melt}$, the intersection depth drops $d_{ch} = 0$, while for a distance $x_{irr} \approx 0$, the intersection depth approaches the melt depth $d_{ch} \approx d_{melt}$.

5.2 Geometrical Consideration of Melted Regions

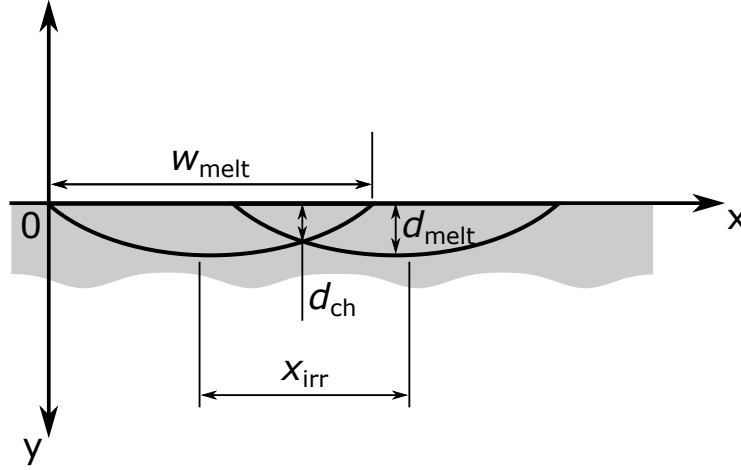


Figure 5.2: Scheme of two neighboring regions in an irradiated and doped silicon surface. Each melted region is approximated by a parabola with a width w_{melt} and a depth d_{melt} . The intersection region between the two melted regions has a depth d_{ch} . The distance between the centers of the two melted regions equals the used pulse to pulse distance x_{irr} .

Figure 5.2 schematically shows two neighboring melted regions in a cross section of an irradiated silicon wafer. Each melted region is assumed to have a parabolic shape with a width w_{melt} and a depth d_{melt} . The two parabolas are intersecting at a depth d_{ch} and their centers are away from each other equal to the used laser pulse to pulse distance x_{irr} . For the geometrical description of the variation of the intersection depth d_{ch} with the used inter-pulse distance x_{irr} , we consider the general equation of a parabola:

$$y(x) = a(x - h)^2 + m, \quad (5.3)$$

where a is a constant and (h, m) are the coordinates of the parabola vertex, which are $h = w_{\text{melt}}/2$ and $m = d_{\text{melt}}$. Since $y(x = 0) = 0$, the constant a has the value:

$$a = \frac{-m}{h^2} = \frac{-4d_{\text{melt}}}{w_{\text{melt}}^2}. \quad (5.4)$$

Thus, the equation of the left parabola is

$$y_1(x) = \frac{-4d_{\text{melt}}}{w_{\text{melt}}^2} \left(x - \frac{w_{\text{melt}}}{2} \right)^2 + d_{\text{melt}}, \quad (5.5)$$

and that of the right parabola is

$$y_2(x) = \frac{-4d_{\text{melt}}}{w_{\text{melt}}^2} \left(x - \left(\frac{w_{\text{melt}}}{2} + x_{\text{irr}} \right) \right)^2 + d_{\text{melt}}. \quad (5.6)$$

Equating the two equations (eq. 5.5 and eq. 5.6) reveals the value of x at which the two parabolas intersect:

$$\begin{aligned} a(x - h)^2 + d_{\text{melt}} &= a(x - (h + x_{\text{irr}}))^2 + d_{\text{melt}} \\ x^2 - 2xh + h^2 &= x^2 - 2x(h + x_{\text{irr}}) + (h + x_{\text{irr}})^2 \\ x &= \frac{2hx_{\text{irr}} + x_{\text{irr}}^2}{2x_{\text{irr}}} \\ x &= h + \frac{x_{\text{irr}}}{2} = \frac{w_{\text{melt}} + x_{\text{irr}}}{2}. \end{aligned} \quad (5.7)$$

Substituting eq. 5.7 into eq. 5.5, makes it possible to obtain the relationship between intersection depth d_{ch} and melt depth d_{melt} as a function of the inter-pulse distance x_{irr} as follows:

$$\begin{aligned} d_{\text{ch}} &= \frac{-4d_{\text{melt}}}{w_{\text{melt}}^2} \left(\frac{w_{\text{melt}} + x_{\text{irr}}}{2} - \frac{w_{\text{melt}}}{2} \right)^2 + d_{\text{melt}} \\ d_{\text{ch}} &= d_{\text{melt}} - \frac{x_{\text{irr}}^2 d_{\text{melt}}}{w_{\text{melt}}^2} \end{aligned} \quad (5.8)$$

$$\frac{d_{\text{ch}}}{d_{\text{melt}}} = 1 - \frac{x_{\text{irr}}^2}{w_{\text{melt}}^2}. \quad (5.9)$$

5.3 Experiment

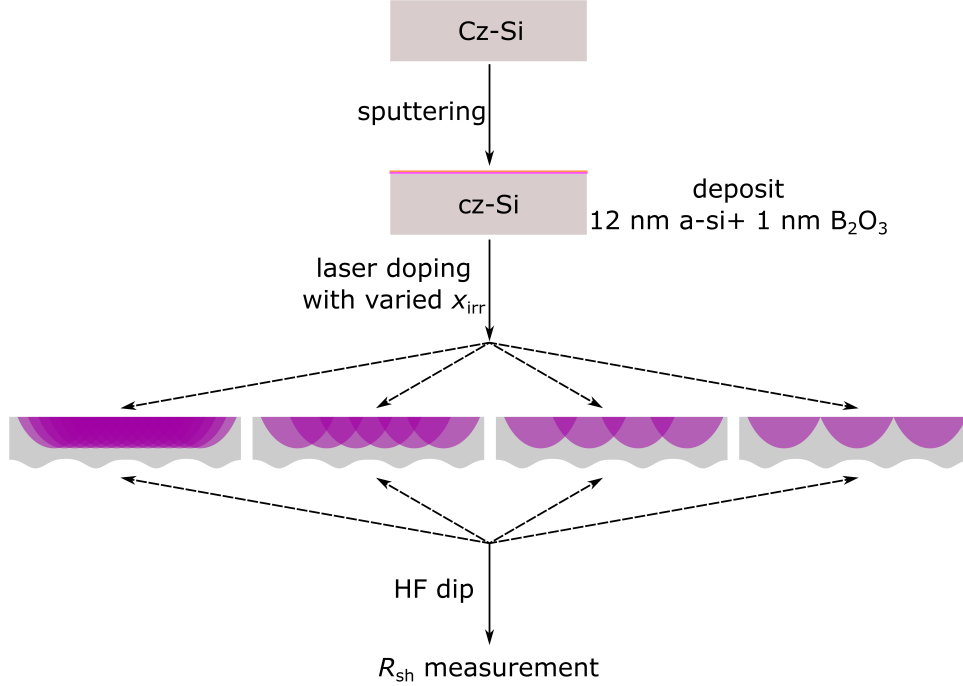


Figure 5.3: a) Schematical representation of the experimental steps followed in this chapter. A two-layer precursor system: a 1 nm thick boron oxide (B_2O_3) layer covered by 12 nm thick amorphous silicon (a-Si) deposited on a chemically cleaned Cz-Si wafer surface serves as a precursor layer (dopant source) for the laser doping process. Afterwards, a pulsed green laser irradiates the surface with a constant pulse energy density $H = 2.8 \text{ J/cm}^2$ and a varying pulse to pulse distance $1 \mu\text{m} \leq x_{irr} \leq 11 \mu\text{m}$. The varying distance x_{irr} changes the intersection depth d_{ch} between the locally doped regions (violet color). Finally, a HF-dip removes the residues on the surface and a four-point probe measurement measures the sheet resistance R_{sh} of the different doped areas with different pulse to pulse distances x_{irr} .

Figure 5.3 schematically demonstrates the experimental steps followed in this chapter to investigate the influence of using different pulse to pulse distance x_{irr} for the laser doping process. For that, Czochralski silicon (Cz-Si) is used. A HF-dip removes the native silicon oxide layer on the wafer's surface. Next, the sputtering system mentioned in sec. A.2.3 deposits a two-layer precursor system consisting

of a 1 nm boron oxide (B_2O_3) layer followed by a 12 nm amorphous silicon (a-Si) layer. The precursor layer serves as a source for doping atoms. After that, the laser system described in sec. A.2.1 irradiates the surface with a pulse energy density $H = H_{th, \text{evap, Si}} = 2.8 \text{ J/cm}^2$, a pulse repetition rate $f = 12.5 \text{ kHz}$ and a varied scanning speed $v_{\text{scan}} = 12.5 \text{ mm/s}$, 37.5 mm/s , 62.5 mm/s , 87.5 mm/s , 112.5 mm/s , and 125 mm/s . From eq. 5.1, the scanning speeds v_{scan} used correspond to pulse to pulse distances $x_{\text{irr}} = 1 \text{ }\mu\text{m}$, $3 \text{ }\mu\text{m}$, $5 \text{ }\mu\text{m}$, $7 \text{ }\mu\text{m}$, $9 \text{ }\mu\text{m}$ and $11 \text{ }\mu\text{m}$. After doping finishes, a 30 s HF-dip removes the leftover residues on the wafer's surface. Finally, a sheet resistance R_{sh} measurement of the cleaned doped surface takes place.

5.4 Results and Discussion

5.4.1 Simulation Results

The model mentioned in chapter 4 simulated the experiment described in sec. 5.3. The results from the simulation are presented in the current section.

Figure 5.4 exhibits the measured sheet conductance G_{sh} of the laser doped layer using different inter-pulse distance x_{irr} . With the increasing distance x_{irr} , the measured conductance G_{sh} non-linearly decreases as a result of either decreasing the incorporated doping (boron) atoms amount (called dose D_B) or changing of layer's geometry. The non-linear decrease is very well described using a second order fit equation. At distance $x_{\text{irr}} = 0$ (the case of a furnace-diffused layer with homogeneous layer's depth), sheet's conductance G_{sh} equals the maximum reachable sheet conductance $G_{\text{sh, max}}$ that one can reach under the used experimental conditions. At distance $x_{\text{irr}} = 9.75 \text{ }\mu\text{m}$ (the melt width w_{melt} as shown in the microscopic insert), the resulted sheet conductance G_{sh} drops to zero, however being highly doped, which indicates the physical non-connection between the locally doped regions. From the previous two conditions, the fit equation is rewritten as following:

$$G_{\text{sh}} = G_{\text{sh, max}} \left(1 - \frac{x_{\text{irr}}^2}{w_{\text{melt}}^2} \right). \quad (5.10)$$

To find out the exact reason for the reducing sheet conductance G_{sh} with increasing the used distance x_{irr} , the work uses the model mentioned in the previous chapter to simulate this experiment.

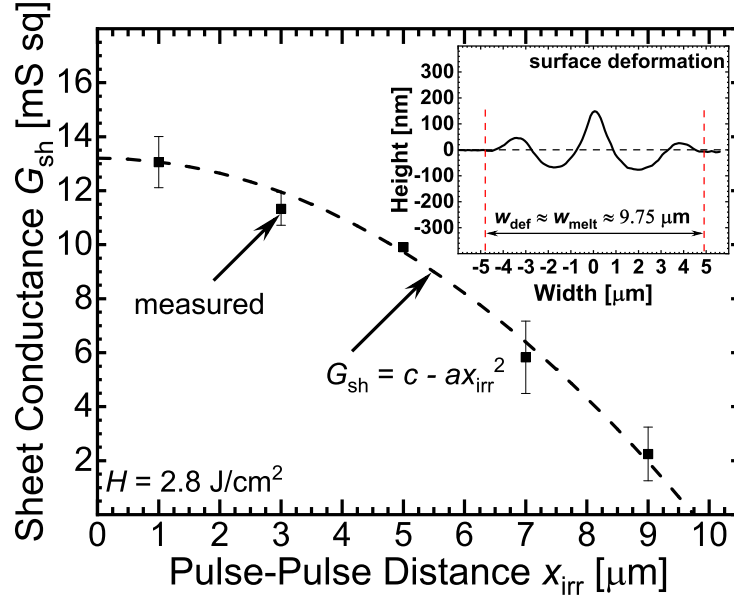


Figure 5.4: Sheet conductance G_{sh} of the doped surface decreases with the used pulse to pulse distance x_{irr} . The measured data points are perfectly fitted using a second order equation. The reduction of the resulted sheet conductance G_{sh} with increasing distance x_{irr} is only explainable by either the reducing amount of incorporated doping atoms in the doped layer or the changing layer's geometry due to x_{irr} variation. The case of distance $x_{irr} = 0$ (where the measured sheet conductance $G_{sh} = \text{maximum reached conductance } G_{sh,max}$) corresponds to a furnace-diffused layer with a homogeneous laterally distributed doping profile and layer's depth. The case of pulse-pulse distance $x_{irr} = 9.75 \mu\text{m}$ (where the measured sheet conductance G_{sh} drops to 0) corresponds the case where the locally doped regions are physically non-connected. The microscopic insert (surface deformation caused by irradiating a polished silicon wafer surface with a single laser pulse of energy density $H = 2.8 \text{ J/cm}^2$) confirms the melt width w_{melt} value ($w_{melt} = 9.75 \mu\text{m}$).

Figure 5.5 demonstrates the concentration maps resulted from simulating the experiment shown in fig. 5.3. The grey region is the undoped silicon (base doping of 10^{16} cm^{-3}), whereas the colored region is the boron-doped region. In order to find the doping profile of each doped layer, the concentration is laterally averaged over the hashed areas. The pn-junction depth $d_{pn,lat}$ resulted from the averaged doping profiles is represented by the red dashed line. The depth $d_{pn,ch}$ of the intersection

region between the melted regions is extracted from the simulated data and is represented by the blue dashed line. The green dashed line represents the maximum pn-junction depth reached.

Figure 5.5a shows the concentration map resulted when using distance $x_{irr} = 1 \mu\text{m}$. Here both, doping concentration and doped depth, are homogeneous laterally over the x-axis. Therefore, the three depths, $d_{pn,ch}$, $d_{pn,lat}$ and $d_{pn,max}$, are almost coinciding.

Figure 5.5b demonstrates the concentration map resulted when using distance $x_{irr} = 3 \mu\text{m}$ for doping. Due to increasing the used distance x_{irr} , the lateral homogeneity of doping concentration and doped depth decreases. Therefore, the depth $d_{pn,ch}$ decreases relative to the two depths $d_{pn,lat}$ and $d_{pn,max}$ as a result of moving the melted regions away from each other.

Figure 5.5c demonstrates the concentration map resulted when using distance $x_{irr} = 5 \mu\text{m}$ for doping. The increased distance x_{irr} deteriorates the lateral homogeneity of doping concentration and doped depth. Therefore, the depth $d_{pn,ch}$ decreases more relative to the two depths $d_{pn,lat}$ and $d_{pn,max}$ as a result of moving the melted regions away from each other.

Figure 5.5d demonstrates the concentration map resulted when using distance $x_{irr} = 7 \mu\text{m}$ for doping. The increased distance x_{irr} decreases the lateral homogeneity of doping concentration and doped depth. Therefore, the depth $d_{pn,ch}$ decreases more relative to the two depths $d_{pn,lat}$ and $d_{pn,max}$ as a result of moving the melted regions away from each other.

Figure 5.5e demonstrates the concentration map resulted when using distance $x_{irr} = 9 \mu\text{m}$ for doping. Here, as a result of increasing the used distance x_{irr} , the lateral homogeneity of doping concentration and doped depth almost demolishes. The concentration picture almost repeats with each single locally doped area. The depth $d_{pn,ch}$ drops to be almost 50 nm.

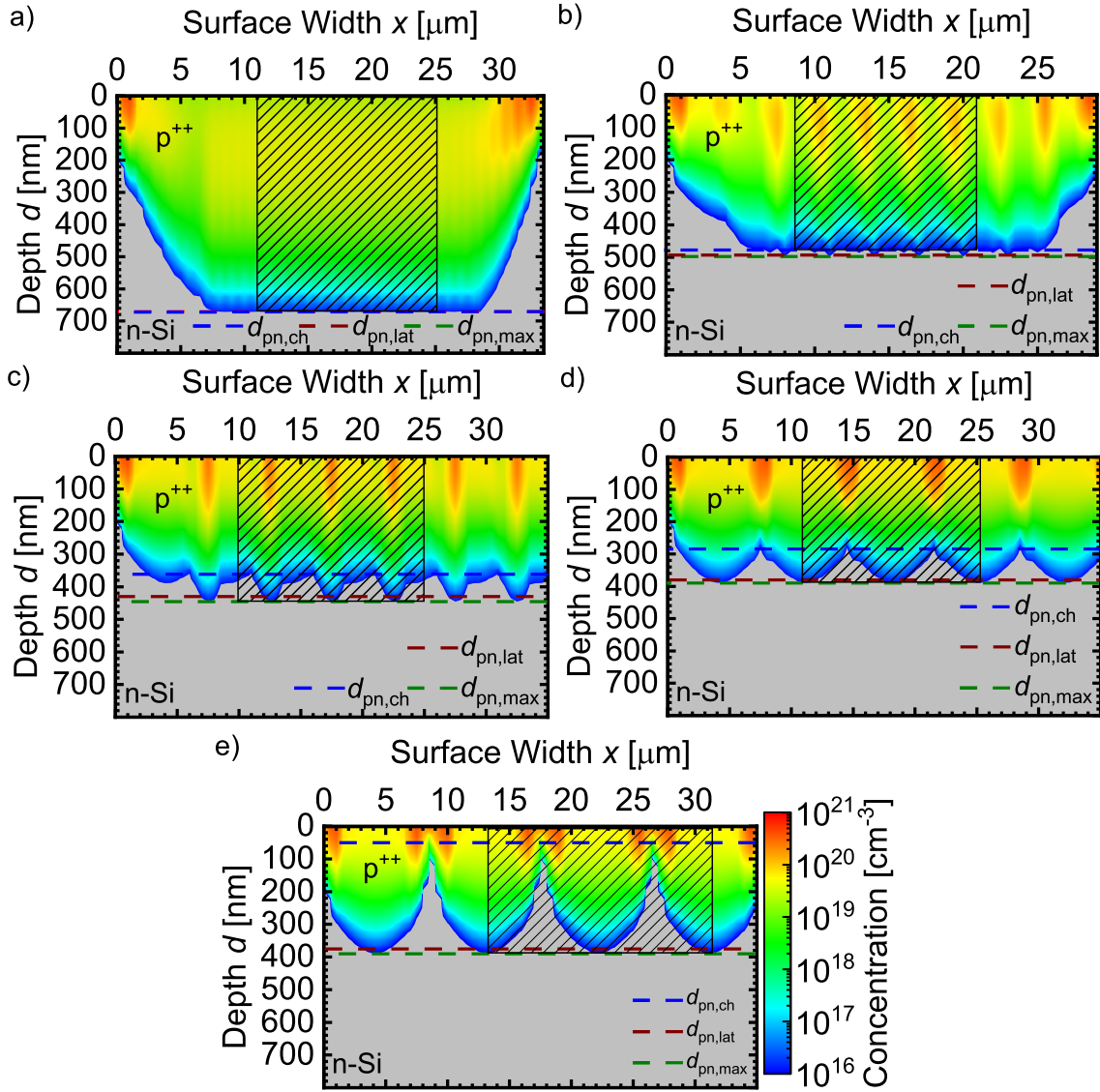


Figure 5.5: A cross sectional concentration map of the laser doped layer using varied inter-pulse distance x_{irr} : a) $x_{irr} = 1 \mu\text{m}$, b) $x_{irr} = 3 \mu\text{m}$, c) $x_{irr} = 5 \mu\text{m}$, d) $x_{irr} = 7 \mu\text{m}$, e) $x_{irr} = 9 \mu\text{m}$. The colored region is the doped region, whereas the grey region is the undoped silicon with base doping of 10^{16} cm^{-3} . For each layer, the doping profile is the laterally averaged concentration over the hashed area. The three depth $d_{pn,ch}$, $d_{pn,lat}$ and $d_{pn,max}$ correspond to the pn-junction depth in the melted channel region, the pn-junction depth resulted from the laterally averaged doping profiles (shown in fig. 5.6) and the maximum pn-junction depth respectively.

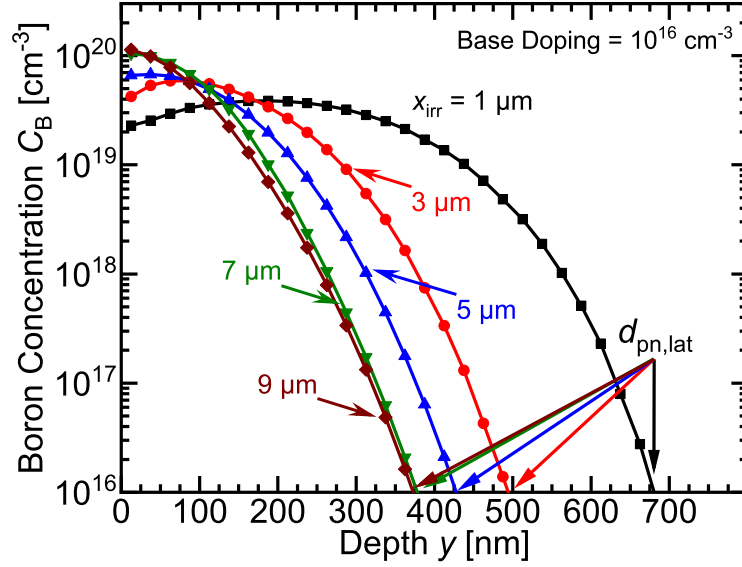


Figure 5.6: Simulated doping profiles for the irradiated surface using different pulse to pulse distance x_{irr} . Since the doping level of the base silicon is 10^{16} cm^{-3} , the intersection between the doping profiles with the depth axis y gives the pn-junction's depth $d_{pn,lat}$. The depth $d_{pn,lat}$ decreases and the surface concentration $C_B(d = 0)$ increases with the increasing pulse to pulse distance x_{irr} as a result of non-sufficient diffusion time. A wider pulse to pulse distance x_{irr} melts every superficial point less often, which provides less time for dopants to diffuse from the high concentration $C_B(d = 0)$ surface to the low concentration C_B in the depth d . Subsequently, the surface concentration $C_B(d = 0)$ increases when increasing the distance x_{irr} . This causes the pn-junction's depth $d_{pn,lat}$ to shrink. The area under the curve represents the number of boron atoms existing in the doped layer per unit area and is called dose D_B . Figure 5.7 shows the variation of the doping dose D_B with throughout the doped layer depth y .

Figure 5.6 represents the doping profiles simulated by the model mentioned in chapter 4 for the irradiation cases of sec. 5.3. Since the melted region's center coincides with the irradiating pulse center, a wider pulse to pulse distance x_{irr} decreases the overlap O_x between the locally melted regions. As a result, each point at the surface is less frequently irradiated and melted, which does not provide sufficient time for doping atoms to diffuse from the high concentration C_B surface (where the doping atoms source exists) to the lower concentration C_B depth. Therefore,

the increased inter-pulse distance x_{irr} results in a high concentration $C_B(d = 0)$ of boron at the surface and a shallow pn-junction's depth $d_{\text{pn,lat}}$. Since the doping concentration of the base silicon is 10^{16} cm^{-3} , the intersection between the doping profiles with the depth axis y gives the pn-junction's depth $d_{\text{pn,lat}}$. The area under each curve calculated through

$$D_B = \int_0^y C_B(y) dy. \quad (5.11)$$

gives the amount (dose D_B) of boron atoms incorporated in the doped layer per unit area for each irradiation case. The variation of the dose D_B with the doped layer depth y is shown in fig. 5.7.

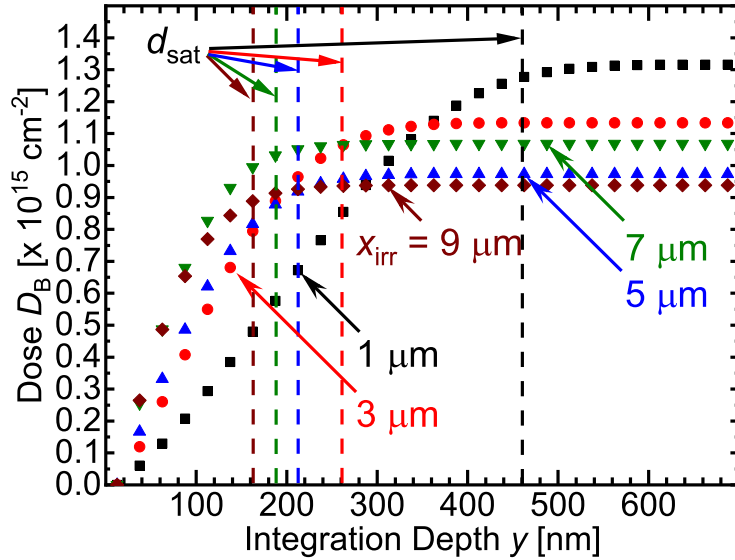


Figure 5.7: The integration of the simulated doping profiles, shown in fig. 5.6, over the doped layer depth y , using eq. 5.11, demonstrates a saturation curve shape. For each distance x_{irr} , the dose D_B increases linearly with the integration depth y until reaching a saturation point where further increasing the depth y does not significantly add to the dose D_B . The depth d_{sat} of this saturation point indicates the depth y deeper than which the existing doping atoms do not significantly add to the resulting sheet conductance G_{sh} .

Figure 5.7 shows the variation of the dose D_B over the doped layer's depth y . Integrating the simulated laterally-averaged doping profile (in fig. 5.6) over the

depth y results in a saturation curve shape. The dose D_B linearly increases with the integration depth y till reaching a depth (called saturation depth d_{sat}) deeper than which does not significantly contribute to the resulting dose D_B . That implies that the incorporated doping atoms existing deeper than the depth d_{sat} barely contributes to increasing the dose D_B , and thus to the measured sheet conductance G_{sh} .

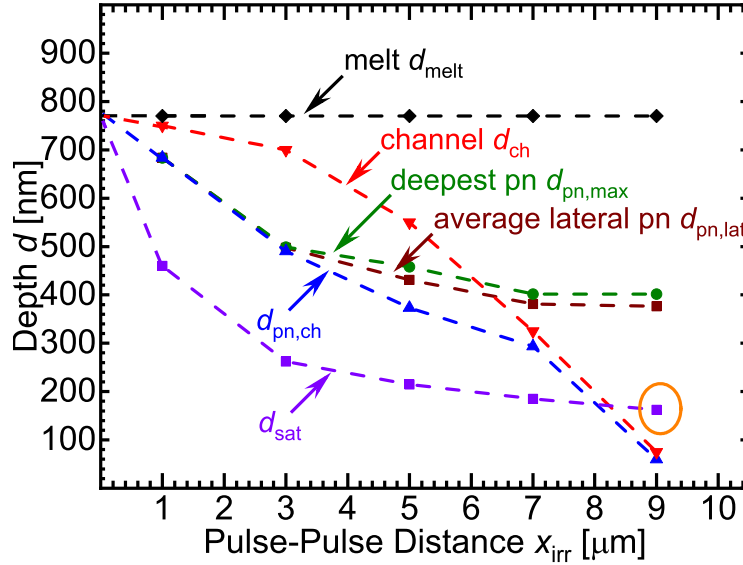


Figure 5.8: A representation of all simulated depths of interest. As the melt depth d_{melt} mainly depends on the used pulse energy density, which is constant for all distance x_{irr} cases ($H = 2.8 \text{ J/cm}^2$), the depth d_{melt} stays unchanged with varying the distance x_{irr} . Contrarily, Both, the channel's depth d_{ch} and the pn-junction depth $d_{\text{pn,ch}}$ in the channel region, non-linearly decrease with increasing the used distance x_{irr} . The maximum pn-junction depth $d_{\text{pn,max}}$, the laterally-averaged doping profile depth $d_{\text{pn,lat}}$ and the saturation depth d_{sat} decrease with increasing the distance x_{irr} . This decrease of the two depths: $d_{\text{pn,max}}$ and $d_{\text{pn,lat}}$ is limited by the depth of a single doped region with 0% overlap. The same applies to the saturation depth d_{sat} decrease with the increasing distance x_{irr} . For the cases $0 \leq x_{\text{irr}} \leq 7 \mu\text{m}$, the saturation depth d_{sat} is smaller than the smallest doped depth $d_{\text{pn,ch}}$ which implies that almost 100% of the available dose D_B is contributing to the resulting sheet conductance G_{sh} . For $x_{\text{irr}} = 9 \mu\text{m}$, the depth d_{sat} (the point in the orange circle) is smaller than $d_{\text{pn,ch}}$ which signifies that only a portion of the existing dose D_B contributes to G_{sh} .

Figure 5.8 shows the key depths existing in the laser doped layers. The melted

depth d_{melt} is only dependent on the supplied energy density which is constant for all the irradiated cases ($H = 2.8 \text{ J/cm}^2$). The melted channel depth d_{ch} and the pn-junction depth $d_{\text{pn,ch}}$ non-linearly decrease with increasing pulse distance x_{irr} . The maximum pn-junction depth $d_{\text{pn,max}}$ and the pn-junction depth $d_{\text{pn,lat}}$ (from fig. 5.6) decrease with increasing the distance x_{irr} . The decreasing trend is limited by the depth of a non-overlapping doped region (caused by irradiating with a single last pulse). The saturation depth d_{sat} , which defines the effectively-contributing doped depth to the dopant dose D_{B} , is for $0 \text{ } \mu\text{m} \leq x_{\text{irr}} \leq 7 \text{ } \mu\text{m}$ less than the shallowest doped layer of depth $d_{\text{pn,ch}}$. That implies that for the case $0 \text{ } \mu\text{m} \leq x_{\text{irr}} \leq 7 \text{ } \mu\text{m}$, almsot 100% of the available doping in the doped layer is contributing to the measured sheet conductace G_{sh} . For $x_{\text{irr}} = 9 \text{ } \mu\text{m}$, the depth $d_{\text{sat}} > d_{\text{pn,ch}}$ which means that the available doping only partially contributes to the total dose D_{B} . Full or partial contribution to the does D_{B} means also full or partial contribution to the measured sheet conductance G_{sh} .

Figure 5.9 shows the doping atoms' dose: $D_{\text{B,full}}$ and $D_{\text{B,act}}$ which are calculated (using eq. 5.11 when integrating to $y = d_{\text{pn,lat}}$) from the simulated laterally-averaged doping profiles (shown in fig. 5.6) and calculated from the measured sheet conductance G_{sh} (shown in fig. 5.4) using eq. 2.2 (assuming an average hole mobility $\bar{\mu}_{\text{h}} = 68 \text{ cm}^2/(\text{V s})$ [36, 37]). The calculated dose $D_{\text{B,act}}$ is smaller than the simulated dose $D_{\text{B,full}}$ for all the distances x_{irr} . At $x_{\text{irr}} = 7 \text{ } \mu\text{m}$, the difference between both doses: $D_{\text{B,act}}$ and $D_{\text{B,full}}$ is significant, so that using another suitable hole mobility μ_{h} value would not compensate it. As shown in fig. 5.8, at $x_{\text{irr}} = 7 \text{ } \mu\text{m}$, the saturatiion depth d_{sat} is smaller than the smallest doped layer's deth $d_{\text{pn,ch}}$ which implies that 100% of the available dose $D_{\text{B,full}}$ should be contributing to the measured sheet conductance G_{sh} . Since $D_{\text{B,act}} < D_{\text{B,full}}$, then the reason for the decreasing sheet conductance G_{sh} with the increasing distance x_{irr} is not the decreasing dose $D_{\text{B,full}}$, but the changing layer's geometry. Furthermore, all the doses D_{B} lie in the same order of magnitude, with some slight variation. Since the difference is negligible, this work assumes that all layers contain the same dose D_{B} which equals the average dose $\bar{D}_{\text{B}} \approx 1.2 \times 10^{15} \text{ cm}^{-2}$. The reason for obtaining the same boron dose $D_{\text{B}} = \bar{D}_{\text{B}}$ in all cases is that the used pulse to pulse distance x_{irr} does not exceed the melt width, $x_{\text{irr}} \leq w_{\text{melt}}$. For a distance range $x_{\text{irr}} \leq w_{\text{melt}}$, the laser irradiates 100% of the precursor layer's area that is available for doping. When the used inter-pulse distance x_{irr} exceeds the melt width, i.e. for $x_{\text{irr}} > w_{\text{melt}}$, the laser does not irradiate the available precursor

areas in-between the subsequent melted regions.

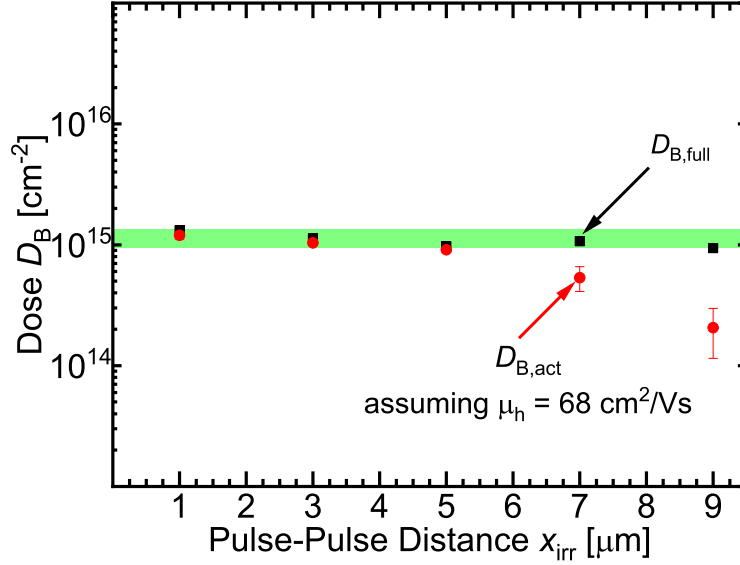


Figure 5.9: The calculated doses $D_{B,act}$, from the measured sheet conductance G_{sh} shown in fig. 5.4 using eq. 2.2 (assuming an average hole mobility $\bar{\mu}_h = 68 \text{ cm}^2/(\text{V s})$ [36, 37]), lie below the simulated doses $D_{B,full}$, which is extracted from fig. 5.9 using eq. 5.11 (integration limit: $y = d_{pn,lat}$), for all the distance x_{irr} cases. Since saturation distances $0 \leq x_{irr} \leq 7 \text{ } \mu\text{m}$ is smaller than the shallowest doped layer's depth $d_{pn,ch}$, then it is predicted that the actual dose $D_{B,act}$ should be coinciding with the total dose $D_{B,full}$. However, the dose $D_{B,act}$ at $x_{irr} = 7 \text{ } \mu\text{m}$ is significantly smaller than the full dose $D_{B,full}$. This difference is uncompensated by assuming another suitable mobility μ_h value. Furthermore, the total doses $D_{B,full}$ for all irradiated cases do not significantly vary. Therefore, the decreasing measured sheet conductance G_{sh} is not because of decreasing the dose $D_{B,full}$ but due to the changing layer's geometry. The negligibly small variation in doses $D_{B,full}$ originates from the full consumption of the available precursor on the silicon surface as a result of irradiating using an inter-pulse distance $x_{irr} \leq w_{melt}$. Thus, we assume that the average boron dose, which exists in all doped layers, is constant, $D_B = \bar{D}_B \approx 1.2 \times 10^{15} \text{ cm}^{-2}$.

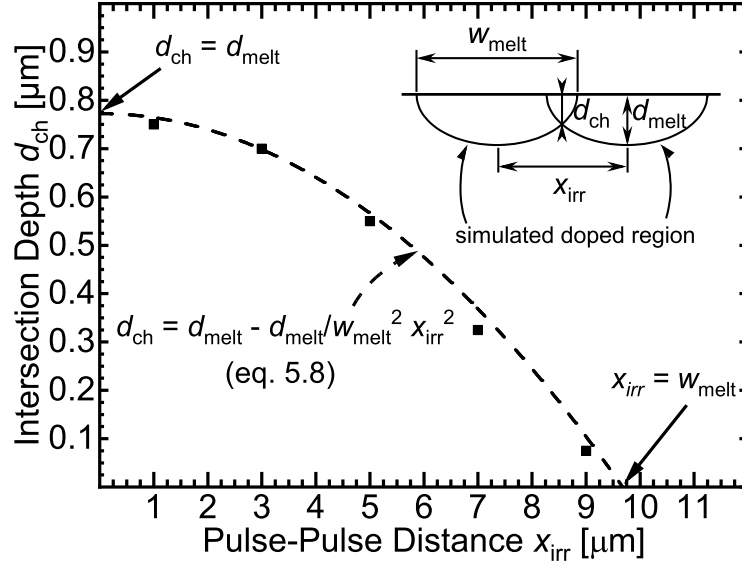


Figure 5.10: From the simulated cases, the intersection depth d_{ch} decreases with the increasing pulse to pulse distance x_{irr} . The intersection region is the connecting region between the subsequent locally melted regions. The curve (the dashed line), calculated using eq. 5.8, perfectly fits the intersection depths d_{ch} . This demonstrates that the resulting melt form has a parabolic shape, and thus, is describable using eq. 5.8. The parabolic form of the melted volume originates from the Gaussian intensity distribution nature of the laser beam. Therefore, the increasing pulse to pulse distance x_{irr} decreases the intersection depth d_{ch} quadratically. At an inter-pulse distance $x_{irr} = 0$, similar to the case of a furnace-diffused layer, the intersection depth equals the melt depth, i.e. $d_{ch} = d_{melt}$. At an inter-pulse distance $x_{irr} \geq w_{melt}$, the intersection depth d_{ch} drops to zero which completely separates the locally doped regions from each other.

Figure 5.10 shows the melted intersection depth d_{ch} resulting from the simulation of the cases shown in fig. 5.5 versus the inter-pulse distance x_{irr} . The increasing pulse to pulse distance x_{irr} decreases the depth d_{ch} . Assuming a parabolic form of the melted silicon region that results from melting with the Gaussian intensity-distributed laser beam leads to a perfect fit for the simulated data when using eq. 5.8. At overlap $O_x = 100\%$ (distance $x_{irr} = 0$), the intersection depth is $d_{ch} = d_{melt}$, whereas at pulse to pulse distance $x_{irr} \geq w_{melt}$, the intersection depth drops $d_{ch} = 0$. Intersection depth $d_{ch} = 0$ means that the doped regions are not connected to

each other.

In the light of all the previous graphs, we deduce that the drop of sheet conductance shown in fig. 5.4 when increasing the used pulse to pulse distance x_{irr} at pulse energy density $H = 2.8 \text{ J/cm}^2$ results from the changing layer's geometry and not the reducing doping atoms dose D_B . From figure 5.10, at a distance $x_{\text{irr}} = 0$ (overlapping $O_x = 100\%$), the doped layer has a regular depth d_{melt} . Regular layer's depth d_{melt} means that no depth discrepancies over the layer's width (x-direction) exist, i.e $d_{\text{ch}} = d_{\text{melt}}$. As a result, the sheet conductance of that doped layer equals the maximum reachable sheet conductance ($G_{\text{sh}} = G_{\text{sh, max}} \approx 13.2 \text{ mS}\square$) using the current system (laser parameters, precursor type and thickness and substrate conditions). Conversely, for a distance equal to or exceeding the melt width $x_{\text{irr}} \geq w_{\text{melt}}$, the overlap between locally doped regions drops $O_x = 0\%$. Therefore, the depth d_{ch} of the intersection zone drops $d_{\text{ch}} = 0$ which electrically separates and isolates the locally doped regions from each other. Consequently, the measured sheet conductance drops to zero $G_{\text{sh}} = 0$, although the layer is highly doped. From fig. 5.9, sheet conductance G_{sh} calculated by eq. 2.2 overestimates the sheet conductance G_{sh} as distance x_{irr} increases. According to eq. 2.2, dose D_B of boron in the doped sheet is the only factor affecting the measured sheet conductance G_{sh} . Since boron dose D_B stays constant when changing the used pulse to pulse distance in the range $0 \leq x_{\text{irr}} \leq w_{\text{melt}}$, the variation in boron dose D_B is not the root cause of the dropping sheet conductance G_{sh} . Accordingly, the change in the doped layer's geometry is the factor which affects the sheet conductance G_{sh} in this experiment, and not the dose D_B of incorporated boron. This explains the perfect fit of the measured sheet conductance G_{sh} when using a quadratic function, as intersection depth d_{ch} quadratically drops with the increasing distance x_{irr} . The fit equation used is

$$G_{\text{sh}}(x_{\text{irr}}) = G_{\text{sh}}(x_{\text{irr}} = 0) \left(1 - \frac{x_{\text{irr}}^2}{w_{\text{melt}}^2} \right). \quad (5.12)$$

The value of sheet conductance G_{sh} at $x_{\text{irr}} = 0$ is expressed as follows:

$$G_{\text{sh}}(x_{\text{irr}} = 0) = G_{\text{sh, max}} = q \bar{\mu}_h \bar{D}_B, \quad (5.13)$$

where q is electron charge and $\bar{\mu}_h$ is average hole mobility. Substituting eq. 5.13 in eq. 5.12 reveals the dependence of sheet conductance G_{sh} on boron dose \bar{D}_B as

expressed:

$$G_{\text{sh}}(x_{\text{irr}}) = q \mu_{\text{h}} \bar{D}_{\text{B}} \left(1 - \frac{x_{\text{irr}}^2}{w_{\text{melt}}^2} \right). \quad (5.14)$$

From eq. 5.9, we replace the term $\left(1 - \frac{x_{\text{irr}}^2}{w_{\text{melt}}^2} \right)$ as follows:

$$G_{\text{sh}}(x_{\text{irr}}) = q \mu_{\text{h}} \bar{D}_{\text{B}} \frac{d_{\text{ch}}}{d_{\text{melt}}} = q \mu_{\text{h}} \bar{D}_{\text{B}} \frac{d_{\text{min}}}{d_{\text{max}}}. \quad (5.15)$$

Equation 5.15 implies that the change of the measured sheet conductance G_{sh} is linearly proportional to the ratio of intersection depth d_{ch} to melt depth d_{melt} and the mean doping dose \bar{D}_{B} . This means that the amount of doping atoms contributing to current flow is the full dose \bar{D}_{B} scaled down by the ratio of the minimum depth d_{min} to the maximum depth d_{max} .

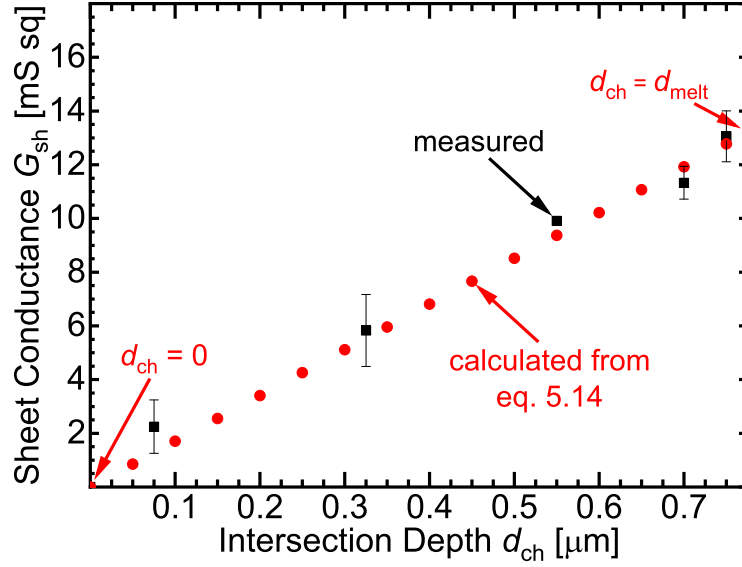


Figure 5.11: Assuming an average mobility $\bar{\mu}_h = 68 \text{ cm}^2/(\text{V s})$ and an average dose $\bar{D}_B = 1.2 \times 10^{15} \text{ cm}^{-2}$, the measured and the calculated (using eq. 5.15) sheet conductance G_{sh} show a good agreement. The agreement reveals that 100% of the boron dose D_B contributes to the charge carrier flow if the sheet's depth is regular, $y(x) = d_{melt}$, which is the condition of eq. 2.2. The irregularity in the sheet's depth ($d_{ch} \leq d_{melt}$) causes a linear scaling of the dose \bar{D}_B to the ratio $\frac{d_{ch}}{d_{melt}}$. Consequently, the ratio between intersection depth d_{ch} to melt depth d_{melt} plays the most crucial role for sheet conductance G_{sh} when varying the used pulse to pulse distance x_{irr} , as dose $D_B = \bar{D}_B$ is constant. The case of intersection depth $d_{ch} = 0$ results when the pulse to pulse distance $x_{irr} \geq w_{melt}$.

Figure 5.11 demonstrates a good agreement between the measured and the calculated sheet conductance G_{sh} when using eq. 5.15. Based on the value of the average boron dose $\bar{D}_B = 1.2 \times 10^{15} \text{ cm}^{-2}$, we assumed an average mobility $\bar{\mu}_h = 68 \text{ cm}^2/(\text{V s})$ [36, 37]. The good agreement uncovers the mechanism of charge carrier flow in a doped layer. The entire amount of doping atoms (boron dose \bar{D}_B) incorporated in the sheet is contributing to current flow if the sheet depth is regular ($y(x) = d_{melt}$), and that is the validity range of eq. 2.2. In the case of irregular sheet's depth ($d_{ch} < d_{melt}$), the amount of doping atoms contributing to current flow shrinks to the ratio of minimum available connection depth d_{min} to the maximum available connection depth d_{max} . Therefore, when varying pulse to pulse distance in the range

$0 \leq x_{\text{irr}} \leq w_{\text{melt}}$, boron dose D_{B} stays constant and sheet conductance G_{sh} reduces by the ratio between the minimum depth $d_{\text{min}} = d_{\text{ch}}$ and the maximum depth $d_{\text{max}} = d_{\text{melt}}$, as stated in eq. 5.15.

This work showed the linear dependence of the sheet conductance G_{sh} of a laser-doped sheet on the ratio between the intersection depth d_{ch} to the layer's depth d_{melt} when inter-pulse distance varies in the range $0 \leq x_{\text{irr}} \leq w_{\text{melt}}$. When the ratio $d_{\text{ch}}/d_{\text{melt}} = 1$ (like a furnace-diffused layer), 100% of doping atoms contribute to the current flow and then eq. 2.2 is valid, whereas when the ratio drops $d_{\text{ch}}/d_{\text{melt}} = 0$ (electrically isolated locally doped regions), sheet conductance vanishes $G_{\text{sh}} = 0$, and therefore, eq. 2.2 is invalid. Therefore, using the correct laser parameters for doping is crucial to obtain the required electrical properties.

Conclusion

This work presents a unified model for laser doping of silicon from a precursor using a wide energy density range. The model is capable of simulating the various doping cases: liquid silicon/liquid precursor, liquid silicon/gaseous precursor, and liquid silicon/gaseous silicon/gaseous precursor. The used precursor materials and the used laser energy density determine the doping case. Moreover, unlike the previously published models, here we predict not only the doping profile but also the dimensions of the melted volume.

The model showed that the Gaussian distribution of the beam's intensity causes a temperature gradient-induced surface tension gradient along the melt width, which circulates the melt and enhances the diffusion process. The circulation-assisted diffusion has a higher pre-exponential factor value $D_0 = 8 \times 10^{-4} \text{ cm}^2/\text{s}$ when the surface temperature T_{surf} exceeds 2100 K. We also showed that 50% of the evaporated materials recondense after the pulse ends and then provides an additional dopant source for the subsequent pulses. At a high laser energy density, the model showed that the energy coupling in the evaporated tube-like capillary increases. Finally, the model showed that in the case of using a solid precursor, the usage of amorphous silicon as a part of the precursor system allows the diffusion process to start before crystalline silicon melts.

The unified model interpreted the dependence of the sheet conductance G_{sh} on the doped layer dimensions: the sheet conductance G_{sh} is directly proportional to the ratio between the intersection depth d_{ch} and the complete doped layer's depth d_{melt} and the average doping dose \bar{D}_{B} . Furthermore, the model revealed that each melted region has a parabolic form, and thus, the intersection depth d_{ch} between the doped regions quadratically changes with the inter-pulse distance x_{irr} . Moreover, the model demonstrated that the boron dose D_{B} incorporated in the laser doped layer is not significantly altering when varying the pulse to pulse distance x_{irr} . Therefore,

the sheet conductance G_{sh} linearly changes with the ratio $d_{\text{ch}}/d_{\text{melt}}$. For a pulse to pulse distance $x_{\text{irr}} \geq w_{\text{melt}}$, the locally doped regions are non-intersecting/non-connecting, and hence, no continuous layer results ($G_{\text{sh}} = 0$).

Appendix A

Appendix

A.1 Material Properties

A.1.1 Optical Properties

The dependencies of the refractive index real part n_{Si} and the absorption coefficient α_{Si} in equations A.1, A.3, and A.2 as well as the constants C_n and C_α come from the published data by Martin A. Green [74]. The temperature dependence of the refractive index real part $n_{\text{Si}}(T)$ of solid silicon is expressed as following:

$$n_{\text{s-Si}}(T) = n_{\text{s-Si}}(T_0) \left(\frac{T}{T_0} \right)^{(C_n(T_0)T_0)} = 4.151 \left(\frac{T}{300} \right)^{(1.2 \times 10^{-4} \times 300)} \quad (\text{A.1})$$

and of liquid silicon $n_{\text{l-Si}} = 3.04$ [77]. The extinction factor $\kappa_{\text{s-Si}}(T)$ is then calculated as

$$\kappa_{\text{s-Si}}(T) = \frac{\alpha_{\text{abs,s-Si}}(T) \lambda_0}{4 \pi n_{\text{s-Si}}(T)} \quad (\text{A.2})$$

and that of the liquid silicon $\kappa_{\text{l-Si}} = 4.87$ [77]. The absorption coefficient $\alpha_{\text{abs,s-Si}}(T)$ of solid silicon is represented as following:

$$\alpha_{\text{abs,s-Si}}(T) [\text{cm}^{-1}] = \alpha_{\text{abs,s-Si}}(T_0) \left(\frac{T}{T_0} \right)^{(C_\alpha(T_0)T_0)} = 7850 \left(\frac{T}{300} \right)^{(33 \times 10^{-4} \times 300)} \quad (\text{A.3})$$

and of liquid silicon [77] is expressed as following:

$$\alpha_{\text{abs,l-Si}} [\text{cm}^{-1}] = \frac{4\pi\kappa_{\text{l-Si}}}{\lambda_0[\text{cm}]} \quad (\text{A.4})$$

A.1.2 Thermal and Mechanical Properties

Table A.1 and A.2 shows the material data used in the current work.

Table A.1: *Properties of crystalline silicon*

Property	Solid	Liquid	Unit	Reference
Density ρ_{Si}	$2330 - 2.19 \times 10^{-2} T$	$2540 - 2.19 \times 10^{-2} T - 1.21 \times 10^{-5} T^2$	$\left[\frac{\text{Kg}}{\text{m}^3}\right]$	[83, 91]
Thermal conductivity k_{Si}	$22.23 + 422.52 \times \exp\left(\frac{-T}{255.45}\right)$	62	$\left[\frac{\text{W}}{\text{m K}}\right]$	[90, 91]
Heat capacity c_{pSi}	$352.43 + 1.78 T - 2.21 \times 10^{-3} T^2 + 1.3 \times 10^{-6} T^3 - 2.83 \times 10^{-10} T^4$	1021.84	$\left[\frac{\text{J}}{\text{Kg K}}\right]$	[91]
Latent Heat H_{Si}	1800(Melting)	16207(Vaporation)	$\left[\frac{\text{kJ}}{\text{Kg}}\right]$	[76, 91]

Table A.2: *Properties of precursor layer*

Property	Solid	Liquid	Unit	Reference
Melting Temperature $T_{\text{melt a-Si}}$	1420(Melting)	–	[K]	[87]
Melting Temperature $T_{\text{melt B}_2\text{O}_3}$	723(Melting)	–	[K]	[85, 86]
Evaporation Temperature $T_{\text{evap B}_2\text{O}_3}$	–	1773	[K]	[85]
Latent Heat $H_{\text{melt B}_2\text{O}_3}$	0.317(Melting)	4.308(Vaporation)	$\left[\frac{\text{J}}{\text{Kg}}\right]$	[85]

Table A.3: Material properties data of boron oxide B_2O_3 .

Temperature T [K]	$k_{B_2O_3}$ $[\frac{W}{cm \cdot K}]$	Temperature T [K]	$c_{PB_2O_3}$ $[\frac{cal}{g \cdot K}]$	Temperature T [K]	$\rho_{B_2O_3}$ $[\frac{g}{cm^3}]$
303.4	0.0052	243.6	0.187	411	1.693
876.1	0.0099	286.4	0.2134	450	1.671
981.1	0.0107	389.1	0.2654	500	1.648
1076.5	0.0114	483.4	0.3056	550	1.626
1175.1	0.0121	595.6	0.344	600	1.609
1273.8	0.013	740.1	0.389	700	1.58
1381.9	0.0139	862.6	0.4437	800	1.559
1474.1	0.0141	976.3	0.444	900	1.541
1572.5	0.0136	1138.4	0.4483	1000	1.528
1689.8	0.0119	1373.7	0.4467	1100	1.518
		1744.7	0.4472	1201	1.509
				1300	1.503
				1400	1.498

(a) Thermal conductivity data of boron oxide $[\frac{W}{m \cdot K}]$ [104]. (b) Heat capacity data of boron oxide $[\frac{cal}{g \cdot K}]$ [95]. (c) Density data of boron oxide $[\frac{g}{cm^3}]$ [94, 105].

A.2 Experimental Facilities

A.2.1 Laser System

Figure A.1 schematically shows the laser system used in ipv for laser doping of silicon. The system consists of a neodymium-doped yttrium aluminum garnet (Nd:YAG) crystal-containing head. The Nd:YAG crystal acts as the active medium as explained in section 2.3.2. A series of diodes pump the Nd:YAG to emit laser beam. Normally a beam with wavelength $\lambda = 1064$ nm is emitted from the Nd:YAG crystal. A non-linear crystal doubles the frequency of the output beam (wavelength $\lambda = 1064$ nm) turning it into green light (wavelength $\lambda = 532$ nm). A non-linear crystal is a material that lacks inversion symmetry. The frequency-doubled Nd:YAG laser passes then through the optical system. The first component in the optical system is the three-lens telescope system. The lenses are convex, concave and then convex

lens. The 3-lens telescope expands the input beam in a relatively short distance by approximately a factor of 2. The first two lenses diverge the beam to the required diameter, while the third lens collimates the beam. The expanded collimated beam passes then through the second component in the optical system, which consists of a $\lambda/2$ plate and a Glan-Taylor polarizing cube prism. The $\lambda/2$ plate is mounted in a rotary mount. The combination of the rotation of the $\lambda/2$ plate with the Glan-Taylor polarization cube allows an exact control of the emitted laser power, without changing the pulse duration τ_p of the laser pulse. Alternatively, the variation of the pumping optical power changes the output laser power and the pulse duration τ_p of the laser pulse. Here, the $\lambda/2$ plate is used to rotate the polarization of the emitted laser beam, whereas the Glan-Taylor polarization prism splits the laser beam into two perpendicular polarization in two perpendicular directions. One part is absorbed by a beam dump. The other part goes through the slit. The slit width is adjustable using a micrometer screw that ranges from 0 mm up to 5 mm in 100 μm steps. The slit trims the external parts of the incident beam in x-direction. The intensity of the incident beam is Gaussian distributed in the yz-plane. The trimmed parts are the tails of the Gaussian distribution, while the untrimmed part is the almost flat part of the Gaussian distribution. Generally, as a rule of thumb, letting 50% of the incident power to pass results in a beam with a top-hat like intensity-distribution in the z-direction. Now, the trimmed beam has a Gaussian distribution in the z-direction and a Gaussian intensity distribution in the y-direction. Afterwards, the beam passes through a cylinder lens that focuses the beam only in the z-direction, whereas the y-direction is still collimated. A 45° positioned flat mirror redirects the incident beam to move in the vertical plane instead of the horizontal plane. Here, the beam projection is turned from the yz-plane to the xz-plane. Before and after the redirection, the top-hat like intensity distribution stays in the z-direction, while, the Gaussian intensity distribution direction changed from y-direction to the x-direction. Afterwards, a cylindrical 3-lens objective system focuses the incident beam in the x-direction on the substrate/wafer surface plane. The objective lens system consists of 3 cylindrical lenses. The objective lens system is mounted on a micrometer screw to enable processing of samples with various thicknesses. The optically manipulated output beam that falls on the substrate surface has relatively wide Rayleigh length which improves the processing quality even for a rough substrate surface. The flat substrate is then placed on the porous ceramic plate, also called chuck. A vacuum

system sucks the substrates on the chuck. A high resolution magnifying camera allows the precise position of the substrate for a high spatial accuracy processing. Finally, the width w_p of the line-focused laser beam on the substrate's surface is about $12\ \mu\text{m}$ and the length l_p is dependent on the slit width. A programmable computer control system simultaneously operates laser and table, allowing flexible and variable laser processing.

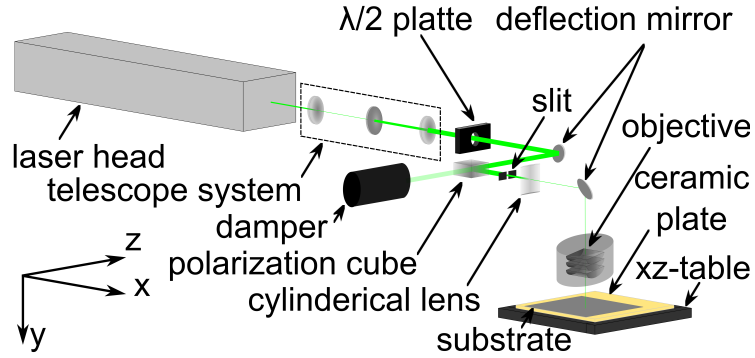


Figure A.1: Scheme of the used laser system in the laser doping process. A Nd:YAG crystal emits a green pulsed laser beam (wavelength $\lambda = 532\ \text{nm}$). A series of optical elements manipulates the beam form during propagation to be line-focused instead of circular-focused. Furthermore, the line-focused beam has a Gaussian Intensity distribution in the short axis and has a tophat intensity distribution in the long axis. A translational table in the xy -plane fixes the substrate/wafer during the laser processing through a porous ceramic plate connected to a vacuum pump. The vacuum pump creates a negative pressure on the plate's surface which fixes the flat substrate placed on it during the processing. Before the processing step, the camera fixed over the table enables the precise positioning of the wafer and allows reaching a high spatial accuracy during the processing.

A.2.2 Laser Power Measurement

Figure A.2 shows a cross sectional scheme of the thermo pile, LM-10, used for laser power measurement. The thermopile surface is coated with materials enhance the absorption of laser with different wavelengths ranging from ultraviolet (UV) range to the visible range. The incident laser beam is absorbed and raises the surface temperature forming a temperature gradient across the sensor. The temperature

gradient induces a voltage signal through the thermoelectric effect. The voltage signal is then recalculated into laser average power P_{avg} . A metal cylindrical body with fins is attached to the surface to protect the operator from the reflected radiation and to prohibit the surrounding diffused light to affect the measurement accuracy. The fins help dissipating the heat transferred from the surface to the metal cylindrical body. The thermopile sensor, LM-10, is capable of measuring laser power starting from 10 mW up to 10W with spectral range $\lambda = 250 \text{ nm}$ to $10.6 \text{ }\mu\text{m}$ and an active area diameter of 16 mm.

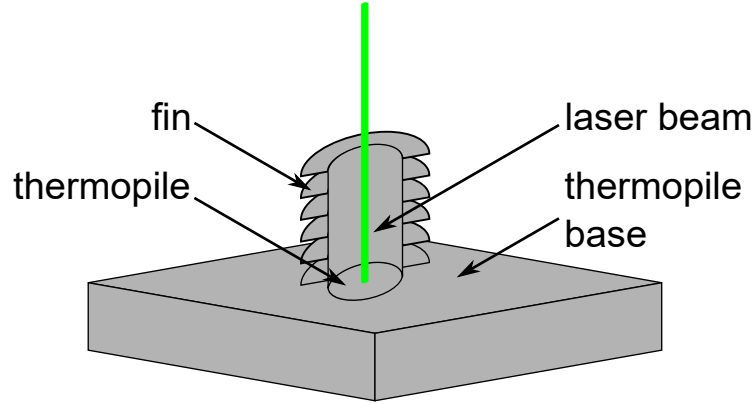


Figure A.2: Cross sectional scheme of the thermopile laser sensor, LM-10, used to measure the laser average power P_{avg} . The incoming laser beam heats up the surface forming a temperature gradient across the sensor. The thermoelectric effect generates a potential difference between the regions with different temperatures. The potential difference is then recalculated into laser power. The fins are to dissipate the heat transferred to the cylindrical wall surrounding the thermopile.

A.2.3 Sputtering

Figure A.3 shows a scheme of the Leybold Univex 600-il, the sputtering machine used for depositing the precursor layer, the dopant source. The machine consists of three main departments: loading station, loading chamber and deposition chamber. A carrier transports and holds the 6-inch wafers inside and outside of the machine and in-between the three department. Two groups of wheels enable the carrier to move on two rails through a mechanical system consisting of a rotating gear coupled in a chain-like trace existing on the bottom side of the carrier. The mechanical sys-

tem controlled by the input recipe moves the carrier to the input positions with the input speed. To load the substrates/6-inch wafers the loading station, the carrier moves to the loading station. The operator place the 6 wafers in the 6 pockets and then runs the recipe. The carrier moves inside the loading chamber at the atmospheric pressure. The inlet valve of the loading chamber closes, and a vacuum pump system evacuates the chamber down to 10^{-6} mbar. The valve between the loading chamber and the deposition chamber opens and the carrier moves inside the deposition chamber and then the valve closes again. The process gas (argon) flows in from the gas inlet beside the targets to increase the chamber pressure. Instantaneously, the pressure reaches the 10^{-2} range to ignite the plasma to onset the sputtering process of the target under which plasma burns. Directly after plasma ignition, the vacuum pump system valve opens to decrease the chamber pressure to the 10^{-3} mbar range. A free sputtering phase occurs during the transition between the two pressures, from 10^{-2} mbar to 10^{-3} mbar. The deposition phase starts as soon as the carrier moves under the ignited plasma. In order to obtain a homogeneous deposited layer, the carrier moves forward and backward under the target to be sputtered in a cyclic form. The starting and ending positions as well as the moving speed of the carrier are given by the recipe. The number of cycles the carrier oscillates under the target to be sputtered, the speed with which the carrier moves as well as the rate with which the target is sputtered defines the deposited film thickness. For a precise monitoring of the deposition process, a number of position sensors are located on the left side of the sputtering machine along its length. The deposition department consists of 5 compartments; the silicon and boron oxide targets are located in the second and fourth compartments, while the other three compartments enable the carrier to fully move outside the main sputtering region (either the second or the fourth compartment). The existence of the other three compartments improves the homogeneity of the deposited layer over the entire length of the carrier/wafers. When the recipe/deposition process ends, the gas flow stops, the generator (RF- and/or DC-generator) turn off, the valve between the deposition and loading chambers open and the carrier moves to the home position in the loading chamber. To get the wafers out, the loading chamber is ventilated and the carrier moves to the loading station, where the operator can take the wafers off.

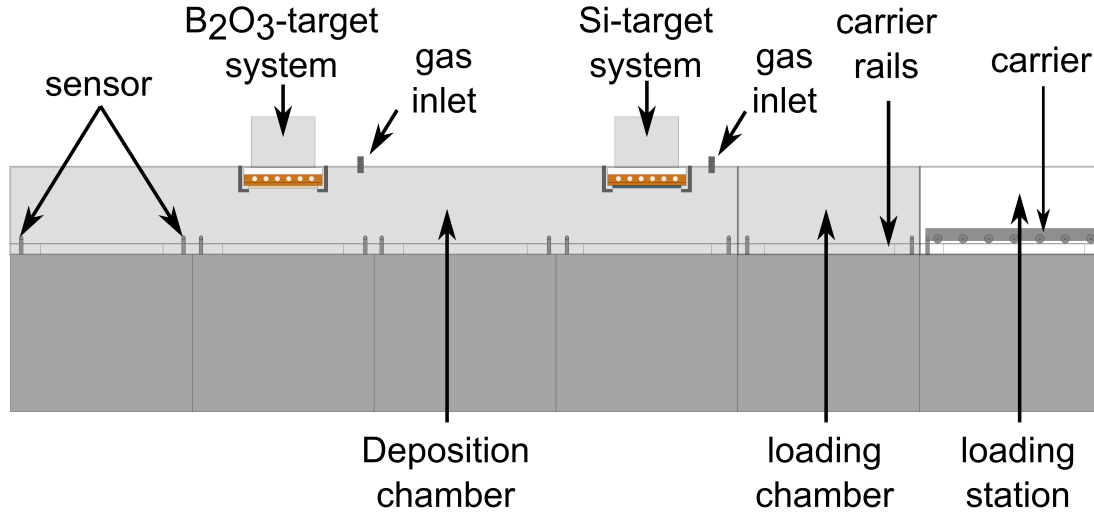


Figure A.3: Scheme of the sputtering machine, Leybold Univex 600-il, used in this work. The machine has 3 main departments: loading station, loading chamber and deposition chamber. The carrier shown in fig. A.5 holds and transports the wafers between the three departments. The carrier has wheels on both sides, the left and the right, and moves on two rails through a mechanical system consisting of a combination a rotating gear coupled in a chain-like trace located on the lower part of the carrier. The loading station is for mounting the 6-inch wafers. The loading chamber is to bring the vacuum level surrounding the carrier down from atmospheric pressure down to about 10^{-6} mbar. Afterwards, the carrier is pulled through the mechanical system into the evacuated deposition chamber (typical base pressure of 2×10^{-7} mbar) for the deposition process. The sensors located on the side of the machine monitor the current location of the carrier for a precise, automatic and safe processing. The deposition chamber consists of 5 compartments, in two of them two targets are mounted. The 5 compartments allow the carrier to enter fully under the ignited target and to move fully out for a homogeneous deposited layer. Beside each target, a gas inlet allows the process gas (argon) to enter the chamber for the beginning of the deposition.

Figure A.4 schematically shows a section of the used sputter gun in the sputtering machine, Leybold Univex 600-il (fig. A.3). The components of the sputter gun are the RF-matching network, the insulating teflon plate, the hollow copper plate and the target material mounted on a conductive plate. The RF-matching network

matches the impedance of the source (RF- or DC-generator) to the impedance of the load (the gas atoms existing between the two electrodes). The matching network/box maximizes the power passed from the source to the load and allows the highest sputtering rate possible at any operating parameter. The thick teflon plate provides the electrical insulation between the cathode and the machine's body. The thick channel-containing copper plate 1 electrically connects the target material with the generator and cools the target material during the sputtering process. The copper plate 2 is the conductive plate over which the target material is mounted. The type of the target material determines the sputtering technique required to sputter it. The non-conductive materials, like boron oxide, requires a RF-sputtering, using the RF-generator. Both, the RF-sputtering technique and the DC-sputtering technique are capable of sputtering the conductive materials like aluminum and the semi-conductive materials, like silicon.

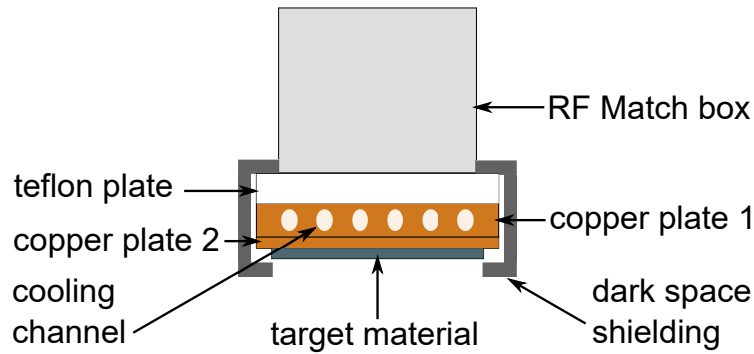


Figure A.4: Scheme of the sputter gun used in the Leybold Univex 600-il sputtering machine (fig. A.3). The upper part of the gun consists of an RF-match box to match the impedance of the source (the RF- or DC-generator) to that of the load (the gas atoms existing between the two electrodes) to allow delivering the maximum power to the load. The insulating thick teflon plate electrically insulates the copper plates from the earthed machine body. The copper plate 1 electrically connects the target material to the generator and has water cooling channels inside of it to dissipate the heat gained by the system. The copper plate 2 is the plate on which the target material is mounted on. The target materials in our case are boron oxide (non-conductive material) and silicon (semi-conductor material). Both RF- and/or DC-sputtering techniques are capable of sputtering silicon, whereas only the RF-sputtering technique is capable of sputtering boron oxide.

Figure A.5 schematically demonstrates the carrier used in the sputtering machine, Leybold Univex 600-il. Six 6-inch pockets are carved in the carrier's surface to hold the wafers during the deposition process. The area of each pocket is $157 \times 157 \text{ mm}^2$, whereas the pockets' depths are 1 mm deep to properly hold the wafer without shading the edges from the sputtered material/s. The left and right corners of the carrier are designated with "L" and "R" letters carved in the carrier's surface, respectively. The moving direction is shown in the figure.

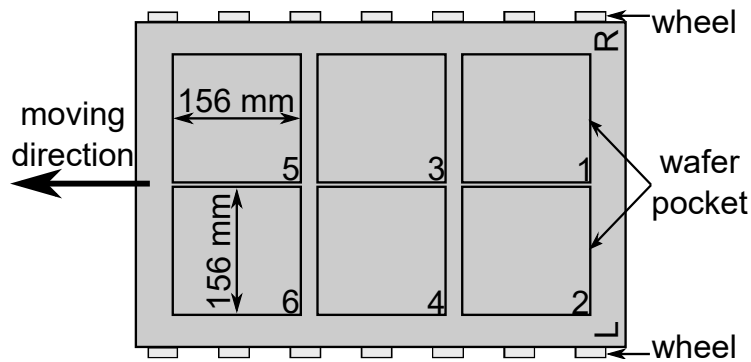


Figure A.5: The carrier over which the six 6-inch wafers are held and transported during the deposition process is schematically shown. Six pockets are carved in the surface of the carrier with each having $157 \times 157 \text{ mm}^2$ area. In the left corner of the carrier, a letter "L" is carved in the surface and so a letter "R" in the left corner.

A.2.4 Secondary Ion Mass Spectroscopy

Secondary ion mass spectroscopy (SIMS) is a well-established micro-analytical technique used to understand the composition of a certain solid substrate. The operation modes of SIMS are static and dynamic. The static SIMS is used mainly for surface analysis, where a primary ion beam with a low ion current density bombards against the surface leading to a spectral emission (surface destruction is lower than 1%) [106]. The dynamic SIMS is substantially used for measuring the trace elements in depth of semiconductors and coatings with a relatively higher detection sensitivity and concentration sensitivity over the other beam techniques [106]. The ability to detect low concentration is referred to as detection sensitivity and the ability to detect concentration difference is referred to as concentration sensitivity. For example, the detection limit of boron in silicon using dynamic SIMS under an

optimum operating conditions varies between 2×10^{13} atoms/cm³ to 10^{14} atoms/cm³ [53]. Further applications of dynamic SIMS are: detecting isotopes, examining of molecular ions and their fragmentation patterns [107] and defining the location of element/molecule with high spatial resolution (accuracy in the micrometer range) [106].

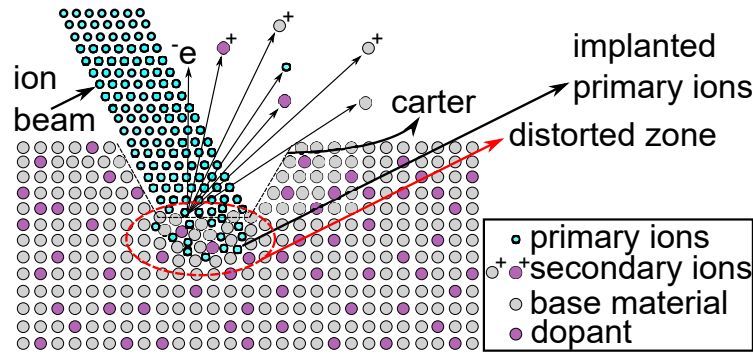


Figure A.6: The principle of the secondary ion mass spectroscopy (SIMS) measurement is schematically represented. A primary ion beam impinges on the surface of the sample with energy ranging from 1 keV up to 20 keV in the case of dynamic SIMS and between 1 keV to 15 keV in case of static SIMS. The bombarding beam unleashes a collision cascade. The reflected energy from the collision cascade releases particles from the surface by breaking the bonding energy. The emitted particles are either neutral atoms/molecules/cluster or ionized atoms/molecules. The mass spectroscopy system detects and analyzes the emitted secondary ions according to their mass to charge ratio m/q .

Figure A.6 demonstrates the working principle of the secondary ion mass spectroscopy (SIMS) measurement. A focused beam of energetically accelerated single-isotope primary ions: normally oxygen (O) or argon (Ar) or cesium (Cs) etc., bombards the substrate's surface releasing a collision cascade. The reflection of the collision cascade is strong enough to break the surface binding energy of some of the surface atoms/molecules. The released surface atoms/molecules are either in the neutral state or in the ionized state. Only the charged particles, in the ionized state, contribute to the mass spectroscopy. The secondary ion emission mechanism is illustrated by three types of sputtering models: kinetic models, surface effect models, and the thermodynamic models [106]. A combination of mass spectrometer or mass

analyzer and detector analyzes the emitted secondary ion species according to their mass to charge ratio m/q .

Figure A.7 schematically represent a typical secondary ion mass spectroscopy (SIMS) device. The main components are the primary ion system consisting of primary ion source, wein filter and x-y deflector and the mass spectroscopy system consisting of ion extractor, mass analyzer and detector. The common species of the primary ion beam are oxygen (O^+), cesium (Cs^+) or argon (Ar^+), neon (Ne^+) etc.. [107]. The generated beam contains many isotopes which need to be filtered through wein filter. The different isotopes of the same material have different masses and thus different velocities. For that reason, to obtain a precise measurement, only one isotope should constitute the primary ion beam. Therefore, the wein filter filters the generated primary ion beam from the unwanted isotopes. The filtered beam is then focused on the substrate's surface through the x-y deflector. The impinging primary ion beam on the substrate's surface dislodge particles from the surface either through the direct collision, slow collision, and thermal sputtering. The ejected particles consists of neutral atoms/molecules/cluster and ionized atoms/molecules. Most of the produced particles are neutral atoms/molecules which do not contribute to the measurement. Only the ionized particles, also called secondary ions, are collected by the ion extractor and being accelerated to a certain energy/velocity. The accelerated ions pass through a magnetic field in the mass analyzer which deflects the flying ions according with the Lorentz force. The radius of deflection is determined by the charge, mass and velocity of the ion and the magnetic field strength. Knowing the magnetic field strength and the velocity of the passing ion, the deflector measures the deflection radius and calculates the mass to charge ratio (m/q). On the display, the measured counts per second per detected m/q ratio of ionized material is displayed.

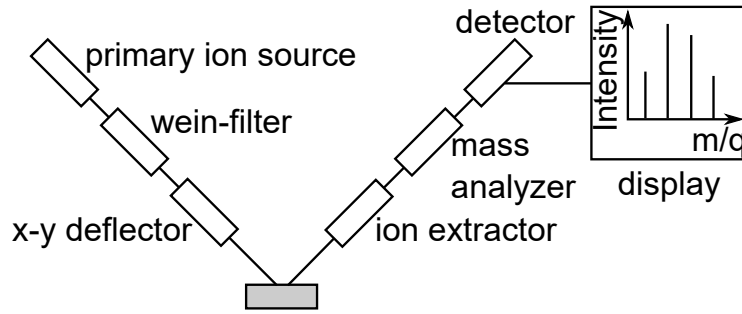


Figure A.7: Scheme of a typical secondary ion mass spectroscopy (SIMS) device with its main components. The primary ion source ejects the primary ion beam which can be either reactive material like oxygen (O) or cesium (Cs) or inert like argon (Ar). The primary ion beam emitted from the source contains many isotopes with different masses and thus with different momenta. For that reason, the wein filter filters the emitted primary ion beam to allow only one isotope to pass through allowing for a precise measurement. The x-y deflector focuses the primary ion beam. The bombardment of the primary ion beam on the substrate's surface causes the emission of secondary ions of the different materials existing in the substrate's surface. The ion extractor accelerates the secondary ions ejected from the surface to a certain velocity. Applying a magnetic field, the mass analyzer analyzes the emitted secondary ions. The detector detects the deflected secondary ion through the magnetic field and measures the signal intensity per ionic species. The display plots the number of count per time per ionic species. The type of ionic species detected is recognized through the mass to ionic charge ratio.

Figure A.8 pictures the SIMS device, Atomika 6500, used in this work. A focused primary oxygen ion beam bombards the substrate's surface, the surface of the silicon wafer, with an incidence angle of 30° and with 10 keV. Under ultra high vacuum conditions, a quadrupole mass spectrometer analyzes the emitted secondary ions from the surface. The sputtering area is $400 \times 400 \mu\text{m}^2$, which is way smaller than a single doping trace area, about $8000 \times 800 \mu\text{m}^2$, to provide the best homogeneity of the doped layer and the highest reachable accuracy of the measured doping profile.

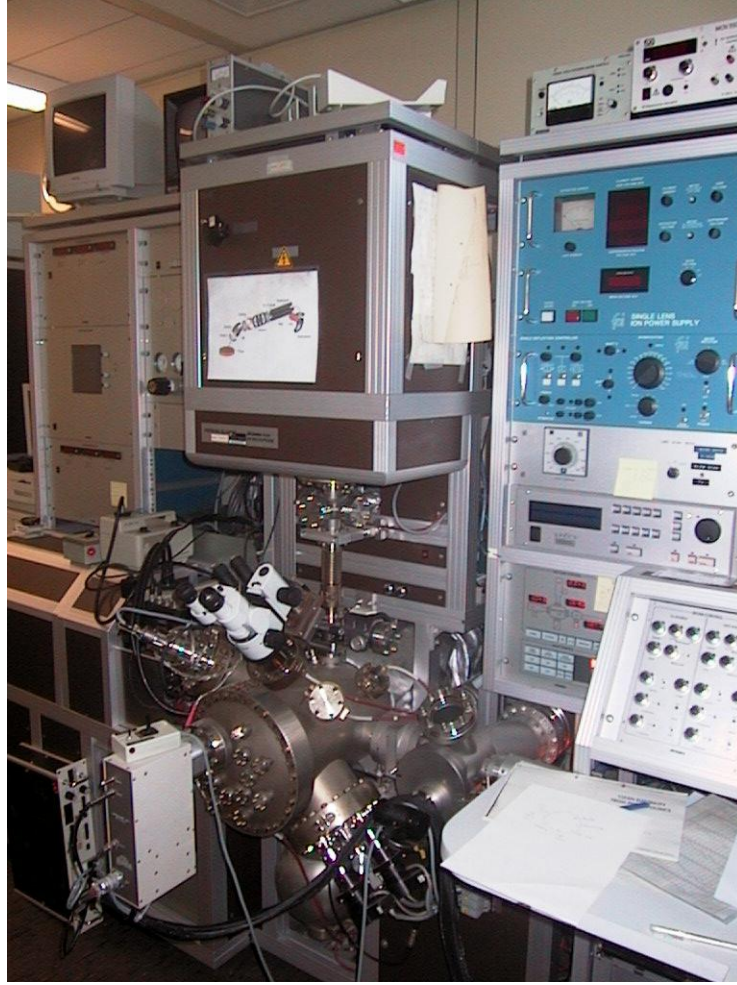


Figure A.8: A picture of the used SIMS device, Atomika 6500, in this work. The device operates under ultra high vacuum (UHV) conditions (1.33×10^{-9} mbar to 1.33×10^{-12} mbar) with two stage vacuum pump systems. The device uses a quadrupole mass spectrometer to analyze the emitted secondary ions.

A.2.5 Laser scanning microscopy

Laser scanning microscope (LSM) is a powerful tool enables not only imaging but also measuring and 3D imaging of the surface morphology. In this work, the 3D laser scanning microscope, keyence VK 9700, is used.

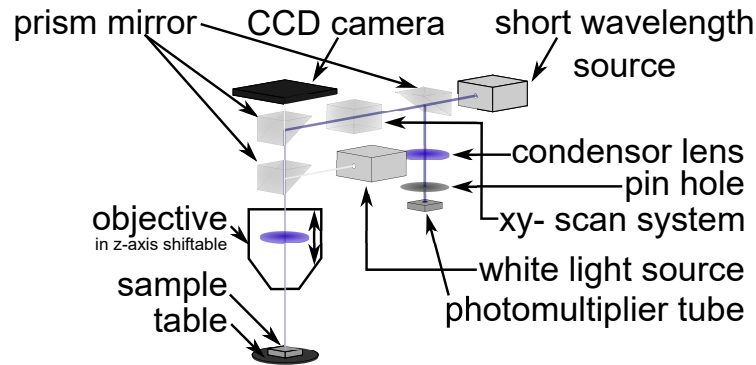


Figure A.9: Schematic representation of the optical system existing in the laser scanning microscope, Keyence VK 9700. In the microscope head exists two beam sources, one for short wavelength (violet laser beam) and the other for white light. The prism mirror divides the beam into two paths. The cube provides the scanning in the x - z plane. The violet laser beam is focused through the objective lens on the sample's surface. For three dimensional scanning, a shifting system shifts the objective lens vertically. The measurement range ranges between the two focal positions at which the system is completely out of focus and in between which the correct focus is included. The scanning technique is shown in figure A.10. The system of condensor lens and pin hole enable getting rid of the blurry effects caused by the reflections from the regions/pixels not lying in the focal plane. The photomultiplier measures the intensity of violet laser reflected from the sample's surface at each objective lens height. The CCD-camera receives the reflected white light beam carrying the color information. The system is then analyzed using a powerful software to visualize the captured region.

Figure A.9 shows schematically the optical system existing in the used laser scanning microscope, Keyence VK 9700. The main components of the optical system are the beam sources, the prism mirrors and the cube system. The charged-coupled device (CCD) camera and the photomultiplier are for the interpretation of the reflected beams. Two beams are generated from the beam sources, the violet laser beam and the white light beam. The reflected white light beam provides color information about the surface. The prism mirrors are semi-transparent allowing for the half of the emitted beam to propagate in the propagation direction, whereas the other half in the perpendicular direction. The reflected violet laser beam scans the sample for three dimensional imaging as it provides height information. The

cube allows the violet laser beam to scan in the x-z plane while the objective lens movement in the y-direction enables the three dimensional imaging. The reflected violet laser beam is condensed (collimated or converged), filtered and increased in quality using the condensator lens and the pin hole system. The photomultiplier receives the reflected beam and analyzes the intensity.

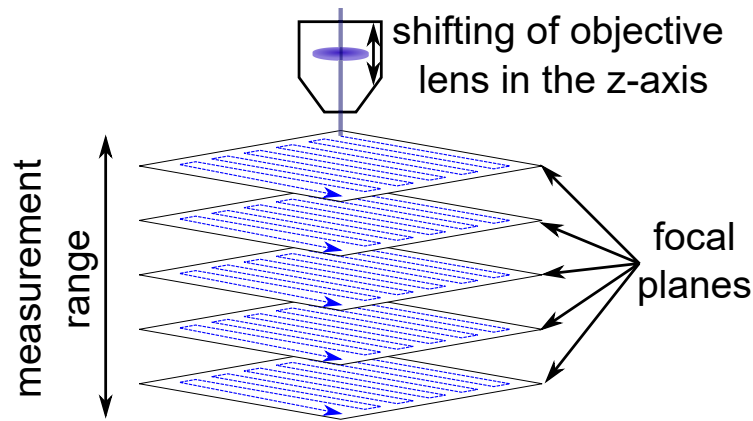


Figure A.10: Schematic representation of the depth scanning technique by the laser scanning microscope, Keyence VK 9700. The movement of the objective lens in the y-axis enables the shifting of the focal plane vertically, and thus grasping rough structures, non-zero depth structures. The condensor lens focuses the incident reflected violet laser to then be chopped with the pin hole to allow only image reflected from the position to be scanned in the x-z plane to pass through. The photomultiplier receives the reflected violet laser beam, analyzes the intensities. The points at which the captured intensity the highest are those lying in the focal plane at that particular moment. As the scanning proceed, the software records the readings of the CCD-camera and the photomultiplier to construct the three dimensional image of the investigated surface.

Figure A.10 describes schematically the 3D imaging process. The cube shifts the violet laser beam in the x-z plane over the sample's surface. At each scanning point in the x-z plane, the objective lens is shifted in the y-axis between the two foci planes in between which no detectable image occurs. The two foci planes are the two extremes, upwards and downwards, away from the correct focus position. Shifting the objective lens vertically changes the focal plane accordingly vertically, and thus, receiving at each focal plane, the levels of the surface with the highest reflected laser

intensities. The reflected violet laser beam is received by a photomultiplier. As the scanning technique proceeds, the software records pixels of the highest intensity occurred at each focal plane with the height at which it is observed. Combining these information, the 3D imaging is grasped [108].

A.2.6 Profilometer

Profilometer is a very useful tool not only for measuring the film thicknesses but also surface roughness and surface microstructures for a variety of materials and samples. For that reason, the profilometer had found its way to a wide range of industrial applications like semiconductor, automotive, aerospace and medical applications. The modern profilometers, like the device used in this work, Dektak XT, is capable of measuring film thicknesses with reproducibility $<0.03\%$ [109]. The modern Dektak XT is produced by Bruker corporation.

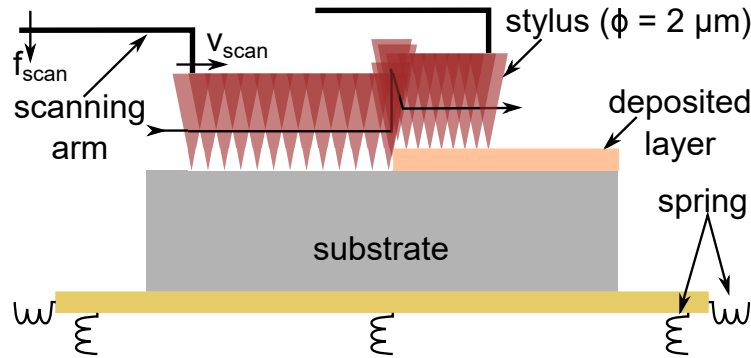


Figure A.11: Schematic representation of the film thickness measurement conducted by the profilometer "Dektak XT" in this work. A sample with a well polished back and front sides with the front surface covered with a hard material is placed on the spring supported measuring stage. The deposited film on the flat surface should have a step in it to enable the measuring of its thickness. A stylus, with head diameter equals $2 \mu\text{m}$, scans across the step made in the deposited hard film. The force f_{scan} and the speed V_{scan} of the moving stylus determines the accuracy and the validity of the measurement. The force f_{scan} should not be high enough to scratch the surface. The rule of the springs connected to the stage is to compensate for any slight vibrational motion happened in the surrounding, and thus, allowing for such high accuracy and measurement reproducibility.

Figure A.11 schematically shows the film thickness measurement technique used in this work. For that, the profilometer "Dektak XT" is used. The device consists of a stage with springs connected to it. The springs compensate for any vibration coming from the surrounding environment. The scanning arm is connected to a diamond stylus with a head diameter equals $2\text{ }\mu\text{m}$. The sample should be flat with both sides polished to enable the lowest noise and allow for the highest measurement precision. The film covering the flat surface should contain a step or an edge over which the stylus can move and record the height. For the measurement, the clean surface is placed on the clean flat spring-supported stage. The stylus scan afterwards across the edge or the step in the deposited film. The level of the stylus is being logged in the software and is being plotted in real time on the display.

List of Figures

2.1	Schematical representation of the cross-section of the IBC solar cell developed in <i>ipv</i>	10
2.2	Scheme of a doped square-like area in an undoped silicon wafer	14
2.3	Scheme of the RF-sputtering deposition chamber	16
2.4	Scheme of a typical laser processing machine	17
2.5	Laser beam propagation	18
2.6	Scheme of the doping process	21
3.1	Laser beam dimensions and doping technique	24
3.2	Scheme of pulse-pulse overlap in x- and z-directions	25
3.3	Scheme of the four-point probe sheet resistance measurement device .	26
4.1	Scheme of a small nodal network with one interior node	31
4.2	The volume disrectization used in the model	34
4.3	Scheme of the matrix carrying the x-dimensions of the studied volume	35
4.4	Scheme of the matrix carrying the y-dimensions of the studied volume	36
4.5	Scheme of the matrix carrying the properties of the cells in the studied volume	36
4.6	The inter-nodal spacing between two neighboring nodes at the borders of two different mesh regions	40
4.7	The fit formula for predicting the pulse duration as a function in the pulse energy density	41
4.8	The photodetector voltage signals for the emitted laser pulse at $H = 0.75 \text{ J/cm}^2$ and $H = 4.25 \text{ J/cm}^2$	42
4.9	Scheme of the temporal and the spatial intensity distribution of the laser pulse	43

4.10	Signifying the three laser doping regimes	47
4.11	Investigating the temperature-time curve against the temporal pulse form	49
4.12	Scheme of the experiment used to investigate the surface morphology	50
4.13	The measured surface deformation resulting from laser irradiation using laser scanning microscope	52
4.14	Validation of the calculated melt width	54
4.15	Validation of the calculated melt depth	56
4.16	Scheme of different phases with which the mesh network passes through the irradiation duration	58
4.17	Scheme of the experiment used for measuring the doping profiles with SIMS	60
4.18	Validation of the calculated doping profile for low pulse energy densities	61
4.19	Validation of the calculated doping profile for high pulse energy densities	62
4.20	Finding the correct reduced surface reflection with the help of fig. 4.13	67
4.21	Finding the correct surface reflectance of the melted silicon surface that fits the measured doping profile	68
4.22	Finding the correct recondensation percentage that fits the measured doping profile	70
4.23	Finding the correct pre-exponential factor value that gives the best fit for the measured doping profile	71
4.24	A visualization of the temperature distribution in the melted pool . .	73
4.25	Scheme of the half melt pool approximated to the nearest geometrical shape	74
5.1	Scheme of the laser doping process using different pulse to pulse dis- tance x_{irr}	79
5.3	Schematical representation of the experiment conducted for finding the dependence of sheet conductance G_{sh} on intersection depth d_{ch} . .	82
5.4	Measured sheet conductance variation with the used pulse to pulse distance x_{irr} for doping	84

5.5	A cross sectional concentration map of the laser doped layer using varied inter-pulse distance x_{irr} : a) $x_{\text{irr}} = 1 \mu\text{m}$, b) $x_{\text{irr}} = 3 \mu\text{m}$, c) $x_{\text{irr}} = 5 \mu\text{m}$, d) $x_{\text{irr}} = 7 \mu\text{m}$, e) $x_{\text{irr}} = 9 \mu\text{m}$. The colored region is the doped region, whereas the grey region is the undoped silicon with base doping of 10^{16} cm^{-3} . For each layer, the doping profile is the laterally averaged concentration over the hashed area. The three depth $d_{\text{pn,ch}}$, $d_{\text{pn,lat}}$ and $d_{\text{pn,max}}$ correspond to the pn-junction depth in the melted channel region, the pn-junction depth resulted from the laterally averaged doping profiles (shown in fig. 5.6) and the maximum pn-junction depth respectively.	86
5.6	Simulated doping profiles for a doped layer using different pulse to pulse distance x_{irr}	87
5.7	Simulated doses as a function of integration depth	88
5.8	A representation of all simulated depths of interest	89
5.9	Simulated dopant doses $D_{\text{B,full}}$ versus measured doses $D_{\text{B,act}}$	91
5.10	Intersection depth d_{ch} dependence on the used pulse to pulse distance x_{irr}	92
5.11	Validation of the sheet conductance G_{sh} equation	95
A.1	Scheme of the laser processing machine used in this work	103
A.2	Cross sectional scheme of the thermopile laser sensor	104
A.3	Scheme of the sputtering system used in this work	106
A.4	Scheme of the sputter gun used in the sputtering system	107
A.5	Wafers' Carrier during the precursor deposition process	108
A.6	The principle of the secondary ion mass spectroscopy measurement	109
A.7	Scheme of a typical secondary ion mass spectroscopy (SIMS) device with its main components	111
A.8	A picture of the used SIMS device	112
A.9	Scheme of the laser scanning microscope internal system	113
A.10	Scheme of the laser scanning microscope working principle	114
A.11	Scheme of the profilometer working concept	115

List of Tables

A.1	Properties of crystalline silicon	100
A.2	Properties of precursor layer	100
A.3	Material properties data of boron oxide B_2O_3	101

Bibliography

- [1] C. Kemfert, W.-P. Schill, and T. Traber, “Energiewende in deutschland-chancen und herausforderungen,” *Vierteljahrshefte zur Wirtschaftsforschung*, vol. 82, no. 3, pp. 5–9, 2013.
- [2] “Communication from the commission to the european parliament, the council, the european economic and social committee and the committee of the regions, a roadmap for moving to a competitive low carbon economy in 2050,” 2011.
- [3] M. da Graça Carvalho, “Eu energy and climate change strategy,” *Energy*, vol. 40, no. 1, pp. 19–22, 2012.
- [4] “Renewables 2019: Analysis and forecast to 2024,” International Energy Agency, Report P-191, 2019.
- [5] “Photovoltaics report,” Fraunhofer ISE, Report, Feb. 2023.
- [6] M. Dahlinger and K. Carstens, “Optimized laser doped back surface field for ibc solar cells,” *Energy Procedia*, vol. 92, pp. 450–456, 2016.
- [7] M. Dahlinger, K. Carstens, E. Hoffmann, R. Zapf-Gottwick, and J. H. Werner, “23.2% laser processed back contact solar cell: fabrication, characterization and modeling,” *Progress in Photovoltaics: Research and Applications*, vol. 25, no. 2, pp. 192–200, 2017. [Online]. Available: <https://onlinelibrary.wiley.com/doi/abs/10.1002/pip.2854>
- [8] K. Carstens, M. Dahlinger, E. Hoffmann, J. R. Köhler, R. Zapf-Gottwick, and J. H. Werner, “Universal passivation for p++ and n++ areas on ibc solar cells,” *Energy Procedia*, vol. 77, pp. 779–785, 2015.

-
- [9] M. Dahlinger and K. Carstens, "Band gap narrowing models tested on low recombination phosphorus laser doped silicon," *Journal of Applied Physics*, vol. 120, no. 15, p. 155701, 2016.
- [10] K. Carstens, M. Dahlinger, E. Hoffmann, R. Zapf-Gottwick, and J. H. Werner, "Amorphous silicon passivation for 23.3% laser processed back contact solar cells," *Japanese Journal of Applied Physics*, vol. 56, no. 8S2, p. 08MB20, 2017.
- [11] K. Ohmer, Y. Weng, J. R. Köhler, H. P. Strunk, and J. H. Werner, "Defect formation in silicon during laser doping," *IEEE Journal of Photovoltaics*, vol. 1, no. 2, pp. 183–186, 2011.
- [12] S. Eisele, T. C. Röder, J. R. Köhler, and J. H. Werner, "18.9% efficient full area laser doped silicon solar cell," *Applied Physics Letters*, vol. 95, no. 13, p. 133501, 2009.
- [13] F. Cristiano, M. Shayesteh, R. Duffy, K. Huet, F. Mazzamuto, Y. Qiu, M. Quillec, H. Henrichsen, P. Nielsen, D. H. Petersen *et al.*, "Defect evolution and dopant activation in laser annealed si and ge," *Materials Science in Semiconductor Processing*, vol. 42, pp. 188–195, 2016.
- [14] J. Köhler, M. Ametowobla, and A. Esturo-Bretón, "Numerical modelling of pulsed laser doping of crystalline silicon solar cells," in *Proc. 20th European Photovoltaic Solar Energy Conference*, 2005, pp. 1162–1165.
- [15] S. V. Patankar, *Numerical heat transfer and fluid flow*. CRC press, 2018.
- [16] J. Thomas, *Silicon*. Marshall Cavendish, 2002.
- [17] Q. Tang, H. Yao, B. Xu, and J. Ge, "Enhanced energy conversion efficiency of al-bsf c-si solar cell by a novel hierarchical structure composed of inverted pyramids with different sizes," *Solar Energy*, vol. 208, pp. 1–9, 2020. [Online]. Available: <https://www.sciencedirect.com/science/article/pii/S0038092X20308057>
- [18] Y. Lv, Y. Zhuang, W. Wang, W. Wei, J. Sheng, S. Zhang, and W. Shen, "Towards high-efficiency industrial p-type mono-like si perc solar cells," *Solar Energy Materials and Solar Cells*, vol. 204, p. 110202,
-

2020. [Online]. Available: <https://www.sciencedirect.com/science/article/pii/S0927024819305318>
- [19] L. Hamann, L. Proenneke, M. Reuter, and J. H. Werner, "Colored ribbons achieve +0.3% abs module efficiency gain," in *The 22nd international photovoltaic science and engineering conference*, 2012.
- [20] L. Hamann, L. Prönneke, and J. H. Werner, "Colored ribbons achieve +0.28%_{abs.} efficiency gain," *IEEE Journal of Photovoltaics*, vol. 2, no. 4, pp. 494–498, 2012.
- [21] E. V. Kerschaver and G. Beaucarne, "Back-contact solar cells: a review," *Progress in Photovoltaics: Research and Applications*, vol. 14, no. 2, pp. 107–123, 2006. [Online]. Available: <https://onlinelibrary.wiley.com/doi/abs/10.1002/pip.657>
- [22] M. Dahlinger, B. Bazer-Bachi, T. C. Röder, J. R. Köhler, R. Zapf-Gottwick, and J. H. Werner, "Laser-doped back-contact solar cells," *IEEE Journal of Photovoltaics*, vol. 5, no. 3, pp. 812–818, 2015.
- [23] M. Dahlinger, "Laserprozessierte rückkontakt-solarzellen aus silizium," Ph.D. dissertation, Universität Stuttgart, Stuttgart, 2017.
- [24] T. Röder, A. Esturo-Breton, S. Eisele, C. Wagner, J. Kohler, and J. Werner, "Fill factor loss of laser doped textured silicon solar cells," *23rd European Photovoltaic Solar Energy Conference*, 1-5 September 2008.
- [25] M. Dahlinger, S. Eisele, J. Köhler, and J. Werner, "Laser doped boron emitters with sputtered precursor," *26th European Photovoltaic Solar Energy Conference and Exhibition*, pp. 1152 – 1154, 09 2011.
- [26] M. Dahlinger, B. Bazer-Bachi, T. C. Röder, J. R. Köhler, R. Zapf-Gottwick, and J. H. Werner, "22.0% efficient laser doped back contact solar cells," *Energy Procedia*, vol. 38, pp. 250–253, 2013.
- [27] M. Dahlinger, K. Carstens, J. R. Köhler, R. Zapf-Gottwick, and J. H. Werner, "Laser doped screen-printed back contact solar cells exceeding 21% efficiency," *Energy Procedia*, vol. 55, pp. 410–415, 2014.
-

-
- [28] Z. Hameiri, T. Puzzer, L. Mai, A. Sproul, and S. Wenham, “Laser induced defects in laser doped solar cells,” *Progress in Photovoltaics: Research and Applications*, vol. 19, no. 4, pp. 391–405, 2011.
- [29] W. Kern, “Cleaning solution based on hydrogen peroxide for use in silicon semiconductor technology,” *RCA review*, vol. 31, pp. 187–205, 1970.
- [30] K. Carstens, “Passivierung kristalliner silizium-solarzellen mit amorphem silizium,” Ph.D. dissertation, Universität Stuttgart, Stuttgart, 2017.
- [31] J. Lambert and M. Reese, “The gettering of gold and copper from silicon,” *Solid-State Electronics*, vol. 11, no. 11, pp. 1055–1061, 1968.
- [32] A. Bentzen, A. Holt, R. Kopecek, G. Stokkan, J. S. Christensen, and B. G. Svensson, “Gettering of transition metal impurities during phosphorus emitter diffusion in multicrystalline silicon solar cell processing,” *Journal of Applied Physics*, vol. 99, no. 9, p. 093509, 2006. [Online]. Available: <https://doi.org/10.1063/1.2194387>
- [33] M. B. Shabani, T. Yamashita, and E. Morita, “Metallic impurities in mono and multi-crystalline silicon and their gettering by phosphorus diffusion,” *ECS Transactions*, vol. 16, no. 6, p. 179, 2008.
- [34] K. Carstens and M. Dahlinger, “Surface passivation of heavily boron or phosphorus doped crystalline silicon utilizing amorphous silicon,” *Journal of Applied Physics*, vol. 119, no. 18, p. 185303, 2016.
- [35] F. Haase, S. Kajari-Schröder, U. Römer, T. Neubert, J.-H. Petermann, R. Peibst, N.-P. Harder, and R. Brendel, “Increased front surface recombination by rear-side laser processing on thin silicon solar cells,” *IEEE Journal of Photovoltaics*, vol. 3, no. 3, pp. 976–984, 2013.
- [36] D. B. M. Klaassen, “A unified mobility model for device simulation—i. model equations and concentration dependence,” *Solid-State Electronics*, vol. 35, no. 7, pp. 953–959, 1992.
- [37] D. Klaassen, “A unified mobility model for device simulation—ii. temperature dependence of carrier mobility and lifetime,” *Solid-State Electronics*, vol. 35, no. 7, pp. 961–967, 1992.
-

-
- [38] R. V. Stuart, *Vacuum Technology, Thin Films, and Sputtering - An Introduction*. Amsterdam, Boston: Academic Press, 2012.
- [39] R. Behrisch, *Sputtering by Particle Bombardment I - Physical Sputtering of Single-Element Solids*. Wiesbaden: Springer Berlin Heidelberg, 2014.
- [40] K. Wasa, I. Kanno, and H. Kotera, *Handbook of Sputter Deposition Technology - Fundamentals and Applications for Functional Thin Films, Nano-Materials and MEMS*. Zagreb: William Andrew, 2012.
- [41] H. Hügel and T. Graf, *Laser in der Fertigung - Grundlagen der Strahlquellen, Systeme, Fertigungsverfahren*. Wiesbaden: Springer Fachmedien Wiesbaden, 2014.
- [42] P. Penchev, S. Dimov, D. Bhaduri, S. Soo, and B. Crickboom, “Generic software tool for counteracting the dynamics effects of optical beam delivery systems,” *Proceedings of the Institution of Mechanical Engineers, Part B: Journal of Engineering Manufacture*, vol. 231, 02 2015.
- [43] R. K. Willardson and A. C. Beer, *Semiconductors and Semimetals - Pulsed laser processing of semiconductors/ volume editors R.F. Wood, C.W. White, R.T. Young*. Amsterdam, Boston: Academic Press, 1984.
- [44] W. Steen and J. Mazumder, *Laser Material Processing*. London: Springer London, 2010.
- [45] T. Graf, *Laser - Grundlagen der Laserstrahlerzeugung*. Wiesbaden: Springer Fachmedien Wiesbaden, 2015.
- [46] C. T. Dawes, *Laser Welding - A Practical Guide*. Cambridge: Woodhead Publishing, 1992.
- [47] T. Deutsch, D. Ehrlich, R. Osgood Jr, and Z. Liao, “Ohmic contact formation on inp by pulsed laser photochemical doping,” *Applied Physics Letters*, vol. 36, no. 10, pp. 847–849, 1980.
- [48] D. Ehrlich, R. Osgood Jr, and T. Deutsch, “Direct writing of regions of high doping on semiconductors by uv-laser photodeposition,” *Applied Physics Letters*, vol. 36, no. 11, pp. 916–918, 1980.
-

- [49] A. Esturo-Bretón, T. A. Wagner, J. R. Köhler, and J. H. Werner, “Laser doping for crystalline silicon solar cell emitters,” in *13th Workshop on Crystalline Silicon Solar Cell Materials and Processes*, 2003, p. 186.
 - [50] F. C. Campbell, *Elements of Metallurgy and Engineering Alloys* -. Russell Township, Ohio: ASM International, 2008.
 - [51] J. Mayer, “Ion implantation in semiconductors,” in *1973 International Electron Devices Meeting*, 1973, pp. 3–5.
 - [52] F. Chernow, *Ion Implantation in Semiconductors 1976* -. Berlin Heidelberg: Springer Science & Business Media, 2012.
 - [53] D. K. Schroder, *Semiconductor Material and Device Characterization* -. New York: John Wiley & Sons, 2015.
 - [54] M. Berti, L. D. Dalle Rose, A. Drigo, C. Cohen, J. Siejka, G. Bentini, and E. Jannitti, “Matrix atomic losses and oxygen incorporation under ruby-laser irradiation of silicon in gaseous atmospheres,” *Physical Review B*, vol. 34, no. 4, p. 2346, 1986.
 - [55] G. Bentini, M. Bianconi, and C. Summonte, “Surface doping of semiconductors by pulsed-laser irradiation in reactive atmosphere,” *Applied Physics A*, vol. 45, no. 4, pp. 317–324, 1988.
 - [56] S. De Unamuno and E. Fogarassy, “A thermal description of the melting of c-and a-silicon under pulsed excimer lasers,” *Applied Surface Science*, vol. 36, no. 1-4, pp. 1–11, 1989.
 - [57] S. Matsumoto, S. Yoshioka, J. Wada, S. Inui, and K. Uwasawa, “Boron doping of silicon by arf excimer laser irradiation in b2h6,” *Journal of Applied Physics*, vol. 67, no. 12, pp. 7204–7210, 1990.
 - [58] S. Inui, T. Nii, and S. Matsumoto, “Precise control of sheet resistance in boron doping of silicon by excimer laser irradiation,” *IEEE electron device letters*, vol. 12, no. 12, pp. 702–703, 1991.
 - [59] R. F. Wood, G. A. Geist, and C. L. Liu, “Two-dimensional modeling of pulsed-laser irradiated a-si and other materials,” *Phys. Rev. B*,
-

- vol. 53, pp. 15 863–15 870, Jun 1996. [Online]. Available: <https://link.aps.org/doi/10.1103/PhysRevB.53.15863>
- [60] M. Hernandez, J. Venturini, D. Zahorski, J. Boulmer, D. Débarre, G. Kerrien, T. Sarnet, C. Laviro, M. Semeria, D. Camel *et al.*, “Laser thermal processing for ultra shallow junction formation: numerical simulation and comparison with experiments,” *Applied Surface Science*, vol. 208, pp. 345–351, 2003.
- [61] J. Köhler, M. Ametowobla, and A. Esturo-Bretón, “Numerical modelling of pulsed laser doping of crystalline silicon solar cells,” in *Proc. 20th European Photovoltaic Solar Energy Conference*, 2005, pp. 1162–1165.
- [62] J. R. Köhler and S. J. Eisele, “Phosphorus out-diffusion in laser molten silicon,” *Journal of Applied Physics*, vol. 117, no. 14, p. 145701, 2015. [Online]. Available: <https://doi.org/10.1063/1.4917048>
- [63] T. Li, C. Zhou, Z. Liu, L. Zhao, H. Li, H. Diao, and W. Wang, “Calculated and experimental research of sheet resistances of crystalline silicon solar cells by dry laser doping,” in *2011 International Conference on Electrical and Control Engineering*. IEEE, 2011, pp. 5777–5779.
- [64] P. C. Lill, M. Dahlinger, and J. R. Köhler, “Boron partitioning coefficient above unity in laser crystallized silicon,” *Materials*, vol. 10, no. 2, p. 189, 2017.
- [65] A. Fell, “Modelling and simulation of laser chemical processing (lcp) for the manufacturing of silicon solar cells,” Ph.D. dissertation, Universität Konstanz, Konstanz, 2010.
- [66] M. Diez, *Pulsformung zur schädigungsarmen Laserbearbeitung von Silizium* -. München: Herbert Utz Verlag, 2010.
- [67] S. Patankar, *Numerical Heat Transfer and Fluid Flow* -. Justus-Liebig-Universität Gießen: Taylor & Francis, 2018.
- [68] X. Zhang, J. Ho, and C. Grigoropoulos, “Ultra-shallow p+-junction formation in silicon by excimer laser doping: a heat and mass transfer perspective,” *International Journal of Heat and Mass Transfer*, vol. 39, no. 18, pp. 3835–3844, 1996.
-

- [69] F. K. Courant, R. and H. Lewy, “Über die partiellen differenzengleichungen der mathematischen physik,” *Mathematische Annalen*, vol. 100, no. 1432-1807, p. 32–74, 1928. [Online]. Available: <https://doi.org/10.1007/BF01448839>
 - [70] J. I. Pankove, *Optical Processes in Semiconductors* -. New York: Courier Corporation, 2012.
 - [71] E. Hecht, *Optics, Global Edition*, 5th ed. Harlow: Pearson Education Limited, 2016.
 - [72] S. M. Sze, *Semiconductor Devices - Physics and Technology*. John Wiley & Sons Singapore Pte. Limited, 2012.
 - [73] M. J. Deen and P. K. Basu, *Silicon Photonics - Fundamentals and Devices*. New York: John Wiley & Sons, 2012.
 - [74] M. A. Green, “Self-consistent optical parameters of intrinsic silicon at 300k including temperature coefficients,” *Solar Energy Materials and Solar Cells*, vol. 92, no. 11, pp. 1305 – 1310, 2008. [Online]. Available: <http://www.sciencedirect.com/science/article/pii/S0927024808002158>
 - [75] R. Dassow, *Laserkristallisation von Silicium*, dissertation ed. Universität Stuttgart, 2001.
 - [76] M. Balarin, “Properties of silicon. emis datareviews series no. 4. einföhrung: C. hilsum, vorwort: T. h. ning, inspec, the institution of electrical engineering, london, new york 1988, 31 kapitel, 1100 seiten, 260 datareviews, £ 195, isbn 0-85296-4757,” *Crystal Research and Technology*, vol. 24, no. 4, p. 386–386, 1989.
 - [77] M. S. K. Fuchs, “Optical properties of liquid silicon: the integral equation approach,” *Journal of Physics: Condensed Matter*, vol. 12, no. 19, pp. 4341–4351, may 2000. [Online]. Available: <https://doi.org/10.1088/0953-8984/12/19/305>
 - [78] P. Patnaik, *Handbook of Inorganic Chemicals* -. New York: McGraw-Hill, 2003.
-

-
- [79] D. R. Lide, *CRC Handbook of Chemistry and Physics - A Ready-reference Book of Chemical and Physical Data*. Boca Raton, Fla: CRC Press, 1995.
- [80] E. Kannatey-Asibu Jr, *Principles of Laser Materials Processing*. John Wiley & Sons, 2009, vol. 4.
- [81] T. Menold, M. Ametowobla, J. R. Köhler, and J. H. Werner, "Surface patterning of monocrystalline silicon induced by spot laser melting," *Journal of Applied Physics*, vol. 124, no. 16, p. 163104, 2018. [Online]. Available: <https://doi.org/10.1063/1.5049781>
- [82] M. Hassan, M. Dahlinger, J. R. Köhler, R. Zapf-Gottwick, and J. H. Werner, "Unified model for laser doping of silicon from precursors," *Materials*, vol. 14, no. 9, p. 2322, 2021.
- [83] R. K. Endo, Y. Fujihara, and M. Susa, "Calculation of the density and heat capacity of silicon by molecular dynamics simulation," *High Temperatures-High Pressures*, vol. 35/36, no. 5, p. 505–511, 2003.
- [84] H. Ki, J. Mazumder, and P. S. Mohanty, "Modeling of laser keyhole welding: Part i. mathematical modeling, numerical methodology, role of recoil pressure, multiple reflections, and free surface evolution," *Metallurgical and Materials Transactions A*, vol. 33, no. 6, pp. 1817–1830, 2002.
- [85] P. C. Setze and NACA, *A review of the physical and thermodynamic properties of boric oxide*. Washington, D.C. : National Advisory Committee for Aeronautics, 1957.
- [86] P. Patnaik, *Handbook of inorganic chemicals*. McGraw-Hill, 2003.
- [87] E. P. Donovan, F. Spaepen, D. Turnbull, J. M. Poate, and D. C. Jacobson, "Heat of crystallization and melting point of amorphous silicon," *Applied Physics Letters*, vol. 42, no. 8, pp. 698–700, 1983. [Online]. Available: <https://doi.org/10.1063/1.94077>
- [88] M. Becker, *Heat Transfer - A Modern Approach*. Springer Science & Business Media:Berlin Heidelberg, 2012.
-

-
- [89] K. Kadoya, N. Matsunaga, and A. Nagashima, "Viscosity and thermal conductivity of dry air in the gaseous phase," *Journal of Physical and Chemical Reference Data*, vol. 14, no. 4, pp. 947–970, 1985. [Online]. Available: <https://doi.org/10.1063/1.555744>
- [90] H. Kobatake, H. Fukuyama, I. Minato, T. Tsukada, and S. Awaji, "Noncontact measurement of thermal conductivity of liquid silicon in a static magnetic field," *Applied Physics Letters*, vol. 90, no. 9, p. 094102, 2007. [Online]. Available: <https://doi.org/10.1063/1.2710220>
- [91] Z. Li, X. Wang, Z. Shen, J. Lu, and X. Ni, "Numerical simulation of millisecond laser-induced damage in silicon-based positive-intrinsic-negative photodiode," *Appl. Opt.*, vol. 51, no. 14, pp. 2759–2766, May 2012. [Online]. Available: <http://ao.osa.org/abstract.cfm?URI=ao-51-14-2759>
- [92] R. Swanepoel, "Determination of the thickness and optical constants of amorphous silicon," *Journal of Physics E: Scientific Instruments*, vol. 16, no. 12, p. 1214, 1983.
- [93] P. A. Stolk, A. Polman, and W. C. Sinke, "Experimental test of kinetic theories for heterogeneous freezing in silicon," *Phys. Rev. B*, vol. 47, pp. 5–13, Jan 1993. [Online]. Available: <https://link.aps.org/doi/10.1103/PhysRevB.47.5>
- [94] R. E. Kirk, *Encyclopedia of Chemical Technology. Vol 4 -*. Interscience Encyclopedia Incorporated, 1949.
- [95] *Thermophysical Properties of Matter - the TPRC Data Series. Volume 5. Specific Heat - Nonmetallic Solids -*. New York: Defense Technical Information Center.
- [96] J. Ning, L.-J. Zhang, X. qing Yin, J.-X. Zhang, and S.-J. Na, "Mechanism study on the effects of power modulation on energy coupling efficiency in infrared laser welding of highly-reflective materials," *Materials & Design*, vol. 178, p. 107871, 2019. [Online]. Available: <http://www.sciencedirect.com/science/article/pii/S0264127519303090>
- [97] H. Sasaki, E. Tokizaki, K. Terashima, and S. Kimura, "Density measurement of molten silicon by an improved archimedian method," *Journal of Crystal*
-

- Growth*, vol. 139, no. 3, pp. 225 – 230, 1994. [Online]. Available: <http://www.sciencedirect.com/science/article/pii/0022024894901708>
- [98] T. E. T. K. Sasaki, H. and S. Kimura, “Density variations in molten silicon dependent on its thermal history,” *Japanese Journal of Applied Physics*, vol. 33, no. 11R, p. 6078, 1994.
- [99] K. Tang, E. J. Øvrelid, G. Tranell, and M. Tangstad, “Critical assessment of the impurity diffusivities in solid and liquid silicon,” *Jom*, vol. 61, no. 11, pp. 49–55, 2009.
- [100] H. Kodera, “Diffusion coefficients of impurities in silicon melt,” *Japanese Journal of Applied Physics*, vol. 2, no. 4, p. 212, 1963.
- [101] D. Bäuerle, *Laser Processing and Chemistry* -. Berlin Heidelberg: Springer Science & Business Media, 2013.
- [102] F. Millot, V. Sarou-Kanian, J.-C. Rifflet, and B. Vinet, “The surface tension of liquid silicon at high temperature,” *Materials Science and Engineering: A*, vol. 495, no. 1-2, pp. 8–13, 2008.
- [103] M. J. Assael, I. J. Armyra, J. Brillo, S. V. Stankus, J. Wu, and W. A. Wakeham, “Reference data for the density and viscosity of liquid cadmium, cobalt, gallium, indium, mercury, silicon, thallium, and zinc,” *Journal of Physical and Chemical Reference Data*, vol. 41, no. 3, p. 033101, 2012.
- [104] Y. Kim and K. Morita, “Thermal conductivity of molten B_2O_3 , B_2O_3 - SiO_2 , Na_2O - B_2O_3 , and Na_2O - SiO_2 systems,” *Journal of the American Ceramic Society*, vol. 98, no. 5, pp. 1588–1595, 2015. [Online]. Available: <https://ceramics.onlinelibrary.wiley.com/doi/abs/10.1111/jace.13490>
- [105] A. NAPOLITANO, P. B. MACEDO, and E. G. HAWKINS, “Viscosity and density of boron trioxide,” *Journal of the American Ceramic Society*, vol. 48, no. 12, pp. 613–616, 1965. [Online]. Available: <https://ceramics.onlinelibrary.wiley.com/doi/abs/10.1111/j.1151-2916.1965.tb14690.x>
- [106] V. T. Cherepin, *Secondary Ion Mass Spectroscopy of Solid Surfaces* -. Boca Raton, Fla: CRC Press, 2020.
-

- [107] P. van der Heide, *Secondary Ion Mass Spectrometry - An Introduction to Principles and Practices*. John Wiley & Sons (US), 2014.
 - [108] L. C. Microscope, “COLOR 3D Laser COLOR 3D Laser Confocal Microscope,” pp. 1–28.
 - [109] Bruker, “Performing step metrology with dektak stylus profilers,” https://www.bruker.com/en/products-and-solutions/test-and-measurement/stylus-profilometers/_jcr_content/root/contentpar/search_copy.download-asset.pdf/eec15c12-6f64-4991-b89e-c8cc3e1cb973/Performing%20Step%20Metrology%20with%20Dektak%20Stylus%20Profilers%20App%20Note-BRUKER.pdf, 2021.
-

List of Publications

Parts of this work are published in the following publications:

- M. Hassan, M. Dahlinger, J. R. Koehler, R. Zapf-Gottwick, and J. H. Werner, "Unified model for laser doping of silicon from precursors", *Materials*, vol. 14, no. 9, p. 2322, 2021.
- Zapf-Gottwick, Renate & Seren, Sven & Fernandez-Robledo, Susana & Wete, Evariste-Pasky & Schiliro, Matteo & Hassan, Mohamed & Mihailetchi, Valentin & Buck, Thomas & Kopecek, Radovan & Koehler, Juergen & Werner, Juergen. (2022). "Solar Cells with Laser Doped Boron Layers from Atmospheric Pressure Chemical Vapor Deposition". *Solar*. Vol. 2. No. 2. MDPI, 2022.
- Hassan, Mohamed & Werner, Juergen (2023). Effective Depth Approximation of Sheet Conductance of Laser-Doped Layers. American Institute of Physics (in preparation)

Acknowledgment

At the end of this work, I would like to express my gratitude and thankfulness to all the people who helped, encouraged and supported me throughout this work.

I am deeply indebted to Prof. Dr. Jürgen H. Werner for giving me the opportunity to join institute for photovoltaics as a Ph.D student. Afterwards, you offered me the opportunity to work in one of the cutting edge solar cells' production technologies, laser doped IBC-Solar cells. Scientifically, you always support me to dig deeper in results and to find the simple mathematical explanation hiding behind. Last but not least, I learned so much from you even if it was the hard way.

I'm extremely grateful to Dr. -Ing. Jürgen Köhler for his evermore support since the first moment I joined institute for photovoltaics. My optics, laser and laser processing knowledge returns to you and your encouragement. Designing, validation and optimization of my model for laser doping would not have been completed without the fruitful discussions between us. Once more, I would like to express my gratitude working with you.

Words cannot express my gratitude to Dr. Renate Zapf-Gottwick; you leaded me and my colleagues through the "Laser IBC Module" project and with your guidance and leadership, we achieved on a 6" silicon wafer an efficiency $\eta > 22.2\%$. It was a pleasure working with you.

Words cannot express my gratitude to my colleagues: Patrick Lill, Ahmed Lachhab, Matteo Schilirò, Evariste Pasky Wete and Kathrin Ohmer for the best team work I ever experienced. Special thanks to Patrick Lill, I could not have undertaken this journey without your support.

Special thanks for Birgitt Winter, Hendrick Moldenhauer, Lydia Beisel and Katja Schweiger for the world class working accuracy and the cooperative work. The achievement of such a high solar cell efficiency ($\eta > 22.2\%$) comes back to your work precision.

My gratitude to Freymut Hilscher und Sabine Ost for supporting me with organizational problems.

This endeavor would not have been possible without the financial support from the "Deutscher Akademischer Austauschdienst" (DAAD).

My dear Father and Mother, I would like to express my deepest appreciation to your love, support, and encouragement. With your backing, you contributed to every chapter constituting this work.

My lovely wife Soha, all what I have achieved would not have been real without you standing by my side. You always supported me during depression and frustration periods I have been through. I am indescribable glad to have you by my side and extremely happy to continue my life with you. Thanks forever.

Declaration

herewith, I, Mohamed Hassan, formally declare that I have written the submitted dissertation independently and did not use any outside support except for the quoted literature.

Stuttgart, 16.09.2022